

Materials and Devices for Optical Switching and Modulation of Photonic Integrated Circuits

by

Dilan Anuradha Seneviratne

Bachelor of Engineering, First Class
Imperial College (London, United Kingdom), 1999

Submitted to the Department of Materials Science and Engineering
in Partial Fulfillment of the Requirements for the Degree of
Doctor of Philosophy in Electronic, Photonic and Magnetic Materials

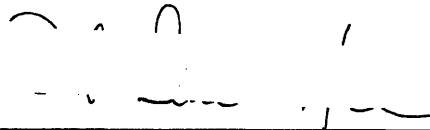
at the

Massachusetts Institute of Technology

June 2007

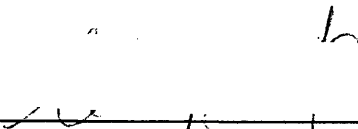
© 2007 Massachusetts Institute of Technology
All rights reserved

Signature of Author



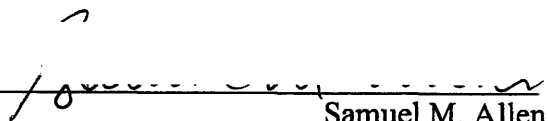
Dilan Anuradha Seneviratne
Department of Materials Science and Engineering
May 10th, 2007

Certified by

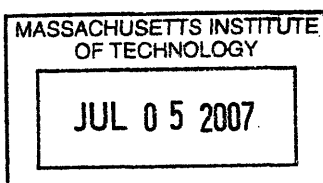


Harry L. Tuller
Professor of Ceramics and Electronic Materials
Thesis Supervisor

Accepted by



Samuel M. Allen
POSCO Professor of Physical Metallurgy
Chair, Departmental Committee on Graduate Students



ARCHIVES

Materials and Devices for Optical Switching and Modulation of Photonic Integrated Circuits

by

Dilan Anuradha Seneviratne

Submitted to the Department of Materials Science and Engineering on May 10th, 2007
in Partial Fulfillment of the Requirements for the Degree of
Doctor of Philosophy in Electronic, Photonic and Magnetic Materials

Abstract

The drive towards photonic integrated circuits (PIC) necessitates the development of new devices and materials capable of achieving miniaturization and integration on a CMOS compatible platform. Optical switching: fast modulation and add-drop switches, key components in a PIC, were investigated. A MEMS-based approach was utilized to control switching in planar ring resonator waveguide structures. A switch extinction ratio of 15 dB, switch speed of 60 μ s and 1 mW operating power were demonstrated.

A metal-insulator transition material, VO₂, was identified as a material with potential for enhancing the switch speed with speeds in excess of gigahertz rates with minimal device footprint. Fundamental material transport properties and nonstoichiometry in VO₂ were characterized. Nonstoichiometry as high as 5% was measured. A Frenkel defect model was used to describe the behavior in VO₂ in which vanadium interstitials were attributed to be the dominant ionic defect in the reducing regime. Frozen-in vanadium interstitials, acting as shallow donors lying 20 meV below the conduction band in the semiconducting phase, enhance the low temperature conductivity and free carrier concentration.

VO₂ was shown to exhibit an activated mobility in its semiconducting and “metallic” phases with room temperature mobility estimated to be 5×10^{-2} cm²/Vs. Electrical switch contrasts of as high as ~5000 and optical extinction ratios of approximately 16 dB were demonstrated. Free carrier absorption due to shallow donor vanadium interstitials was identified as a dominant absorption mechanism at near-IR wavelengths. Control of the degree of nonstoichiometry was shown to influence the near-IR absorption effects.

To address the need for an integrated fast switch for data encoding, a thin film electro-optic (E-O) modulator, based on barium titanate (BaTiO_3) or barium titanate-strontium titanate (SrTiO_3) superlattices, was developed. Mach-Zhender E-O modulators were designed, fabricated with CMOS compatible processing steps and tested. Effective electro-optic values as high as 73pm/V , 2.5 times better performance compared to commercial bulk LiNbO_3 technology was demonstrated, with device area less than $30,000\ \mu\text{m}^2$.

Thesis Advisor: Harry L. Tuller

Title: Professor of Ceramics and Electronic Materials

Acknowledgments

In working towards my PhD there have been numerous individuals and organizations that have assisted me. Without their support this thesis would not have been possible.

First and foremost, I would like to thank my Thesis Advisor, Professor Harry Tuller, for accepting me into his group and guiding me through my entire academic and research work. He has been very patient and extremely supportive through all the ups and downs in the research front. His broad expertise helped in directing forward and keeping on track. I would also like to thank my Thesis Committee, Professor Lionel Kimerling and Professor Subra Suresh, for their critical questioning and comments that helped improve my thesis.

I am deeply grateful to David Bono for his tremendous assistance in setting up some of my key experiments. He was my “go to person” whenever I needed some help with electronics and electrical equipment setups. I am also thankful to staff at MIT’s Microsystems Technology Laboratory, especially Kurt Broderick and Bob Bicchieri for their advice and help in setting up and troubleshooting process steps in the fab.

I would like to thank Jussi Hiltunen, Gregory Nielson, Michael Watts, Rong Sun, Francisco Lopez-Arroyo, and Ytshak Avrahami, for the close collaboration in the various projects that contributed to this project. Some of their ideas, fab processing steps, and results contributed towards piecing together my thesis. I am also indebted to them for the critical discussion and analysis. In addition, I would like to thank all past and present member of Professor Tuller’s Research Group: Josh Hertz, Yoonsil Jin, WooChul Jung, Woosik Kim, Scott Litzelman, Yongki Min, Huankiat Seh, George Whitefield, and for the enlightening scientific and non-scientific discussions in the student office. I am also very grateful to Todd Stefanik for advising me and guiding me in setting up my coulometric titration, electrical conductivity and oxygen pump setups. I would like to thank Huankiat Seh for his continued friendship pre- and post-MIT.

I would also like to thank Fernando Castano and Viram Sivakumar of Professor Ross’ group for their help in maintaining the PLD system.

Research would not be possible without adequate funding. I am thankful to the following funding organization that supported most of my degree: DMSE Teaching Assistantship Fund, Analog Devices Inc., Pirelli Labs, s.p.a, and the Ford-MIT Alliance.

I would like to thank all my friends who helped me stay sane during my doctoral work. Simon Mui and Yoon Chang Mui will always stay dear to me for their great friendship and welcoming home. Waleed Farahat, Mayssam Ali Farahat, and Neda Vukmirovic helped me keep my focus during the latter stages of my degree. Members of the MIT Rugby Team provided me with an environment where I could relax outside of work and engage in some athletic activities as well as social activities. I am also thankful to Amanda Moment for being a super roommate during my last two years at MIT.

Last but not least, I would like to thank my dear Mother, Father and Brother. They have been immensely supportive during all my years at MIT. They helped me stay motivated and focused and created an environment where I had no other worries to contend with. Thank you very much for your love and care.

Contents

ABSTRACT	3
ACKNOWLEDGMENTS	5
CONTENTS	7
LIST OF FIGURES	11
LIST OF TABLES	15
CHAPTER 1: INTRODUCTION	17
1.1 MOTIVATION.....	17
1.1 OPTICAL SWITCHING	20
1.1.1 <i>Mechanical Switches</i>	20
1.1.2 <i>Thermo-optic switches</i>	20
1.1.3 <i>Free-carrier induced absorption switches</i>	21
1.1.4 <i>Summary of Switch Designs</i>	21
1.2 PROPOSED APPROACH TO OPTICAL SWITCHING FOR OADM	22
1.3 MEMS-BASED SWITCH	23
1.4 METAL-INSULATOR TRANSITION MATERIALS	25
1.5 STRUCTURE AND PROPERTIES OF VO ₂	26
1.5.1 <i>Electrical and Optical Properties</i>	29
1.6 DEFECT MODEL.....	32
1.7 APPLICATION OF DEFECT MODEL	37
1.8 ELECTRO-OPTIC OPTICAL MODULATION.....	38
CHAPTER 2: OBJECTIVES	41
2.1 OPTICAL SWITCHING	41
2.1.1 <i>MEMS-based switch</i>	42
2.1.2 <i>Vanadium Oxide Objectives</i>	42
2.2 OPTICAL MODULATOR OBJECTIVES.....	43
CHAPTER 3: EXPERIMENTAL	45
3.1 MEMS-BASED OPTICAL SWITCH.....	45
3.1.1 <i>Optical Design Requirements</i>	45
3.1.2 <i>Mechanical Design Requirements</i>	45
3.1.3 <i>Switch Fabrication</i>	46
3.1.4 <i>Residual Stress Characterization</i>	47
3.1.5 <i>Optical Switch Testing</i>	47

3.2	VANADIUM (IV) OXIDE	49
3.2.1	<i>Sample Preparation</i>	49
3.2.2	<i>Thin Film Sample Preparation</i>	50
3.2.3	<i>Physical Characterization</i>	52
3.2.4	<i>Electrical Characterization</i>	53
3.2.5	<i>Optical Characterization – Transmission measurements</i>	60
3.3	BARIUM TITANATE ELECTRO-OPTIC MODULATOR.....	61
3.3.1	<i>Thin film Growth</i>	61
3.3.2	<i>Thin Film Characterization</i>	62
3.3.3	<i>Electro-Optic Modulator Design</i>	62
3.3.4	<i>Modulator Fabrication</i>	62
3.3.5	<i>Modulator Testing</i>	64
CHAPTER 4: RESULTS		67
4.1	MEMS-SWITCH RESULTS	67
4.1.1	<i>Fabrication Results</i>	67
4.1.2	<i>MEMS Optical Test Results</i>	69
4.1.3	<i>TiN based mechanical beams</i>	70
4.2	VANADIUM (IV) OXIDE	74
4.2.1	<i>High Temperature X-ray Diffraction</i>	74
4.2.2	<i>Thin Film X-ray Diffraction</i>	76
4.2.3	<i>DC Electrical Conductivity – Bulk Samples</i>	76
4.2.4	<i>Thermoelectric Power – Bulk Samples</i>	77
4.2.5	<i>Low Temperature Iso-stoichiometric electrical conductivity measurements– Bulk VO₂</i>	78
4.2.6	<i>Low Temperature Thermoelectric power – Bulk</i>	81
4.2.7	<i>Low temperature conductivity and TEP – thin films</i>	83
4.2.8	<i>Coulometric Titration</i>	83
4.2.9	<i>Optical Properties</i>	89
4.3	BARIUM TITANATE BASED E-O MODULATOR.....	91
4.3.1	<i>Thin film growth results</i>	91
4.3.2	<i>E-O Modulator Device Simulations</i>	92
4.3.3	<i>E-O Modulator Fabrication Results</i>	94
4.3.4	<i>E-O Modulator Test Results</i>	95
CHAPTER 5: DISCUSSION		97
5.1	MEMS-SWITCH	97
5.1.1	<i>Titanium Nitride for enhanced optical switch contrast</i>	99
5.1.2	<i>Summary of MEMS Switch</i>	100

5.2	VANADIUM (IV) OXIDE	101
5.2.1	<i>Electrical Properties of VO₂</i>	102
5.2.2	<i>PO₂ dependence of conductivity</i>	104
5.2.3	<i>Non-stoichiometry effects on Semiconducting Properties of VO₂</i>	105
5.2.4	<i>Non-stoichiometry</i>	108
5.2.5	<i>Thin film electrical properties</i>	111
5.2.6	<i>Optical Properties of VO₂ thin films</i>	111
5.2.7	<i>Summary of the Transport Characteristics of VO₂</i>	112
5.2.8	<i>Implications for VO₂ based optical switching</i>	113
5.3	BARIUM TITANATE E-O MODULATOR	114
5.3.1	<i>Structure</i>	114
5.3.2	<i>Electro-optic Performance</i>	115
5.3.3	<i>Summary of BT E-O Modulator</i>	116
CHAPTER 6: CONCLUSIONS.....		117
CHAPTER 7: FUTURE WORK.....		119
7.1	MEMS SWITCH	119
7.2	VO ₂ BASED SWITCH	119
7.3	BARIUM TITANATE BASED E-O MODULATORS	119
APPENDIX A – MATERIAL PROPERTIES OF TITANIUM NITRIDE AND SILICON.....		121
BIBLIOGRAPHY		123

List of Figures

Figure 1-1 Schematic showing the ring-resonator filter design by Little et al [42].....	24
Figure 1-2 Transfer of optical power between the throughput and drop ports of the ring-resonator filter [81].....	25
Figure 1-3 Resistivity data showing the metal-insulator transition in various transition metal oxides [80].....	26
Figure 1-4 Phase diagram of the V-O system. Reproduced from [82].....	27
Figure 1-5 Existence ranges of the various vanadium oxide phases as a function of oxygen partial pressure and temperature [7].	28
Figure 1-6 A) Monoclinic structure represented by bold lines on the left side and tetragonal crystal structure shown with bold lines on the right side. B) Schematic showing change in band structure associated with change in crystal structure: left side is the semiconducting phase band diagram and right side is the metallic band diagram. Taken from Cavalleri et al [9].....	29
Figure 1-7 Compilation of resistivity data for single crystal VO ₂ from different authors by Vest et al [80].	31
Figure 1-8 Brouwer diagram for VO ₂ based on the defect equations in Table 3.....	35
Figure 1-9 Schematic of the Mach-Zhender modulator configuration.	40
Figure 3-1 Schematic showing the fabrication sequence for fabricating the MEMS ring-resonator switch.....	47
Figure 3-2 Schematic of the bulk sample arrangement for electrical conductivity and thermoelectric power measurements.	50
Figure 3-3 Schematic of the pulse laser deposition system.	51
Figure 3-4 Schematic of the electrical conductivity setup for bulk samples.	54
Figure 3-5 A schematic of the PID controller circuit.	55
Figure 3-6 Schematic of the iso-stoichiometry anneal and measurement setup.....	57
Figure 3-7 Schematic of the coulometric titration cell setup.....	59
Figure 3-8 Schematic showing the processing steps for fabricating the E-O modulator devices. A) PLD growth of BT film. B) PECVD deposition of SiN	

waveguide layer. C) Pattern of SiN. D) Sputter deposition of aluminum. E) Pattern and wet etch of aluminum.....	63
Figure 3-9 Schematic of the E-O modulator test setup.....	65
Figure 4-1 SEM micrographs of a typical MEMS ring-resonator switch. A) Top view of entire MEMS device on top of a ring resonator with anchors on either side of the beams and contact pad on the left. B) Close-up of the MEMS structures near the ring resonator.	68
Figure 4-2 Relative transmission in the throughput and drop ports of the optical ring resonator with and without applied voltage to the MEMS structure. The relative transmission was measured as a function of wavelength.	69
Figure 4-3 Temporal response of the ring resonator. The relative transmission in the throughput port is shown.....	70
Figure 4-4 Results of residual-stress induced buckling in post-released fixed-fixed beams. A) Beam deflection data pre- and post- anneal. B) Zygo deflection contour plot of a typical MEMS beam pre-anneal and post-released. C) Contour plot showing beam deflection after anneal and release.	71
Figure 4-5 Stress evolution in TiN during annealing of as-deposited thin film on bare silicon wafer substrate.	72
Figure 4-6 Stress evolution during annealing of TiN sputter deposited thin film on silicon (substrate)-silicon dioxide-poly-silcon stack.	73
Figure 4-7 Theta-2Theta x-ray spectrum of as-deposited and post annealed TiN thin film.	74
Figure 4-8 High temperature in-situ x-ray diffraction spectrum taken between 580°C and 650°C in A) 100ppm CO/CO ₂ gas mixture and B) 700ppm CO/CO ₂ gas mixture.	75
Figure 4-9 A typical x-ray diffraction spectrum for a VO ₂ thin film deposited on a fused quartz substrate.....	76
Figure 4-10 DC electrical conductivity of VO ₂ as a function of PO ₂ for a series of temperatures.	77
Figure 4-11 Thermoelectric power as a function of oxygen partial pressure for bulk VO ₂ samples measured at elevated temperatures.	78

Figure 4-12 Electrical conductivity vs reciprocal temperature of bulk VO ₂ samples with <i>frozen-in</i> stoichiometry.	79
Figure 4-13 Temperature dependent electrical conductivity of a bulk VO ₂ sample above the phase transition with <i>frozen-in</i> stoichiometry annealed in a 1000ppm O ₂ ambient.	80
Figure 4-14 Temperature dependent of the TEP coefficient in a bulk VO ₂ sample above the phase transition with <i>frozen-in</i> stoichiometry annealed in a 1000ppm O ₂ ambient.	80
Figure 4-15 Thermoelectric power measurements on bulk samples with <i>frozen-in</i> stoichiometry. The oxygen partial pressures in the box on the right indicate the value used during the high temperature anneal.	81
Figure 4-16 Log of carrier concentration vs reciprocal temperature in the semiconducting phase of VO ₂ for a sample annealed at 1000 ppm O ₂ and <i>frozen-in</i> stoichiometry assuming an effective mass of $3*m_0$	82
Figure 4-17 DC electrical conductivity of thin films of VO ₂ deposited at different oxygen working pressures during pulse laser deposition.	83
Figure 4-18 Raw data from coulometric titration measurements between 500C and 650C. The plot shows the equilibrium oxygen partial pressure as a function of amount of oxygen pumped out of the titration cell.	84
Figure 4-19 The equilibrium oxygen partial pressure as a function of total non-stoichiometry in VO ₂	85
Figure 4-20 Dependence of absolute stoichiometry, δ , in VO _{2-δ} as a function of oxygen partial pressure.	87
Figure 4-21 Temperature dependence of $\log[K_F]$ determined from fitting the titration data.	87
Figure 4-22 Temperature dependence of $\log[K_R]$ determined from fitting the titration data.	88
Figure 4-23 Temperature dependence of $\log[K_E]$ determined from fitting the titration data.	88
Figure 4-24 Wavelength dependence of optical transmission above and below the phase transition in VO ₂ for PLD as-deposited thin films.	89

Figure 4-25 Dependence of absorption coefficient of semiconducting VO₂ as a function of energy for thin films under different oxygen working pressures during PLD deposition..... 90

Figure 4-26 Plot of the dependence of the absorption coefficient of VO₂ at 1550 nm wavelength as a function of oxygen total pressure during PLD deposition.90

Figure 4-27 Real and imaginary part of the refractive index determined by ellipsometry of thin VO₂ film deposited by PLD at 4 mTorr oxygen total pressure. 91

Figure 4-28 θ -2 θ x-ray spectra of thin films of BT grown by PLD. Data courtesy of Jussi Hiltunen..... 92

Figure 4-29 X-ray rocking curve results showing the four fold symmetry of the (100)/(001) planes normal to the BT film surface. Data courtesy of Jussi Hiltunen..... 93

Figure 4-30 Contour plot of optical field intensity distribution for the strip loaded MZ modulator design. Data courtesy of Jussi Hiltunen..... 93

Figure 4-31 A) SEM cross-section image of a fabricated BT E-O modulator. B) Top view optical micrograph showing part section of the Mach-Zehnder structure of two test devices next to each other. The Y-split of the MZ waveguide arms can be seen. 94

Figure 4-32 A) Contour plot of the measured optical field intensity as function of position at the output side of the MZ modulator. B) Near-field image captured with an infra-red camera..... 95

Figure 4-33 Typical intensity modulation in a MZ test structure as a function of applied voltage. 96

Figure 5-1 Plot of conductivity vs reciprocal temperature assuming an activated mobility model..... 103

Figure 5-2 Schematic of possible implementation of a ring resonator switch using VO₂. 114

List of Tables

Table 2 OADM switch device requirements.....	22
Table 3 Defect equations in different regions of oxygen partial pressure for VO ₂	36
Table 4 Detailed step-by-step list of the process steps for fabricating the MEMS optical switch. Names within parenthesis refer to MTL's machine names.....	48
Table 5 Pulse laser deposition conditions.....	52
Table 6 shows the optimum deposition parameters that were used to grow epitaxial thin films of barium titanate.....	61
Table 7 lists the measured effective electro-optic coefficient for different materials and deposition conditions of BT.....	96
Table 8 List of Mechanical properties of TiN.....	121
Table 9 List of Mechanical properties of Silicon.....	121

Chapter 1: Introduction

1.1 Motivation

Integrated photonics, the field of integrating optical components on a single platform is increasingly attracting wide interest from microprocessor designers and telecommunication system developers driven by the ever increasing demand for larger bandwidth.

In telecommunications the bandwidth demand is driven by the increase in data-intensive applications, such as video, voice over IP (VOIP), etc. over the internet. Over long-haul distances (distances > 100 's km), optical fiber communication is prevalent. Current optical fiber communication employs wavelength division multiplexing to multiple optical signals (wavelengths) within a single optical fiber (or waveguide). Wavelength Division Multiplexing (WDM) is a technique of combining different wavelengths of light (multiplexing) and transmitting them in a single waveguide. The light is then un-bundled (de-multiplexed) at the receiver end.

Whilst long-haul communication is based on optical networks, metro area networks (distance between 10 's km to 100 's of km), MAN, and local area networks (few kilometer distances), LAN, are based primarily on copper-based electrical signal transmission. Copper based transmission of signals is limited by RC delays as well as optical-electrical-optical (O-E-O) signal conversions. O-E-O conversion is limited by the speed of electronic transistors. The maximum data rates in LAN and MAN networks based on copper are 100 's Mbits/s.

In logic applications, the Moore's Law driven increase in transistor count has led to increasing data rates in global and local interconnects within a microprocessor. The state-of-the-art microprocessor interconnects are facing many obstacles in keeping up with the required data rates (several Giga bits per second) due to resistance-capacitance (RC) delays and increasing fraction of side-wall scattering with decreasing interconnect line widths [63].

The limitations placed by copper based signal transmission in both telecommunication and microprocessors can be overcome by optical signal transmission, with the ability to deliver high data bandwidth limited only by the speed of light.

In telecommunications, programs such as fiber-to-the-home (FTTH) are touted as much needed solutions for removing the copper and O-E bottlenecks. A single optical fiber can carry several hundred Gbits/s compared to 100's Mbits/s over copper [33]. In order for programs such as FTTH to be realized, advances are needed in integrating various optical components onto a single platform referred to as photonic integrated circuit (PIC). This would allow direct optical interconnection between long-haul optical fiber networks and MAN's and LAN's. Integration of optical components is a necessity for minimizing the price/performance ratio of optical cross-connects and optical add-drop devices [53]. Assembly of discrete components to form add-drop or cross-connect leads to high cost due to complex assembly and aligning processes [53]. On the other hand, integrated add-drops and cross-connects are self aligned, and eliminate the cost of complex assembly and alignment.

Currently, the optical components necessary for optical communication such as light sources (laser), detectors, modulators, and switches are available as discrete components. When building an optical signal processor box, these various components are assembled as needed. The assembly can be complex, given the need to align components precisely. Such complex assembly can be tolerated if the number of installations is only a few hundred. However, with program like FTTH, millions of optical signal processors will be needed, scaling directly with the number of households and end users. In this scenario, components requiring complex assembly and alignment are not cost effective. The drive to develop photonic integrated circuits is driven, in part, by this need to minimize cost of assembly and installation of discrete component technology. Optical *switching* is a key component requiring integration on a PIC. Optical *switches* have various applications on a PIC. These are listed in Table 1, along with the required switching speed, a key requirement for the switches.

Table 1 Application of optical switches in a typical photonic integrated circuit and the required switching speeds [61].

Application	Function	Switch speed
Provisioning	Add-drop a specific wavelength	1 – 10 ms
Packet Switching	Switching a short packet of information	1 ns (duration of packet: several bytes)
Modulation	Encode electrical 1's and 0's	10 ps (bit duration)

An optical modulator is used to convert a digital electrical signal carrying 1's and 0's to an optical signal. Modulators are based on intensity modulation, where peak intensity will correspond to a 1 bit and minimum intensity corresponding to a 0 bit. Given that information is generated at the speeds of 100's to 1000's of Mbits per second (Mbps), the modulator operation needs to be in the 100's of Giga hertz frequency to Tera hertz frequency range.

An optical modulator is in effect acting as a switch, switching an optical signal on and off. In addition to modulating an optical signal, optical switches are needed in a photonic integrated circuit (PIC) to turn *on* and *off* optical signals by re-directing or changing the path of an optical signal based on an external command. In the most basic configuration, a signal from an input channel is directed to one of two output channels. The device that directs the optical signal to a particular output channel is the optical switch. A slightly more complicated version is the optical add-drop multiplexer (OADM). In this case, a specific wavelength signal can be added, or dropped from a particular waveguide or channel, based on an external command. An OADM is a combination of several optical switches.

Whilst an optical modulator acts like an optical switch, modulators cannot be used as switches due to the fact that current modulator devices occupy large areas (order of few millimeters) and many optical switches are needed on a PIC. On the other hand, current available optical switches cannot be used for optical modulation due to the relatively low switch speeds. Thus, both these devices need to be addressed separately.

In this thesis, materials and devices for add-drop multiplexers and optical modulation are investigated.

1.1 Optical Switching

There are numerous designs described in the literature that are reported to carry out optical switching functions with target application in add-drop multiplexing. The switches available can be broadly classified into: mechanical (MEMS-based) switches, thermo-optic switches, free-carrier induced absorption switches, and electro-optic switches. The mechanical, thermo-optic and free-carrier based switches are described in this section. Electro-optic switches are discussed in section 1.8

1.1.1 Mechanical Switches

Some of these designs involve tilting mirrors [1,20], cantilever-based moving waveguides [52] and free standing mirrors supported by torsion beams [11]. The tilting mirror approach of Lucent [1,20] is commercially used for large scale optical cross-connects. This design requires 3-D alignment to optical fibres, and is therefore, not compatible with planar PIC's. In addition the drive voltage for this design is 200V and switching times of a few milliseconds. The design of Chen et al [11] is a free-space design where switching is accomplished by electrostatic deflection of a door-like mirror with hinges. The area of a single 2 x 2 switch occupies an area of several square millimeter which is not compatible with large scale PIC's.

The cantilever-based waveguide switch [52] is a planar design which can switch between eight output waveguides (1 x 8). The horizontal deflection of the cantilever is electrostatically actuated. The drive voltage is approximately 70V and switch time is approximately a millisecond.

1.1.2 Thermo-optic switches

Thermo-optic switches operate based on a temperature-change-induced change in the refractive index. Silicon dioxide [16] and polymer [29] based switches are described in the literature. These devices overall have large switch times, order of several milliseconds, and require relatively large amounts of power, order of 100's of milliwatts

per switch. The slow switch speed and large power requirement render these types of design unattractive for PIC's.

1.1.3 Free-carrier induced absorption switches

Free-carrier switches operate based on a change in the effective index [1], induced by a carriers injected into the switch area or by a plasma dispersion effect [44], also induced by carrier injection. These switches are usually based on silicon or other III-V semiconductors such as GaAs. These designs are compatible with planar PIC's, but require relatively large operating powers (several 100's of milliwatts) and device size are also relatively large (just under 1 square millimeter).

1.1.4 Summary of Switch Designs

Several selective optical switch designs were discussed above covering largely three different switch design types based on MEMS, thermo-optic and free-carriers.

While all of these devices are fabricated through conventional micromachining processes, the MEMS-based approaches mentioned thus far have several drawbacks due to their large footprint (sizes of the order of millimeters) [11], fabrication complexity [11, 52], and complex 3-D assembly [1, 20]. Furthermore, all of these devices require actuation voltages of several 10's of volts and switching times are at best 1 ms. The thermo-optic switches have relatively slow switching speeds and high operating powers. The free-carrier based switches are unattractive due to their large device sizes and relatively high operating powers.

Given the drawbacks of the designs reported in literature a different approach to OADM switching is explored in this thesis. The key requirements for the OADM that will be aimed for are summarized in Table 2.

Table 2 OADM switch device requirements.

Requirement	Desired value
Extinction ratio: ratio between the <i>on</i> and <i>off</i> power	> 15 dB
Insertion loss: loss due to switch design	As low as possible
Switch speed	100's μ s
Operating power	< 1 mW
Drive voltage	5 V
Device footprint (area)	< 5000 μ m ²

1.2 Proposed approach to optical switching for OADM

In this thesis, two approaches are taken for optical switching in optical add-drop's. The first approach involves using a MEMS-based electrostatic device to switch *off* and *on* an optical ring resonator. The second approach involves a phase-transition based metal-insulator transition optical switch.

Intrinsic wavelength switching is a unique characteristic of the MEMS-based switch. Typically, wavelength-selective switching is achieved by demultiplexing the WDM signal, switching the individual wavelength, and then remultiplexing the output signal. The MEMS switch reported in this thesis reproduces the entire process with a single element. This switch is ideally suited for creating reconfigurable integrated optical circuits for a variety of optical networking purposes. Additional advantages of this MEMS switch is its complementary metal-oxide-semiconductor (CMOS) compatibility, small footprint, and low power consumption. These characteristics are all important to achieve large-scale integration of optical switches into low-cost high-performance WDM optical networks.

The second approach involves metal-insulator transition based switching. This design, involves no macroscopic movement, like in the MEMS-switch. Instead, the ultra-fast phase transition and the associated change in optical absorption coefficient are exploited.

1.3 MEMS-based switch

A variety of MEMS-based approaches to optical switching as reported in the literature were described earlier. As was pointed out, many of the reported designs were not suitable for photonic integrated circuits due to large area device footprint, non-2D compatible design, large insertion losses, insufficient switch contrasts and lack of wavelength selectivity. In this thesis, a planar wavelength selective switch with low drive voltages and relatively small device footprint is developed.

This integrated wavelength selective optical switch was proposed by Watts [81]. This design is based on ring-resonator filters developed by Little et al. [42, 43]. This design involves a waveguide ring resonator that is side-coupled to a pair of bus waveguides as shown in the schematic in Figure 1-1 [43]. An optical signal traveling in the “input” waveguide can be completely transferred (switched) to the “drop” waveguide via the ring waveguide provided the dimensions of the ring permit the particular wavelength being switched to resonate in the ring. Resonance occurs when the circumference of the ring is an integral multiple of the wavelength being switched. If the ring is off-resonance, i.e. the circumference of the ring is not an integral multiple of the wavelength; the signal does not interact with the ring and it simply continues down the input/throughput waveguide uninterrupted.

In its “on” state, any wavelength will be switched from the input waveguide to the drop waveguide provided there is a ring resonator designed for each wavelength. In this case, the switch will always remain “on”. Some mechanism is needed to be able to control the switching of the resonator, i.e. be able to switch the resonance on and off. A key advantage of this filter design is that this is compatible with planar integrated photonics. This filter can be made into an optical switch if the resonance can be turned “off” when needed. A MEMS based switching mechanism is developed in this thesis, to render this filter a wavelength selective optical switch.

It has been shown theoretically that if sufficient absorption is introduced into the ring, switching of the optical signal into the drop port can be prevented. When there is significant absorption in the ring, no resonance occurs within it. The signal in the input waveguide will simply remain in the input waveguide. Figure 1-2 below shows how increasing absorption in the ring leads to reduction in the amount of signal power transferred to the drop port, thus preventing switching [81].

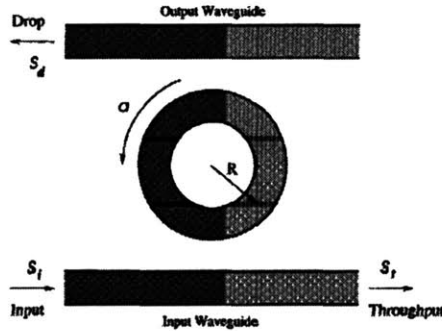


Figure 1-1 Schematic showing the ring-resonator filter design by Little et al [42].

The wavelength selectivity of the switch is created by high index-contrast optical ring resonator filters. The high-index contrast between the core and cladding materials allows the rings to have a small radius (10 μm), and therefore, a large free spectral range (FSR), with low bending loss [2]. A single-ring filter was selected for this initial device to minimize complexity, however, the switching technique could be easily applied to multi-ring filters that have improved optical filter performance.

The high-index core material used for the waveguides is silicon-rich silicon nitride with a refractive index of 2.2. The waveguide core cross section is 1050 nm wide for the bus waveguides and 1010 nm wide for the ring-resonator waveguides, both were 330 nm thick. The cladding is 3 μm -thick silicon oxide on the bottom and air on the top and sides.

Optical modeling calculations carried out by Watts [81] predicts the effect of the absorbing material on power throughput as a function of distance from the ring resonator.

These calculations were carried out for the case where the switch is integrated with silicon-based waveguides. For the case of Si_3N_4 waveguides, the absorbing membrane needs to be at least 1.2 μm away from the ring in the “off” state and less than 0.2 μm

away in the “on” state (Figure 1-2). These calculations were based on the assumption that the absorbing material has a thickness of at least 0.2 μm .

The main requirements for the MEMS switch are:

- Actuation voltage no greater than 5 V
- Switching speed of at or below 1 ms
- Membrane displacement of $\sim 1.2 \mu\text{m}$
- Use of materials and micromachining techniques compatible with integration of other optical devices in the optical signal processor.

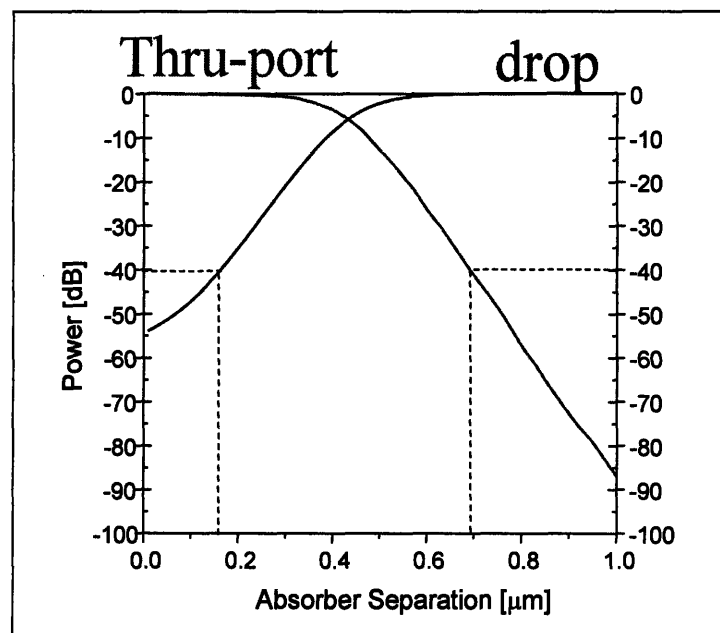


Figure 1-2 Transfer of optical power between the throughput and drop ports of the ring-resonator filter [81].

1.4 Metal-Insulator Transition Materials

Metal-Insulator Transition (MIT) materials are characterized by a sharp discontinuous change in resistivity due to change in temperature. In the literature, there are several reports of materials that exhibit this property, as summarized by Vest et al [80] and

Figure 1-3. All the materials displayed in this figure are transition-metal oxides. The underlying principles and physics governing the MIT effect depend on the specific material. Of the oxides that exhibit the MIT effect, VO_2 is the more attractive, for several reasons:

1. The transition occurs close to room temperature (68°C) compared to other materials which show transitions at -165°C (e.g. V_2O_3) and $+227^\circ\text{C}$ (Ti_2O_3).
2. The transition in VO_2 , accompanied by approximately 4 orders of magnitude change in resistivity, is sharp, occurring apparently over approximately 2-3 degrees Celcius.

For these reasons, VO_2 was chosen for further investigation.

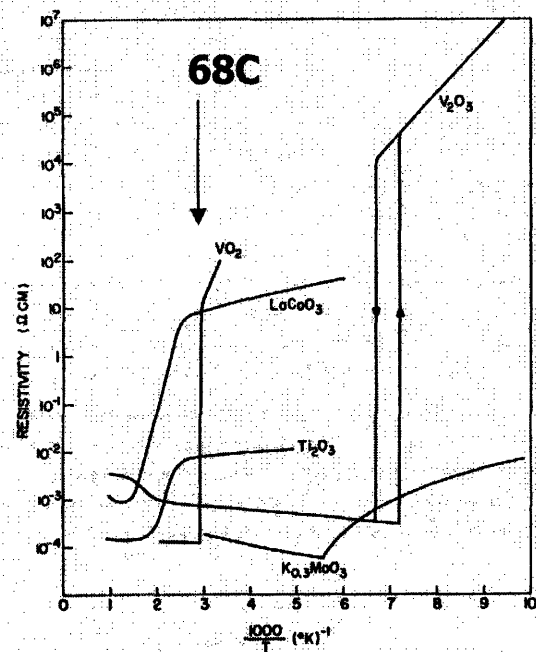


Figure 1-3 Resistivity data showing the metal-insulator transition in various transition metal oxides [80].

1.5 Structure and Properties of VO_2

VO_2 is one of a number of the oxides of vanadium. While its existence range has not been thoroughly characterized, x-ray measurements indicate a narrow existence range as shown in the phase diagram in Figure 1-4 [82]. The existence ranges for different vanadium oxides as a function of oxygen partial pressure and temperature are shown in

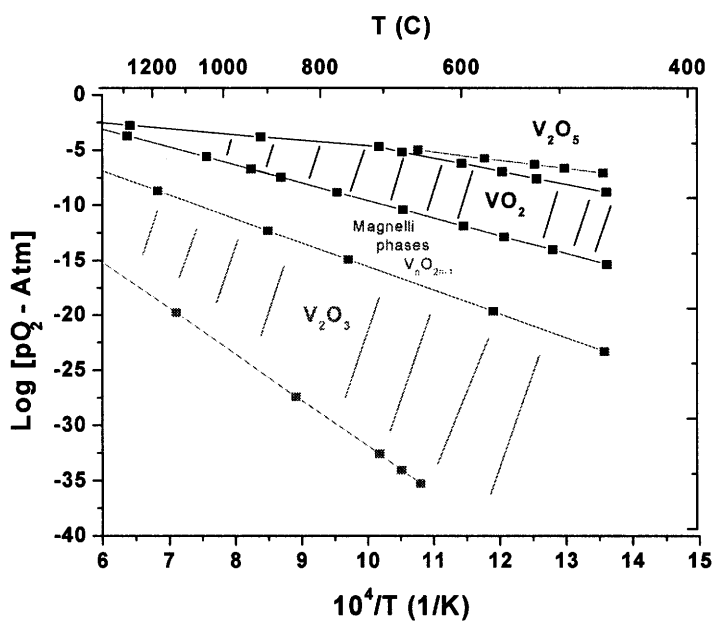


Figure 1-5 Existence ranges of the various vanadium oxide phases as a function of oxygen partial pressure and temperature [7].

VO₂ transforms at 68°C from the monoclinic phase to the high temperature tetragonal (rutile) phase. A schematic of the band structures in the tetragonal and monoclinic phases proposed by Goodenough [25] is shown in Figure 1-6(b).

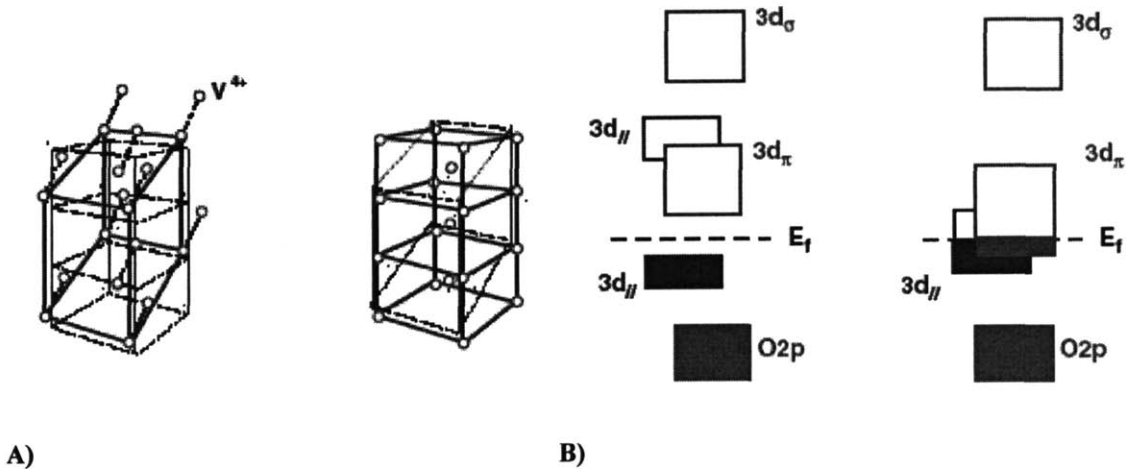


Figure 1-6 A) Monoclinic structure represented by bold lines on the left side and tetragonal crystal structure shown with bold lines on the right side. B) Schematic showing change in band structure associated with change in crystal structure: left side is the semiconducting phase band diagram and right side is the metallic band diagram. Taken from Cavalleri et al [9].

The vanadium atom, with configuration $[\text{Ar}] 4s^2 3d^3$, is bound to each of two oxygen atoms with configuration $1s^2 2s^2 2p^4$. Four electrons are taken up to fill the lower level oxygen 2p shells, leaving one electron in the d-orbital of the V^{4+} cation. The now closed shell O 2p levels are tightly bound, thus lying well below the Fermi level. The unpaired electron on the vanadium cation occupies the lowest 3d level. The 3d levels experience crystal field splitting, thereby dividing into 3 degenerate lower energy levels (t_{2g}) and two degenerate higher energy levels (e_g). It is believed [8, 25, 83] that the interaction between the c-axis vanadium atoms in the insulating state (M phase) leads to pairing-up of the vanadium cations along this direction. This dimerization or formation of $\text{V}^{4+} - \text{V}^{4+}$ pairs results in a further splitting of the 3 t_{2g} levels, due to lowering in energy of one of the $d_{||}$ orbitals. This separation in energy between one lower $d_{||}$ and the two higher energy orbitals, d_{π} and $d_{||}$ level, leads to a band gap of $\sim 0.7\text{eV}$.

1.5.1 Electrical and Optical Properties

There are numerous reports of the electrical conductivity measurements and optical transmission of VO_2 (of both bulk and thin films) near the transition temperature [80, 10, 79]. A comparison of some of the earlier work on single crystal VO_2 is shown in Figure

1-7. One notes significant variation in the values reported. The resistivity jump due to the phase transition ranges from 10^2 to 10^5 . The absolute values of the resistivities also differ significantly in the semiconducting phase, varying by as much as 10^2 .

The effect of stoichiometry on the electrical properties is significant. Kimizuka et al [34] reported the electrical resistivity change near the metal-insulator transition for single crystal whiskers grown between oxygen partial pressures of $10^{-2.9}$ and $10^{-4.1}$. The resistivity jump ranged from 10^4 for samples equilibrated at a pO_2 of $10^{-2.9}$ atm to 10^1 at the more reducing end. In addition, the absolute resistance and slope of the resistance versus inverse temperature is higher in the semiconducting phase for samples grown at the higher pO_2 , compared to those grown under the more reducing pressures. The difference in room temperature resistance is approximately 10^3 . An explanation for the observed differences is not provided in the report by Kimizuka [34].

The conducting specie in VO_2 is the electron, with carrier concentrations approximately 1×10^{18} carriers/cm³ in the semiconducting phase at room temperature. The carrier concentration was derived from Hall effect measurements on pressed powder samples of VO_2 by Kitahiro et al [36]. From the Hall coefficient and conductivity measurements, they derived a Hall mobility of $0.1 \text{ cm}^2/\text{Vs}$. In a separate report, Kitahiro and Watanabe [35] report a maximum thermopower value of $-900 \text{ } \mu\text{V}/\text{K}$ at room temperature. On separate measurements carried out on sputtered thin films, Kwan et al [38] report a maximum thermopower value of $-500 \text{ } \mu\text{V}/\text{K}$ at room temperature. The negative value implies n-type carriers (electrons). In the report by Kwan et al, the simultaneous measurements of electrical resistivity, thermoelectric power and Hall effect were performed as a function of the oxygen partial pressure in the chamber during sputter deposition. They also characterized the phases present in the thin films by measuring lattice spacing using transmission electron diffraction. They observed a minimum in the unit cell volume for films grown at an oxygen partial pressure of 1.3 mTorr. This minimum is attributed to the stoichiometric condition. They speculate, based on a similar observation by Magnelli in the TiO_2 system, that there is an expansion in the unit cell volume as one deviates from the stoichiometric point. In the oxygen-deficient regime, the lattice expansion in TiO_2 is attributed to Ti ions occupying interstitial sites. In the oxygen

excess regime, metal vacancies are generated, leading to Coulombic repulsions between neighboring oxygen anions, again leading to lattice expansion, compared to the stoichiometric composition. Likewise, Kwan speculates that, given the similarity between VO_2 and TiO_2 in the variation of the unit cell volume with oxygen partial pressure during deposition, the oxygen-deficient regime is dominated by vanadium interstitials and oxygen-excess regime is dominated by vanadium vacancies.

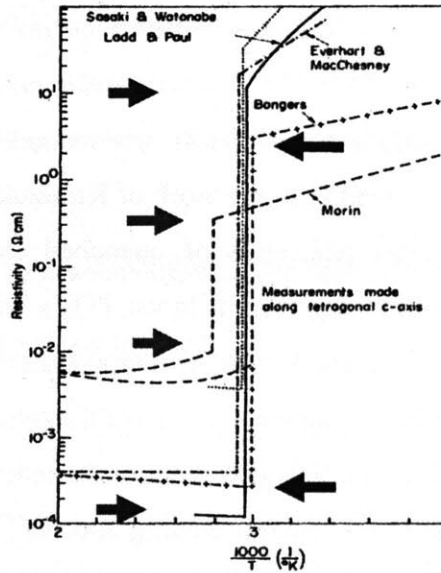


Figure 1-7 Compilation of resistivity data for single crystal VO_2 from different authors by Vest et al [80].

Several qualitative reports [10] of the effect of deposition conditions on optical properties of VO_2 also exist. These studies were performed on sputter deposited thin films of VO_2 with the oxygen partial pressure and temperature varied during deposition. These results, however, cannot be readily compared, as the reported percentage transmission depends on film thickness, substrate, substrate thickness etc. Given the lack of normalized data, such as absorption coefficient, comparisons between the different reports is not possible.

The index of refraction and loss (n and k) values were measured by Petit and Frigerio [57]. One observes significant difference in the indices in the metallic and semiconducting phases consistent with the phase change. It should be noted that the k

value (for example at 1550nm in the semiconducting phase), which is directly proportional to the absorption coefficient, is relatively high and corresponds to an absorption coefficient of approximately 10^4 cm^{-1} . This value is similar to band-edge (band-band) absorption in other semiconducting materials such as silicon and gallium arsenide. This high absorption value could thus be due to the low band gap energy of VO₂ in the low temperature phase which is reported approximately 0.7eV, corresponding to a band edge at 1770nm.

1.6 Defect model

The defect mechanisms in VO₂ are not clearly understood. The only indication of a possible defect mechanism is hinted at in the work of Kimizuka et al [34]. In their report, the room temperature electrical resistance of quenched single crystal specimens is observed to decrease for specimens grown at lower PO₂'s within the VO₂ single phase regime. This type of behavior is characteristic of n-type materials. TiO₂, which also has a tetragonal crystal structure at high temperatures, is well known in the literature [38,66] to be an n-type material with Ti interstitials dominant in the reducing (low PO₂) regime. At "high" PO₂'s, vacant Ti defects are the dominating species [38,66]. A similar model is proposed for VO₂.

In oxide semiconductors, the defect behavior requires consideration of the reactions involving reduction/oxidation, intrinsic lattice defect generation, intrinsic electron-hole pair generation, and ionization of donors/acceptors. In this analysis, VO₂ is assumed to be nominally undoped.

Assuming a model similar to TiO₂, the intrinsic Frenkel ionic disorder, assuming full ionization, and the corresponding mass-action law are given respectively by:

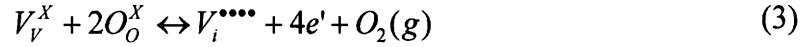


$$K_F = [V_i^{\bullet\bullet\bullet\bullet}][V_V^{\bullet\bullet\bullet\bullet}] = k_F \exp\left(\frac{-\Delta H_F}{kT}\right) \quad (2)$$

where $[V_i^{\bullet\bullet\bullet\bullet}]$ = the vanadium interstitial concentration, $[V_V^{\bullet\bullet\bullet\bullet}]$ = vanadium vacancy concentration, K_F = VO₂ Frenkel reaction equilibrium constant, k_F = the pre-exponential

constant, $\Delta H_F = \text{VO}_2$ Frenkel reaction enthalpy, $k = \text{Boltzman's constant}$, $T = \text{temperature}$.

The reduction reaction and its corresponding mass-action law are given by:



$$K_R = [V_i^{\bullet\bullet\bullet\bullet}] n^4 pO_2 = k_R \exp\left(\frac{-\Delta H_R}{kT}\right) \quad (4)$$

where $V_V^X = \text{vanadium cation on a cation site}$, $O_O^X = \text{oxygen on an anion site}$, $e = \text{electron}$, $n = \text{electronic carrier concentration}$, $pO_2 = \text{oxygen partial pressure}$, $K_R = \text{VO}_2 \text{ reduction reaction equilibrium constant}$, $k_R = \text{the pre-exponential constant}$, $\Delta H_R = \text{VO}_2 \text{ reduction reaction enthalpy}$.

The oxidation reaction and its corresponding mass-action law are given by:



$$K_O = [V_V^{\bullet\bullet\bullet\bullet}] p^4 (pO_2)^{-1} = k_O \exp\left(\frac{-\Delta H_O}{kT}\right) \quad (6)$$

where $h = \text{hole}$, $p = \text{hole carrier concentration}$, $K_O = \text{VO}_2 \text{ oxidation reaction equilibrium constant}$, $k_O = \text{the pre-exponential constant}$, $\Delta H_O = \text{VO}_2 \text{ oxidation reaction enthalpy}$.

Electron-hole pair generation and the corresponding mass-action law are given by:



$$K_E = np = k_E \exp\left(\frac{-E_g}{kT}\right) \quad (8)$$

where $K_E = \text{electronic disorder reaction equilibrium constant}$, $k_E = \text{the pre-exponential constant}$, $E_g = \text{VO}_2 \text{ bandgap}$.

Overall, the requirement for charge neutrality leads to:

$$4[V_V^{\bullet\bullet\bullet\bullet}] + e' \leftrightarrow h^\bullet + 4[V_i^{\bullet\bullet\bullet\bullet}] \quad (9)$$

Given the relatively small bandgap of VO_2 , electronic defects are expected to dominate in the near-stoichiometric regime. The *stoichiometric* composition occurs at the point at which:

$$[V_V^{''''}] = [V_i^{••••}] \quad (10)$$

However, in the *near-stoichiometric regime*, charge neutrality is dominated by the majority carriers and is given by:

$$n = p = \sqrt{K_E} \quad (11)$$

Combining this with equation 6 an expression for the vanadium vacancy generation can be derived. This gives:

$$[V_V^{''''}] = \frac{K_O}{K_E^2} pO_2 \quad (12)$$

Similarly, an expression for the vanadium interstitial concentration in this near-stoichiometric regime can be found by substituting equation 12 in equation 2 which gives:

$$[V_i^{''''}] = \frac{K_F K_E^2}{K_O} (pO_2)^{-1} \quad (13)$$

Under high PO_2 conditions, the charge neutrality condition can be approximated involving only holes and vanadium vacancies (see equation 5):

$$p \cong 4[V_V^{''''}] \quad (14)$$

Substituting this into the mass-action expression for the oxidation reaction, equation 6 gives:

$$p \cong 4[V_V^{''''}] \cong (4K_O)^{1/5} (pO_2)^{1/5} \quad (15)$$

The electron concentration in this regime can then be found by substituting this equation in the expression for electronic disorder, equation 11, giving:

$$n \cong \frac{K_E}{(4K_O)^{1/5}} (pO_2)^{-1/5} \quad (16)$$

The vanadium interstitial concentration, in the oxidizing regime, can then be found by combining equation 15 with equation 2, which gives:

$$[V_i^{\bullet\bullet\bullet}] \cong \frac{4K_F}{(4K_O)^{1/5}} (pO_2)^{-1/5} \quad (17)$$

Using a similar treatment, the concentrations of the defects in the reducing regime can be obtained. The relevant approximation for the reducing regime is:

$$n \cong 4[V_i^{\bullet\bullet\bullet}] \quad (18)$$

A complete list of the defect concentrations in the three regimes is given in Table 3.

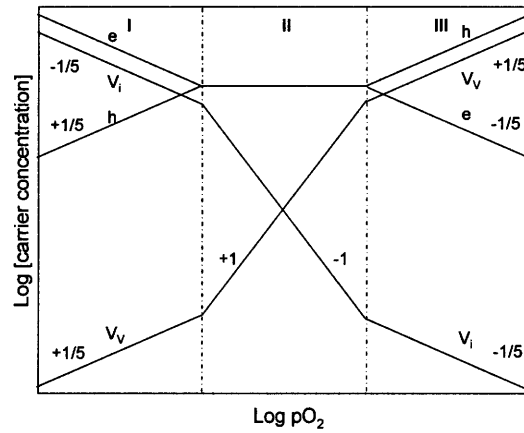


Figure 1-8 Brouwer diagram for VO₂ based on the defect equations in Table 3.

Table 3 Defect equations in different regions of oxygen partial pressure for VO₂.

Electrical Carrier	Regime I – Reducing $n \cong 4[V_i^{\bullet\bullet\bullet\bullet}]$	Regime II-Near Stoichiometry $n \cong p$	Regime III-Oxidizing $p \cong 4[V_V^{\bullet\bullet\bullet\bullet}]$
n	$(pO_2)^{-1/5} (4k_R)^{1/5} \exp\left(-\frac{\frac{1}{5}\Delta H_R}{kT}\right)$	$k_E \exp\left(-\frac{\frac{1}{2}E_g}{kT}\right)$	$(pO_2)^{-1/5} \frac{k_E}{(4k_O)^{1/5}} \exp\left(-\frac{E_g - \frac{1}{5}\Delta H_O}{kT}\right)$
p	$(pO_2)^{1/5} \frac{k_E}{(4k_R)^{1/5}} \exp\left(-\frac{E_g - \frac{1}{5}\Delta H_R}{kT}\right)$	$k_E \exp\left(-\frac{\frac{1}{2}E_g}{kT}\right)$	$(pO_2)^{1/5} (4k_O)^{1/5} \exp\left(-\frac{\frac{1}{5}\Delta H_O}{kT}\right)$
$[V_i^{\bullet\bullet\bullet\bullet}]$	$(pO_2)^{-1/5} \frac{(4k_R)^{1/5}}{4} \exp\left(-\frac{\frac{1}{5}\Delta H_R}{kT}\right)$	$(pO_2)^{-1} \frac{k_F k_E^2}{k_O} \exp\left(-\frac{\Delta H_F + 2E_g - \Delta H_O}{kT}\right)$	$(pO_2)^{-1/5} \frac{4k_F}{(4k_O)^{1/5}} \exp\left(-\frac{\Delta H_F - \frac{1}{5}\Delta H_O}{kT}\right)$
$[V_V^{\bullet\bullet\bullet\bullet}]$	$(pO_2)^{1/5} \frac{4k_F}{(4k_R)^{1/5}} \exp\left(-\frac{\Delta H_F - \frac{1}{5}\Delta H_R}{kT}\right)$	$(pO_2) \frac{k_O}{k_E^2} \exp\left(-\frac{\Delta H_O - 2E_g}{kT}\right)$	$(pO_2)^{1/5} \frac{(4k_O)^{1/5}}{4} \exp\left(-\frac{\frac{1}{5}\Delta H_O}{kT}\right)$

1.7 Application of Defect Model

The defect model presented in the table and figure above provide a framework for characterizing the type and concentration of defects and their dependencies on temperature and PO₂. The defect model can, in principle, be determined from an analysis of the total bulk electrical conductivity as a function of the key variables. The total electrical conductivity, defined below, is a summation of all the charge carrying defects listed in Table 3.

$$\sigma_{total} = \sum_i (Z_i q) c_i \mu_i \quad (19)$$

Where Z_i is the valence, q is the elementary charge, c_i is the concentration, and μ_i is the mobility of i^{th} specie.

As observed in Figure 1-8, each specie has a particular dependence on the oxygen partial pressure and temperature within each defect regime. The electrical conductivity will, therefore, also have a partial pressure dependence corresponding to the most conductive defect specie in the particular oxygen partial pressure regime. Thus, electrical conductivity measurements as a function of PO₂ and temperature can, in general, be used to determine the defect regime of VO₂ and therefore, the dominant defect specie. In addition, the activation energy for electrical conductivity can be extracted from the temperature dependent measurements. The activation energy can, with the assistance of the defect model, then be used to extract the energetics of the relevant defect reactions.

The type and magnitude of the conducting electrical specie can be determined from thermoelectric power (TEP) measurements. In TEP measurements, the voltage induce by an imposed temperature gradient is measured. The TEP coefficient is defined by:

$$\alpha = \frac{dV}{dT} \quad (20)$$

Where α = TEP coefficient, dV = induced voltage gradient, dT = temperature gradient.

The TEP coefficient for electrons is related to the carrier concentration by [37]:

$$\alpha = -\frac{k}{q} \left[\ln \frac{N_c}{n} + \frac{H}{kT} \right] \quad (21)$$

For holes, the corresponding equation is given by:

$$\alpha = -\frac{k}{q} \left[\ln \frac{N_V}{p} + \frac{H}{kT} \right] \quad (22)$$

where N_C and N_V are the density of states in the conduction and valence band respectively, H is the heat of transport, k = Boltzman's constant, and q = elementary charge. In oxide semiconductors, H , is usually small and can be neglected according to Tuller and Nowick [77].

By independently deriving the carrier concentration from analysis of the TEP measurements, the mobility of the conducting specie i , in equation 19, can then be derived from a corresponding measurement of conductivity.

1.8 Electro-Optic Optical Modulation

Electro-optic (E-O) modulators play a major role in optical communications systems. An optical modulator is used to convert a digital electrical signal carrying 1's and 0's to an optical signal. Modulators are based on intensity modulation, where peak intensity will correspond to a 1 bit and minimum intensity corresponding to a 0 bit. Given that information is generated at the speeds of 100's to 1000's of Mbits per second (Mbps), the modulator operation needs to be in the 100's of Giga hertz frequency to Tera hertz frequency range. Given this required *switching* speed, modulation of electro-optic ferro-electric crystals, specifically single crystal LiNbO₃, is the current industry standard. The intrinsic *switching* speed of LiNbO₃ is of the order of picoseconds.

The integration of a modulator with light sources, waveguides and detectors is also a key need for achieving photonic integrated circuits. This requires translation of bulk crystal properties into the thin film form. LiNbO₃'s present predominant use as E-O modulator material is based on its ability to be grown as large, high quality single crystals. For integration onto Si, and where the ability to grow large single crystals is unimportant, KNbO₃ and BaTiO₃, have the potential for more desirable properties, such as much higher electro-optic coefficients, higher data rates and/or lower operating voltages. In

particular, BaTiO₃ (BT) is a prime candidate due to its high electro-optic coefficient ($r_{42}=820$ pm/V compared to $r_{33}=30$ pm/V for LiNbO₃). One of the expectations in the drive towards integrated photonics is device miniaturization thus enabling large scale integration. However, given the best electro-optic coefficient of LiNbO₃, $r_{33}=30$ pm/V, the modulation device size required is large; approximately 40mm in length, a dimension not acceptable for large scale integration. Thus, a material with a higher electro-optic coefficient, in thin film form, is needed and hence the emphasis on BaTiO₃.

In order to utilize its high electro-optic coefficient, BT has to be grown epitaxially or highly (001) oriented. In recent years, much progress has been achieved in growing high quality epitaxial ferroelectric oxide films, including BaTiO₃, onto Si for the purpose of developing nonvolatile memory devices. The combination of a high electro-optic coefficient, and the ability to grow high quality BT films, points to the feasibility of integrating thin film optical modulators onto a Si-based device platform.

The electro-optic modulator is an intensity modulator, which works based on phase shifting the signal from one arm of a Mach-Zhender structure by some angle ϕ compared to the other arm. An applied electric field applied across the electro-optic material induces a change in the real part of the refractive index:

$$n(E) = n - \frac{1}{2}n^3 E * r_{ijk} \quad (23)$$

where $n(E)$ = electric field dependent real part of the refractive index, n = real part of refractive index, E = applied electric field, and r_{ijk} = electro-optic tensor value. Given that the wave velocity is inversely dependent on n , the waves in the two arms of the Mach-Zhender structure will experience a relative phase shift resulting from the field-induced index change in one of the arms. The phase change is given by:

$$\phi = \frac{2\pi L}{\lambda} n(E) \quad (24)$$

Where ϕ = phase, L = device length, λ = wavelength. For a π phase shift, the voltage that needs to be applied is given by:

$$V_{\pi} = \frac{\lambda d}{n^3 r_{ijk} L} \quad (25)$$

Where V = voltage applied.

A schematic of an intensity modulator based on the Mach-Zhender design is shown in the Figure 1-9 below.

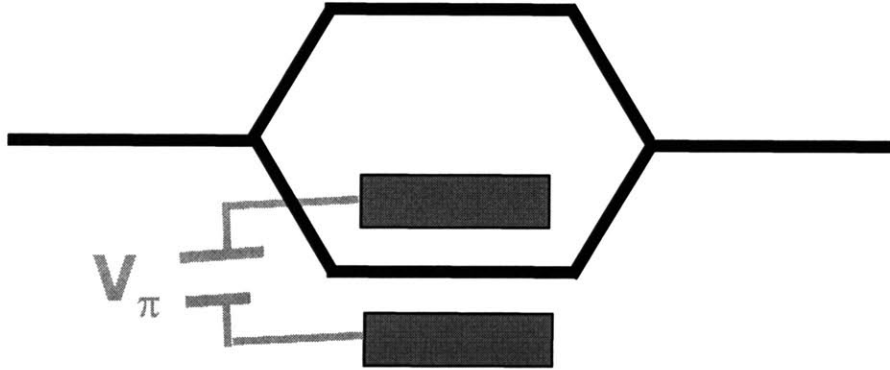


Figure 1-9 Schematic of the Mach-Zhender modulator configuration.

There are several reports in the literature on the development of BT-based thin film modulators. Petraru et al [58, 59] fabricated a BT thin film modulator on MgO substrates and demonstrated an effective electro-optic coefficient of 22 pm/V. BT films were deposited by pulse laser deposition. Gill et al [23, 24] also fabricated BT based thin film modulators on MgO. Their films were deposited by a metal-organic chemical vapor deposition process (MO-CVD). Gill et al [24] report an effective electro-optic coefficient of 50 pm/V in DC operation. Subsequent work by the same group demonstrated significantly higher electro-optic coefficients. Tang et al [69-74] reported an effective electro-optic coefficient of 360 pm/V in DC operation at 1561 nm.

A key objective in this section of the thesis was to develop an electro-optic modulator with comparable or superior performance to those reported in the literature and to demonstrate the ability to ultimately integrate such devices onto Si wafers.

Chapter 2: Objectives

As discussed earlier, the current available optical switch design for OADM applications have several drawbacks which prevent ready use in photonic integrated circuits (PIC). PIC's require device size that are compatible with large scale integration (area no more than several square microns per switch), CMOS compatible fabrication processes, minimal power consumption (less than 1 mW per device), minimal insertion losses and at least 15dB extinction ratios. In addition, for reconfigurable OADM's switching speeds faster than 1 ms are desired.

On the other hands, for modulation, the most important device requirement is speed. A switching/modulation speed of pico seconds is desired. None of the current switches designed for OADM applications can be used for modulation due to their limited switching speeds. The only viable available option is switching/modulation based on electro-optic ferro-electric materials. Therefore, two independent approaches are undertaken: one for the slower switching function for OADM's and the other a fast switch for optical modulation. Henceforth, the fast switch will simply be referred to as the E-O modulator and the slower switch for OADM application will be referred to as a switch.

2.1 Optical Switching

A ring resonator based optical switch design was identified as a possible solution to the slower switching function. Despite the relatively slow switch speeds reported for MEMS-based optical switches in the literature, the approach taken in this thesis will be MEMS-based. The advantageous design of the ring resonator, having a small device size (approximately 10's of microns), low insertion losses and potentially large extinction ratios, coupled with appropriate design of the MEMS component of the switch will lead to a successful switch design. The first switch solution investigated will be the MEMS-based approach. As a potential enhancement of the MEMS switch design, an alternate approach, utilizing the metal-insulator transition in VO_2 will be explored. The metal-insulator transition in VO_2 is known to occur at pico second timescales. Thus, a VO_2 based switch can in principle provide one unified solution to both switching and

modulation. In order for the VO₂ switch to be realized, however, the properties of VO₂ need to be characterized.

2.1.1 MEMS-based switch

For the MEMS-based switch, the mechanical structure design is critical for the performance of the ring resonator switch. To this end, finite element modeling will be carried out to design and optimize the mechanical structure to meet the required switching speed, operating power and device size. The optimized designs will be fabricated and tested.

The main objective of the MEMS switch approach is to design a switch having switching speeds faster than 1 ms, drive voltages close to 5 V, and device area no more than several 1000's um². The designs then need to be fabricated using CMOS compatible materials and process steps and tested, to prove the concept of MEMS-based optical switching of ring resonators.

2.1.2 Vanadium Oxide Objectives

As discussed above, a review of the literature finds that the resistivity jump associated with the MIT effect in VO₂ can vary by several orders of magnitude. Various authors have made attempts to pinpoint the cause of the scatter in the data, but all of the reports are qualitative in nature. The actual defect mechanism in VO₂ has not been experimentally determined. As was mentioned in section 1.6, the defect mechanism is speculated to involve vanadium interstitials in the reducing regime and vanadium vacancies in the oxygen excess regime. No systematic studies have been performed to establish the defect model for this system.

As was discussed in section 1.6 and 1.7, the electrical properties may be significantly influenced by the oxygen partial pressure. The deviation from stoichiometry commonly results in the generation of excess electronic carriers to compensate for resulting ionic defects in a manner similar to excess carriers induced by extrinsic shallow donors or acceptors. As a result, nonstoichiometric VO₂ can be expected to exhibit a considerably higher free carrier concentration than the stoichiometric composition and thereby have a lower resistivity ratio between the metallic and semiconducting phases. For applications

in photonics, a high switch contrast (resistivity ratio between metallic and semiconducting phases) is required. Therefore, determining the partial pressure of oxygen at which VO_2 is stoichiometric, which in turn corresponds to the minimum free carrier concentration, is desirable.

In this thesis, a quantitative defect model of VO_2 is developed by examining the temperature and partial pressure dependent electrical conductivity, thermopower and nonstoichiometry. Given that the higher temperature phase is metallic, the detection of changes in conductivity due to stoichiometry changes is limited. An approach was therefore developed to freeze stoichiometry to below the phase transition and characterize the transport properties in the semiconducting phase. A unique contribution of this thesis will be the direct correlation between non-stoichiometry, δ , in $\text{VO}_{2-\delta}$ and the associated electrical and optical properties. The extent of non-stoichiometry under controlled conditions of temperature and oxygen partial pressure is experimentally determined with the aid of coulometric titration measurements.

An additional key objective of this thesis is to establish the influence of non-stoichiometry on carrier density and, in turn, the optical properties of VO_2 . The effect of free carrier concentration on optical properties will be characterized by optical transmission measurements.

2.2 Optical Modulator Objectives

Given the need for a fast switch and lack of any suitable switch design from OADM solutions, barium titanate based materials will be explored in order to utilize their electro-optic effect for optical modulation.

The objective in this part of the thesis is to develop a thin film electro-optic modulator based on BaTiO_3 . Given the high degree of anisotropy in the electro-optic coefficient in BT, its films need to be grown with controlled film orientation. The optimum orientation is (001). The quality of the BT films will be characterized by measuring the electro-optic effect. In order to characterize the electro-optic effect Mach-Zehnder (MZ) structures will be fabricated. In addition to enabling the characterization of the electro-optic effect of BT films, test of the MZ structures should demonstrate the concept of thin film optical

modulation. The overall goal in this part of the thesis is to demonstrate a working thin-film electro-optic device.

Chapter 3: Experimental

This chapter consists of three main parts, covering:

1. Experimental work on the development of MEMS-based wavelength selective optical ring resonator switches
2. Development of a barium titanate based thin film electro-optic modulator
3. Characterization of the transport properties of vanadium (IV) oxide.

3.1 MEMS-based Optical Switch

Switching of the optical ring-resonators described in the introduction was carried out using a micro-mechanical structure designed for this purpose.. The key objectives were to design an appropriate micro-mechanical structure, develop a fabrication sequence that utilizes CMOS-compatible process and test the fabricated devices.

3.1.1 Optical Design Requirements

Optical design criteria were derived based on calculations prepared by Mike Watts in the Ultra-fast Optics Group at MIT [81]. Key requirements included that the membrane material should have a real refractive index as close as possible to the waveguide material and that the imaginary index (related to the absorption coefficient) of the material should be between 0.1 and 10. The waveguides used in optical ring-resonator were fabricated from Si_3N_4 . The real index of the Si_3N_4 was 2.1.

For the case of Si_3N_4 waveguides, the absorbing membrane needs to be at least $1.2 \mu\text{m}$ away from the ring in the “off” state and less than $0.2\mu\text{m}$ away in the “on” state (Figure 1-2). These calculations were based on the assumption that the absorbing material has a thickness of at least $0.2 \mu\text{m}$.

3.1.2 Mechanical Design Requirements

The mechanical structure chosen for the switch is an end-fixed beam (also referred to as fixed-fixed beam). This structure is generally known to give symmetric deflection about the center. The deflection of an end-fixed beam under a uniform electrostatic load is described through the following equation [65]:

$$m\ddot{x} + b\dot{x} + kx = \frac{\varepsilon AV^2}{2(g_0 - x)^2} \quad (26)$$

where x = displacement of the mechanical structure, m = mass of the moveable structure, b = damping coefficient, k = effective spring constant of structure, ε = permittivity of the region between the electrodes, A = overlap area of the (moveable) mechanical structure and static electrodes, V = voltage, and g_0 = initial effective gap between the two electrodes. Given the static electrode was a back contact on the silicon substrate, g_0 is composed of the air gap and the dielectric layers (silicon oxide and silicon substrate) between the moveable structure and the back contact.

The membrane was designed to pull-in at the extreme end of the mechanical deflection. It is known that a fixed-fixed membrane deflected beyond 1/3 of the total displacement gap, pulls-in [65]. The voltage required to pull-in a fixed-fixed beam is given by:

$$V_{PI} = \sqrt{\frac{8kg_0^3}{27\varepsilon A}} \quad (27)$$

The design of the beams was carried out using a commercial FEM tool, Coventorware [14]. The mechanical designs of the structures were optimized to minimize the pull-in voltage [51]. The spring constant of the mechanical structure depends on its material stiffness. A large stiffness value will lead to high drive voltages. On the other hand, too low a spring constant will result in low natural frequencies, thus limiting the switch speed. Aluminum (Young Modulus = 70 GPa) was chosen as the initial choice for the mechanical structure.

3.1.3 Switch Fabrication

CMOS-compatible processing steps were used to fabricate the MEMS switch. The waveguides and ring resonators were pre-fabricated by Tymon Barwicz [2] at MIT.

A schematic of the fabrication sequence is shown in Figure 3-1. A detail list of processing steps is tabulated in Table 4.

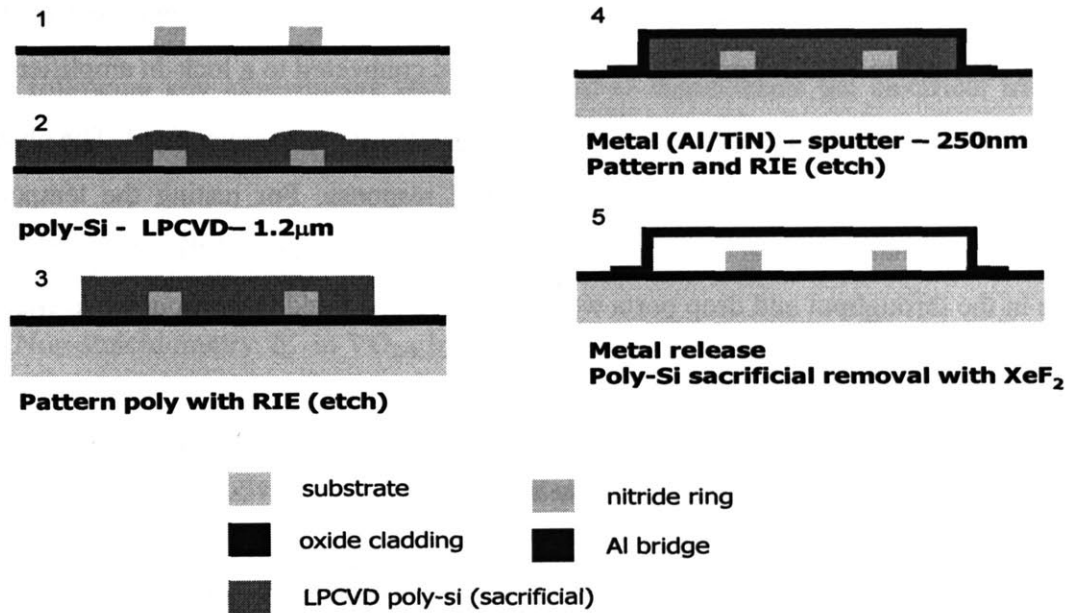


Figure 3-1 Schematic showing the fabrication sequence for fabricating the MEMS ring-resonator switch.

3.1.4 Residual Stress Characterization

Control of the residual stresses in thin films is critical to the performance of mechanical structures within MEMS devices. The fixed-fixed beams used in this design were particularly sensitive to residual stresses. The residual stress of the active mechanical component, Al or TiN, was characterized using a Tencor FLX curvature measurement tool. This tool was used to measure the bow of the substrate before and after deposition of the film. The stress in the film is then calculated using the Stoney formula for calculating thin film stresses on substrates.

3.1.5 Optical Switch Testing

Testing of the fabricated optical switch was carried in the Ultra-fast Optics Group at MIT. The test setup consists of a signal generator which is used to drive a tunable laser source. The laser output is coupled through a polarization controller and onto a lens-tipped optical fiber. The MEMS switch is mounted on a probe-station. Micro-probes are used to contract the metal pads on the MEMS device. The optical fiber is aligned with the input waveguide of one of the devices. The output from the drop or the throughput guide

is focused via a lens onto a mirror which can be switched to a CCD camera or to a photo-detector. The photo-detector and signal generator and connected to a lock-in amplifier.

The spectral and temporal responses of the optical switch were characterized. The above mentioned setup was used for testing the spectral response. For testing the temporal response, the signal generator was used to drive a voltage source and the corresponding change in the throughput and drop ports were measured at a fixed laser input wavelength.

Table 4 Detailed step-by-step list of the process steps for fabricating the MEMS optical switch.

Names within parenthesis refer to MTL's machine names.

1. Deposit Oxide on brand new wafers in ICL.	a. Wafer clean (rcaICL) b. Grow oxide (6C-LTO)
2. Deposit poly-silicon in ICL	a. Wafer clean (rcaICL) b. Grow poly (6A-Poly)
3. Pattern resist in TRL with contact mask	a. HMDS coat (HMDS-TRL with green cassette) b. Coat wafers with resist (coater with green chuck) c. Pre-bake (pre-bake with green cassette) d. Contact aligner using EV1 (EV1 with green chuck and mask plate) e. Develop resist (photo-wet with green labware) f. Postbake (post-bake with green cassette)
4. Etch poly in ICL	Dry etch poly with (AME5000 chamber B) Strip resist in asher (asherICL)
5. Pre-metal clean before Endura sputter step #6	Piranha clean (premetal-Piranha)
6. Sputter Al on Endura (Endura)	
7. Pattern resist in TRL with contact mask.	Same as step #3
8. Etch Al in ICL	a. Wet Etch (TRL-Acidhood2) b. Strip resist in asher (asherTRL)
9. Release Al structures in TRL	a. Release structures by sacrificial removal of poly-silicon (XeF2)

3.2 Vanadium (IV) Oxide

The following key experiments were performed to characterize the electrical transport, thermodynamic and optical properties of VO₂:

1. Electrical conductivity and thermoelectric power as a function of temperature and oxygen partial pressure
2. Non-stoichiometry, δ , in VO_{2- δ} by coulometric titration measurements
3. Optical absorption as a function of stoichiometry.

For electrical conductivity and thermoelectric power measurements, bulk specimens were used. For optical absorption measurements, thin film specimens were used.

3.2.1 Sample Preparation

3.2.1.1 Bulk sample preparation and mounting

Bulk, polycrystalline samples, prepared for the electrical conductivity and thermoelectric power measurements, were processed by conventional ceramic processing routes as described in the following paragraph.

The bulk specimens were made by uniaxially pressing V₂O₃ powders (Alfa-Aesar purity 95%) into pellets 3/4" in diameter and 5 mm thick. Each as-pressed pellet was sealed inside a plastic bag in preparation for cold-isostatic pressing (CIP). The cold-isostatic pressing was performed at room temperature. The pellets were pressed to a pressure of 40,000 psi. The pellets were then sintered at 850°C for six hours in a 1000 ppm carbon monoxide balance carbon dioxide atmosphere. The post-sintered phase is V₂O₃.

The pellets were then diced into rectangular bars measuring 2-4 mm in width and thickness and approximately 10 mm in length. The pellets were then prepared for 4-point electrical conductivity measurements. The same samples were used for the thermoelectric power (TEP) measurements.

The pellets were then electroded by applying platinum ink (Engelhard #6082 [18]) to the specimen on lines spaced approximately 2-3 mm apart (see Figure 3-2). Platinum wire, 0.01 inch diameter, was then wrapped around each electrode to complete the contact. In

addition, to the 4 platinum wires, one additional platinum-10% rhodium wire was attached to the platinum wire at each end of the sample. This Pt-10%Rh/Pt junction forms an S-type thermocouple used to measure sample temperatures during electrical conductivity measurements and temperature gradients during thermoelectric power measurements. Each lead was then fed through a ¼” 6-bore alumina rod. The end of the alumina rod extending out from the flange sealing the end of the alumina sample tube was sealed using silicone to prevent gas leaks through the open bores at the room temperature end of the rod.

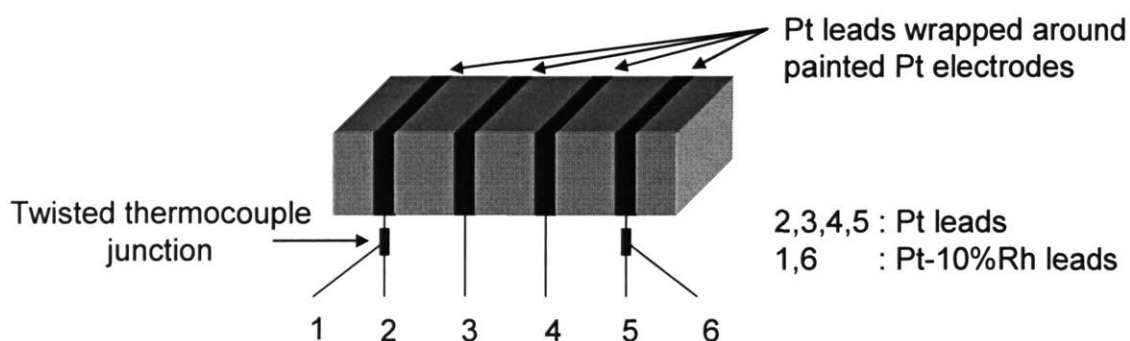


Figure 3-2 Schematic of the bulk sample arrangement for electrical conductivity and thermoelectric power measurements.

3.2.2 Thin Film Sample Preparation

3.2.2.1 VO₂ Film deposition - Pulse Laser Deposition

VO₂ thin films were grown using pulse laser deposition. Pulse laser deposition (PLD) is a high vacuum physical vapor deposition process. The process is similar to sputtering, but the ablation of the target is accomplished by using a laser (Lamda Physik COMPeX Pro™ laser operating at $\lambda=248$ nm) instead of a plasma. The ablation of the target creates a plume which deposits on the substrate. Films can be deposited at high temperature by heating the substrate.

A schematic of the PLD setup used is shown in Figure 3-3. A set of focusing lenses is used to focus the laser beam onto the target. The focusing lens is moved in such a way as to raster the laser beam on the target. This rastering enables uniform wear of the target.

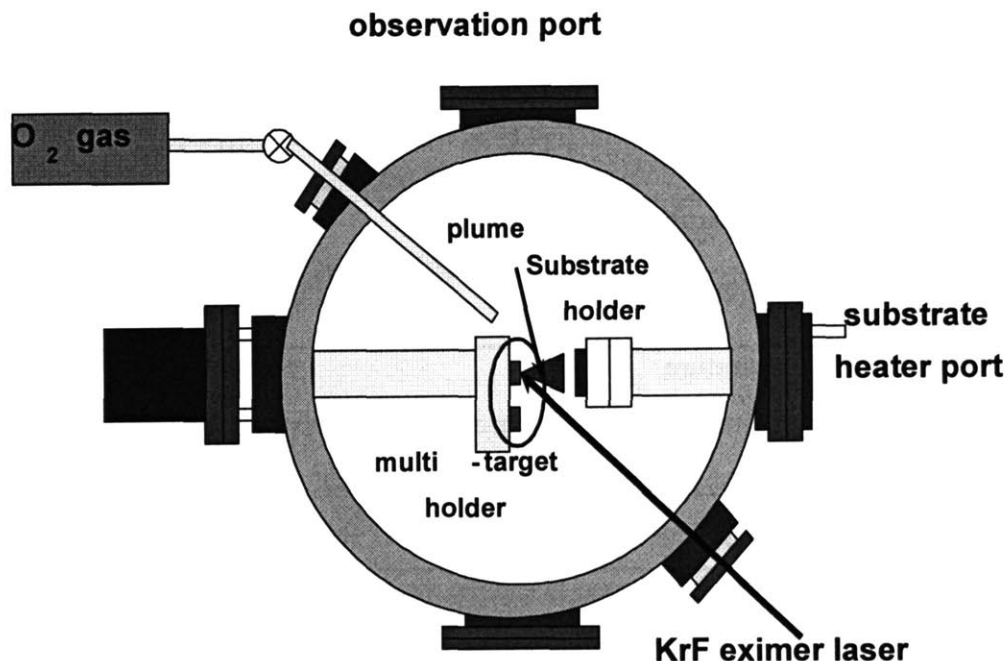


Figure 3-3 Schematic of the pulse laser deposition system.

The substrates used for deposition of the VO₂ films were fused quartz substrates (supplied by Finkenbeiner and Waferworld) and (100)-oriented single crystal magnesium oxide (MgO) substrates. The substrates were cleaned in the following sequence: acetone, distilled water, methanol, water, and iso-propylalcohol (IPA). The as cleaned samples were then immediately loaded into the vacuum chamber and pumped down. The target used for VO₂ film deposition was V₂O₅. The deposition conditions for growth of VO₂ films are listed in Table 5:

3.2.2.2 Electrode deposition for electrical characterization

Four 100 nm thick parallel platinum electrodes, deposited by sputtering, were used for the characterization of the electrical conductivity of the VO₂ thin films. The electrodes were 1.5mm wide. The spacing between each electrode was 3 mm. The outer electrodes were used to apply current and the inner electrodes were used to measure the voltage drop. Given that the electrode spacing is much larger than the thickness of the film, the entire thickness of the film can be assumed to be part of the geometrical factor in the expression for calculating electrical conductivity.

Table 5 Pulse laser deposition conditions.

Property	Value
Base Pressure	2×10^{-6} Torr
Total Working Pressure	4×10^{-3} Torr
Deposition ambient	Pure oxygen gas
Substrate Temperature	600°C
Fluence	5 J/cm ²
Pulse rate	20 Hz

3.2.3 Physical Characterization

3.2.3.1 X-ray diffraction

X-ray diffraction was used to characterize the phase and structure of bulk and thin film VO₂ samples. A Rigaku-300 [62] copper rotating anode source with 185mm spacing of source-sample-detector was used. Cu K_α radiation was generated using an accelerating voltage of 50kV and current of 300mA. For both the bulk and thin film measurements, θ - 2θ reflection measurements were performed. For bulk measurements, the sample was ground into a powder and pressed onto a roughened glass slide. A few drops of water helped bind the powder together and prevented it from falling off when the glass slide was mounted vertically during the x-ray measurement. For thin film samples, the substrate was mounted using modeling clay.

In-situ measurements of the phase transition of VO₂ as a function of PO₂ were performed at Alfred University by Scott Misture, one of our collaborators. The experimental setup is described in detail in the paper by Dollan and Misture [15].

3.2.3.2 Electron Microscopy

Electron microscopy is a powerful tool for physical inspection of the microstructure of materials. A Philips Field Emission Electron Microscope (XL30 FEG ESEM) was used for microstructure analysis of the thin films.

3.2.4 Electrical Characterization

3.2.4.1 Bulk Conductivity

The DC electrical conductivity was measured in both bulk and thin film samples. In the bulk measurements, the electrical conductivity was measured as a function of oxygen partial pressure and temperature. The 4-point measurements (see Figure 3-2) help nullify any contact resistance problems due to imperfect contacts. In this arrangement, current is passed through the outer leads and the voltage measured between the inner leads. The current, which ranged between 0 mA and 100 mA was applied in linear steps of 20 mA. The slope of the voltage versus current plot gives the resistance of the sample at that particular oxygen partial pressure and temperature. The electrical conductivity is then obtained from:

$$\sigma = \frac{l}{RA} \quad (28)$$

Where l is the spacing between the inner (voltage measuring) electrodes, A is the cross-sectional area of the bulk sample and R is the slope of the voltage-current plot.

A zirconia-based oxygen sensor (closed-end tube) was placed next to the bulk sample, to accurately measure the oxygen partial pressure. A schematic of the electrical conductivity setup is shown in Figure 3-4.

3.2.4.2 Thermoelectric Power Measurements

Thermoelectric power (TEP) measurement can be used to obtain insight regarding the type of carrier and the magnitude of the carrier density. In this measurement, a temperature gradient is imposed across the specimen and the

corresponding potential that develops is recorded. The slope of built-in-potential versus temperature-gradient plot gives the thermopower coefficient.

The temperature gradient in the bulk samples was induced using resistance wire made of Kanthal. A Keithley 2425 power source was used to apply a voltage between 0V and 5V in linear steps of 0.5 V. The electrical potential due the temperature gradient was measured simultaneously with the temperature at the two ends of the bulk specimen.

Carrier densities were derived by evaluating the TEP data with the assistance of Eq. 21 by assuming values for the effective density of states and neglecting the heat of transport factor. The heat of transport is usually small in semiconducting oxides and can be neglected according to Tuller and Nowick [77]. A negative value of thermoelectric power coefficient indicates n-type carriers while a positive value indicates p-type carriers.

3.2.4.3 Oxygen Partial Pressure Control

Control of the oxygen partial pressure were achieved by mixing gases, or by the use of an oxygen pump. To obtain oxygen partial pressures great than 10^{-6} atm, pre-mixed tanks of argon and oxygen were be used. To obtain lower oxygen partial pressures, mixtures of carbon monoxide and carbon dioxide were used.

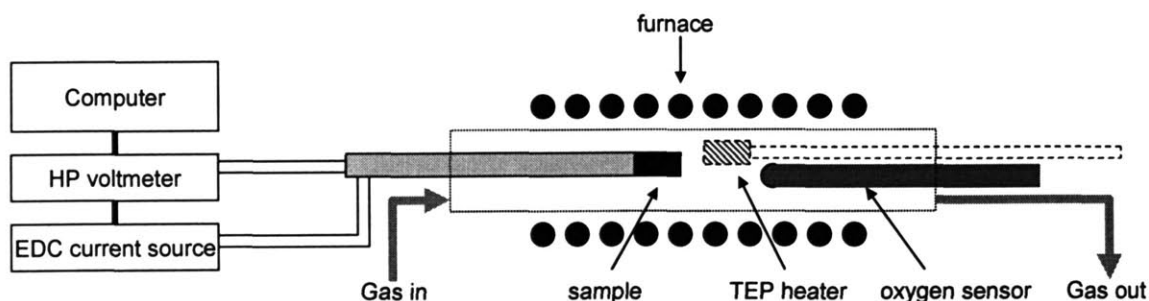


Figure 3-4 Schematic of the electrical conductivity setup for bulk samples.

However, with the least reducing CO/CO₂ mixture available (10 ppm CO/balance CO₂) the highest oxygen partial pressure obtainable is $\sim 1 \times 10^{-13}$ atm at 600°C. VO₂, however, is stable only between 10^{-13} and 10^{-7} atm at this temperature. Therefore, to access this interim regime, an oxygen pump was used.

The oxygen pump used was similar to that described by Stefanik [67]. The oxygen pump is made of a 3/4" diameter zirconia tube open at both ends. A 1000 ppm CO/Balance CO₂ mixture was used as a carrier gas which was caused to flow through the zirconia tube. The outside surface of the zirconia tube was exposed to air. The zirconia oxygen pump tube was heated to 800°C in a separate furnace, upstream from the samples being measured. Oxygen was pumped into this gas stream by applying a positive current between the outer and inner surfaces of the zirconia tube. The rate of oxygen pumped is controlled by the current applied. The oxygen sensor placed next to the measurement samples, mentioned in section 3.2.4.1, was used as a feedback sensor. The closed-loop system was controlled using a commercial PID controller (Omega CN825 controller – [53]). In order to provide a high input impedance into this Omega controller, a separate amplifier circuit was designed and assembled by David Bono, the Undergraduate Laboratory Manager at MIT within DMSE. A schematic of the circuit is shown in Figure 3-5.

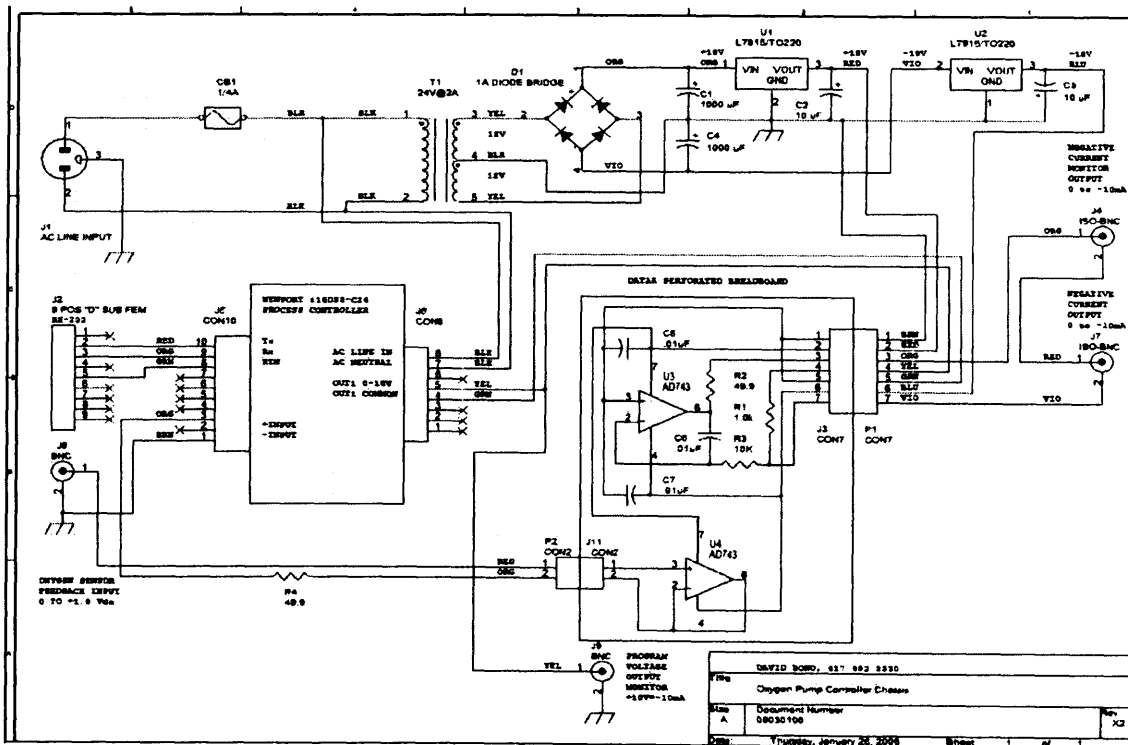


Figure 3-5 A schematic of the PID controller circuit.

3.2.4.4 Iso-Stoichiometric Electrical Conductivity

An important objective of this thesis was to systematically characterize the effect of oxygen stoichiometry on the properties of the low temperature semiconducting phase. Based on the defect model discussed in section 1.6, the level of non-stoichiometry, δ , determines the free carrier concentration. In this experiment, the degree of non-stoichiometry was controlled by controlling the ambient at high temperatures, which was then frozen-in at reduced temperatures. This enabled the characterization of the transport properties in the semiconducting phase as a function of non-stoichiometry.

The high temperature electrical conductivity and thermopower measurements described in section 3.2.4.1 and section 3.2.4.2 respectively, give information only about the effect of non-stoichiometry on the high temperature metallic phase. To examine the effects of non-stoichiometry on the low temperature semiconducting phase properties requires quenching of bulk samples. However, quenching ceramic samples can be catastrophic due cracking and failure from thermal shock. Due to the narrow PO_2 range over which VO_2 , it was not possible to freeze high temperature nonstoichiometry down to room temperature by cooling in a fixed PO_2 environment due phase changes. Evidence of this can be seen, for example, in Figure 4-3. Therefore an alternate method of freezing the non-stoichiometry is needed.

The approach, followed in this study, was to *freeze* in the high temperature stoichiometry by sealing the specimen in a leak tight vessel and utilizing the buffering action of the sample to maintain stoichiometry as the temperature is lowered.

If the sample is cooled, after being annealed, in a chamber whose oxygen content is fixed (i.e. sealed from the ambient) and much smaller than that in the sample, during cooling the sample will effectively not change its stoichiometry due the buffering action of the sample. When an oxide is cooled from high temperatures, it will attempt to oxidize. When the sample attempts to take in the oxygen from the region around it, the equilibrium oxygen partial pressure in the chamber will decrease. However, there is only a fixed amount of oxygen in the environment surrounding the sample. Therefore, the oxide sample will maintain an equilibrium oxygen partial pressure fixed by its oxygen content (stoichiometry). The initial high temperature stoichiometry can therefore be

maintained down to room temperature. Hence, the low temperature stoichiometry is iso-stoichiometric with the high temperature anneal condition. With this stoichiometry freezing method, samples can be slow cooled and the failure of samples is avoided. Furthermore, it makes it possible to measure the electrical properties as a function of temperature at a fixed oxygen stoichiometry.

The experimental setup for iso-stoichiometry measurements consists of a quartz tube with an electrical feed through and gas feeds. The bulk sample is mounted exactly as in the bulk conductivity measurements described in section 3.2.4.1. The cold end of the alumina rod is sealed with Varian Torr-Seal® (Varian part #9530001 [78]), a highly leak proof seal. The sample is annealed at elevated temperature at a selected oxygen partial pressure for 72 hr. After anneal, the gas inlet and outlet valves are closed, thus isolating the interior from the exterior ambient. Once properly sealed, the sample is slow cooled, with electrical conductivity measurements performed during cooling. A schematic of the iso-stoichiometry measurement setup is shown in Figure 3-6.

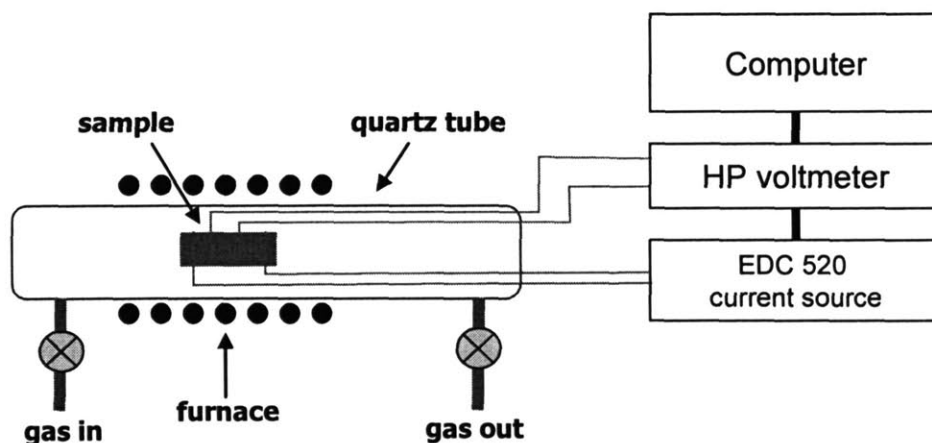


Figure 3-6 Schematic of the iso-stoichiometry anneal and measurement setup.

3.2.4.5 Thin Film Electrical Conductivity

The DC electrical conductivity of the VO_2 thin films was measured with the aid of micro-probes. A 4-point parallel electrode configuration was used, as described in section 3.2.2.2. The electrodes were 1.5 mm wide and the spacing between them was 3 mm. The

electrodes were deposited by DC sputtering from a platinum target. The thickness of the electrode was 100nm.

The DC conductivity was measured by applying a specified current across the outer electrodes and measuring the corresponding voltage drop across the inner electrodes. The current was stepped linearly in increments of 2 mA in both polarities, up to a maximum value of 10 mA. The voltages were plotted against the current values. The slope of the voltage-current plot gives the sample resistance at that particular temperature. The conductivity was then calculated using:

$$\sigma = \frac{l}{RA} \quad (29)$$

where the geometric constant, l , the length of the electrodes was 8 mm, A , the cross-sectional area is given by the product of the thickness of the film and spacing between the voltage measuring electrodes. This latter value was 3 mm. Film thicknesses ranged between 100 nm to 250 nm.

3.2.4.6 Coulometric Titration

Coulometric titration was used to measure the oxygen content in the VO₂ powder as a function of PO₂. The amount of oxygen in an oxide material can be very accurately measured by this technique. The oxide powder is sealed inside a zirconia crucible. Oxygen can then be pumped into or out of this sealed crucible electrochemically by applying a current/voltage between the inside surface of the crucible and outside surface. The total charge passing through the zirconia crucible can be converted into the total amount of oxygen pumped in or out. The number of moles of oxygen passing through the zirconia crucible is given 30.

$$n = \left(\frac{1}{4F} \int_{t_1}^{t_2} I dt \right) - \frac{V}{RT} (P_1 - P_2) \quad (30)$$

where n = no. of moles of oxygen pumped, F = Faraday constant (96,485 C/mol), I = applied current, t_1 = start time, t_2 = end time, V = “dead volume” (~ 4.5 cc), R = molar gas constant, T = temperature, P_1 = starting oxygen partial pressure, and P_2 = oxygen partial pressure at end of pump cycle.

The experimental arrangement was very similar to that described by Stefanik [67]. A schematic of the setup is shown in Figure 3-7. A small (~ 5 ccl) crucible was electroded with platinum ink (Engelhard #6082) on the inside and outside faces. The electrodes were sintered at 800°C for 1 hr. Several layers of platinum ink were applied to ensure good electrical contact with the zirconia crucible and to minimize contact resistance. A separate zirconia disc was similarly electroded. 0.1mg of V_2O_5 powder was weighed and placed inside an alumina crucible covered in platinum foil. The platinum foil served to prevent reaction of the VO_2 with the alumina crucible. The powder containing alumina crucible was place on top of the zirconia disc and covered with the zirconia crucible. The disc was then sealed to the crucible using a glass sealant (Elan #13 [17]). The glass powder was dispersed in water and applied to the joint. In order to ensure proper sealing, the entire setup was heated to a 1000°C, which is above the glass transition temperature of the sealant. Several layers of the sealant had to be applied to ensure good sealing. Because V_2O_5 melts at 670°C, the crucibles were heated in a 1000 ppm CO/balance CO_2 environment to prevent oxidation of the powder and subsequent melting.

The electrodes of the crucible and disc were contacted by platinum wire. These wires served as electrical leads. The electrodes of the crucible were used for pumping oxygen

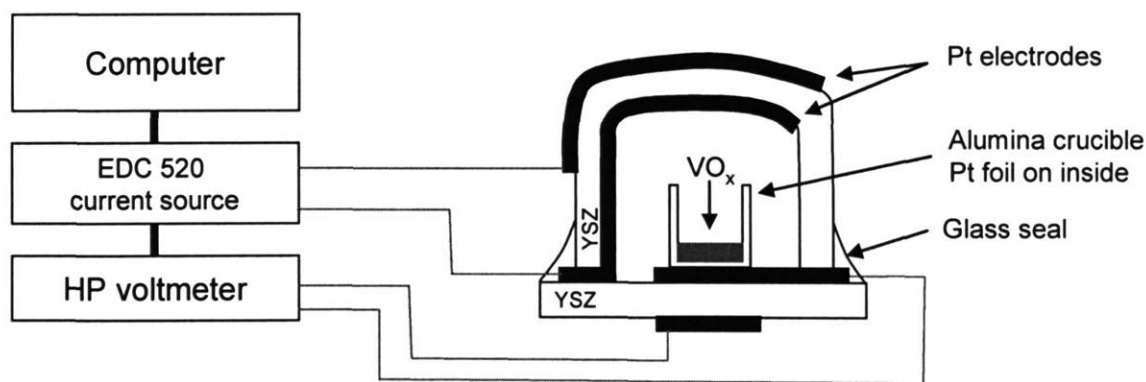


Figure 3-7 Schematic of the coulometric titration cell setup.

while the electrodes of the disc were used to measure the equilibrium voltage, and hence, the oxygen partial pressure inside the crucible.

The coulometric titration measurements were carried out in air between 450°C-650°C. The inner and outer electrodes were shorted for 6 hrs before each run and left to equilibrate for a further 6 hr. A controlled amount of oxygen was then pumped out of the crucible by applying a current for 30 min. The titration cell was left to equilibrate for 120 min. The equilibrium oxygen partial pressure inside the crucible was measured with the disc electrodes before the next pump cycle. This procedure was repeated until the oxygen partial pressure inside the crucible was approximately 10^{-14} atm. This corresponds to the oxygen boundary of the VO₂ phase field.

The total amount of oxygen pumped is then determined from the total amount of charge passed. The total charge is give by $I*t$. From the total charge, the amount of oxygen pumped can be calculated by after correcting for dead volume effects, using Eq. 30.

3.2.5 Optical Characterization – Transmission measurements

The effects of oxygen stoichiometry on the optical absorption were characterized using optical transmission measurements. VO₂ thin films were deposited on fused quartz substrates as described in section 3.2.2.1. The VO₂ samples were then annealed at different stoichiometries using the iso-stoichiometry setup as described in section 3.2.4.4.

The optical transmission measurements were carried out using a Perkin-Elmer spectrophotometer (model Lambda19). This instrument consists of a broadband light source which passes through a monochromator and photodetectors. The beam is then split into two. One passes through the sample being measured, and the other is used as a reference/control. When this measurement was carried out, a blank fused quartz substrate was placed in the reference beam-line. The intensity ratio between reference and sample being measured is recorded. This ratio is the fraction of light transmitted at a particular wavelength. The samples were tested between 250 nm and 2000 nm.

The absorption coefficient was calculated assuming exponential decay in intensity, given by:

$$I = I_0 \exp(-\alpha d) \quad (31)$$

where the ratio I/I_0 is the percentage light transmitted, α is the absorption coefficient, and d is the thickness of the absorbing layer, which was assumed to be primarily the VO_2 film.

3.3 Barium Titanate Electro-Optic Modulator

3.3.1 Thin film Growth

Thin films of barium titanate (BT) were grown using pulse laser deposition. A schematic of the PLD setup was shown earlier. The film properties, primarily the degree of crystallization, film orientation/epitaxy are highly dependent on the deposition conditions. Given the significant anisotropy of the electro-optic coefficient in BT, for optimum modulator performance, the BT films need to be grown (001) oriented thereby enabling the large r_{42} value to be utilized. The optimization of the growth parameters and the characterization of the film quality and orientation were carried out by Jussi Hiltunen.

The optimum deposition parameters used for growing epitaxial BT films is given in Table 6. The films were grown on (100) magnesium oxide substrates. The orientation of the BT film could be controlled by varying the total oxygen working pressure. The out of plane orientation of the film was varied between (100) and (001).

Table 6 shows the optimum deposition parameters that were used to grow epitaxial thin films of barium titanate.

Property	Value
Base Pressure	2×10^{-6} Torr
Total Working Pressure	1 mTorr to 15 mTorr
Deposition ambient	Pure oxygen gas
Substrate Temperature	700°C
Energy per pulse	500 mJ/pulse
Pulse rate	5 Hz

3.3.2 Thin Film Characterization

The orientation and phase of the deposited films were characterized by x-ray diffraction. A Rigaku 300 instrument with a rotating anode and 185 mm diffraction diameter was used. Theta-2 Theta measurements were performed using this tool to characterize the phase of the film. A Bruker D8 machine was used to characterize the epitaxy of the films by varying the tilt (ψ) and the rotation, ϕ angles.

3.3.3 Electro-Optic Modulator Design

A Mach-Zehnder configuration was used for the optical modulator. This is a standard modulator design for phase shift or intensity modulators. Two different waveguide structures were evaluated. One design was a BT-based ridge waveguide. The other was using a SiN strip loaded design.

The Optimum waveguide dimensions were calculated using FimmWave [19], a commercial mode solver, by Jussi Hiltunen.

3.3.4 Modulator Fabrication

To demonstrate electro-optic modulation in thin-film BT, waveguide devices were fabricated. A strip-loaded design was chosen for the primary demonstration of E-O modulation. This design involves the use of a patterned silicon nitride (“SiN”) waveguide (strip) with real index of refraction of 1.79 (and low absorption).

The strip waveguide design was preferred due to its ease of fabrication. An alternate design involving direct patterning of BT was also investigated. However, due to processing difficulties in obtaining smooth edge walls, this approach was abandoned. The dry etch chemistry used (Ar/Cl_2) re-deposited residue on the side walls, resulting in the non-uniform etch of edges (see SEM micrographs in results section).

A Plasmaquest PECVD deposition tool was used to deposit the SiN with a refractive index of 1.79 (at 1550 nm). A high resistivity SiN is preferred in order to maximize field penetration into the BT, thus, maximizing the electro-optic effect of the BT. The deposition recipe was adjusted to obtain different stoichiometries of SiN.

The SiN deposited on BT films was patterned with standard Shipley OCG 835 positive resist and etched with a CF₄, O₂, He, RIE chemistry. Minimum edge roughness and good critical dimension (CD) control is essential for transmission of light along the strip waveguides. From the SEM micrograph (Figure 4-31) of the etched waveguides, it can be seen that the etched waveguide quality is sufficient (edge roughness was less than 10 nm) for this application.

Two designs were fabricated. One design involved straight waveguides with waveguide widths between 1 μm and 10 μm and varying electrode spacings of 4-6 μm. Mach-Zhender structures were also fabricated with similar waveguide widths and electrode spacings together with arm opening angles between 1° and 4°.

Aluminum electrodes were sputter deposited and direct patterned with a wet chemical etchant: PAN etch. The PAN etch is a mixture of phosphoric acid, acetic acid and nitric acid.

The devices were then coated with resist and diced half thickness of the substrate and then cleaved for testing. A smooth waveguide edge is needed to reduce coupling losses during testing. The resist was dissolved away afterwards using acetone.

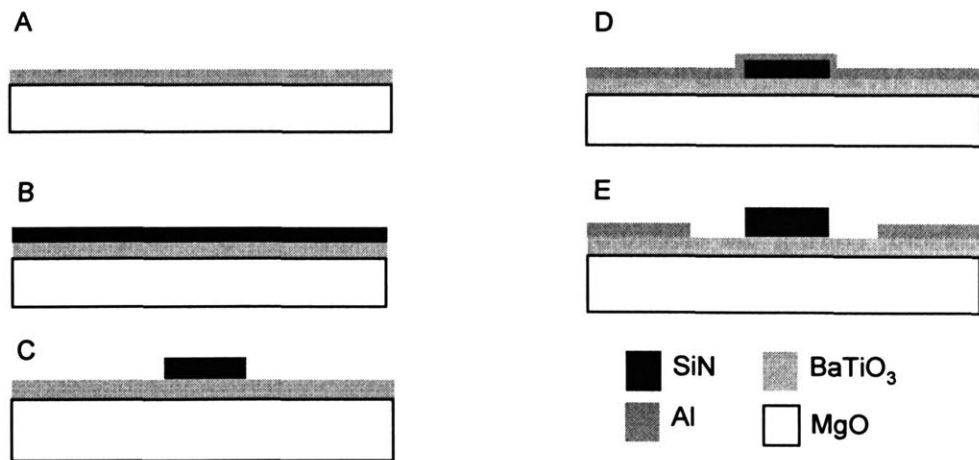


Figure 3-8 Schematic showing the processing steps for fabricating the E-O modulator devices. A) PLD growth of BT film. B) PECVD deposition of SiN waveguide layer. C) Pattern of SiN. D) Sputter deposition of aluminum. E) Pattern and wet etch of aluminum.

3.3.5 Modulator Testing

A Schematic for testing of the E-O modulators is shown in Figure 3-9. The testing was done in Prof. Lionel Kimerling's laboratory. The test setup includes a tunable laser source, polarization controller, a probe-station and micro-probes for contacting the metal electrodes, and CCD camera photodiode was measuring output light intensity.

The output of the laser source is coupled to an optical fiber which passes through a polarization controller. The fiber tip was then aligned with the waveguide on the sample being tested. At the output end, the light was coupled back onto an optical fiber which was then channeled to the photodetector.

A DC voltage source was used to apply the electric field between the metal electrodes on one of the arms of the modulator. The change in intensity at the output of the modulator was measured as function of applied voltage.

A fiber coupled laser operating at 1550 nm wavelength was used as a light source in the waveguide device measurements. The intensity was modulated with a chopper located between two free space optical fiber connectors. The measurement setup was also equipped with a fiber coupled polarization state controller. The correct polarization at the input fiber was confirmed with the external polarizator before the actual waveguide measurement. TE polarized light was end-fire coupled into the Mach-Zehnder waveguide modulator from the lensed input fiber. Proper waveguide operation was verified by imaging the modulator output intensity distribution with a microscope objective coupled infrared camera. During the electro-optic measurements, a voltage sweep was applied across the electrodes and the microscope objective collected light was directed to the optical power meter instead of the camera. The intensity was read from the phase lock amplifier that was frequency matched with the chopper.

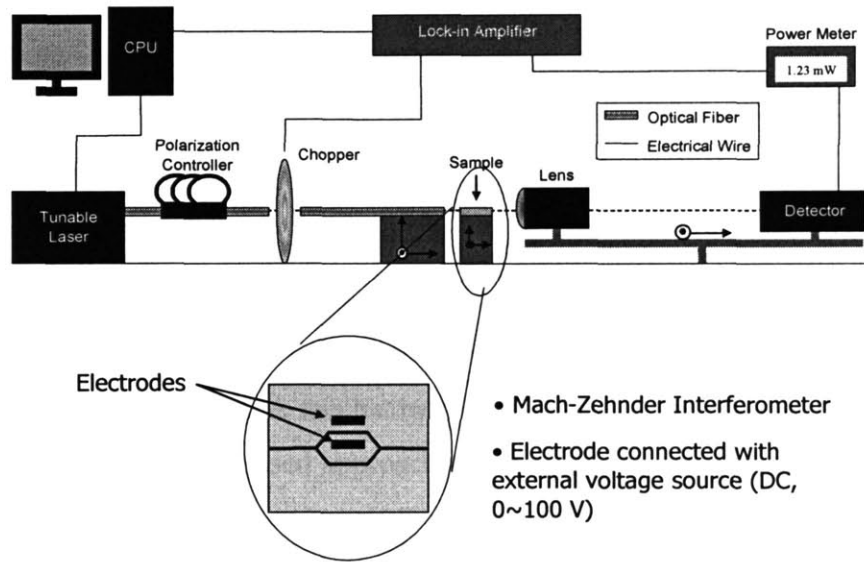


Figure 3-9 Schematic of the E-O modulator test setup.

Chapter 4: Results

In this chapter the results of the work on the three main topics covered in this thesis will be presented. This includes MEMS-based optical switching of ring resonators, electrical, optical and non-stoichiometry characteristics of VO₂ and barium titanate based electro-optic modulators.

Ring resonators were discussed earlier to be highly attractive wavelength selective filters capable of large scale integration for optical add-drop multiplexers. The ring resonator design is an always “on” switch. A mechanism to switch “off” the resonator was desired. To address this need a MEMS based approach was chosen. The results of fabricating the MEMS devices, the optical resonator switch response and the results of development of TiN for MEMS devices will be discussed further in section 4.1.

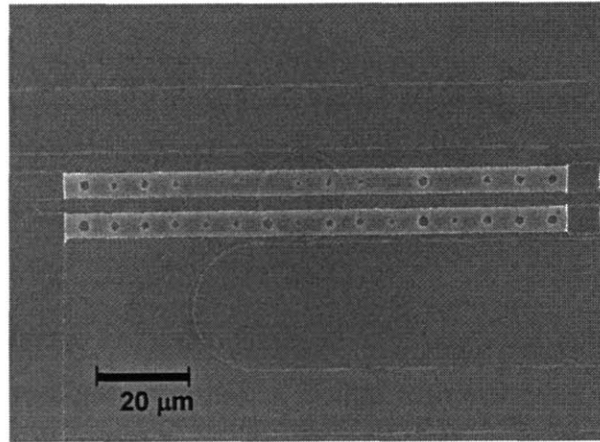
In section 4.2 the results from the characterization of the electrical and optical properties of VO₂ under various oxygen partial pressures and temperatures and their effects on the low temperature semiconducting phase will be displayed.

Section 0 covers the results of the design and fabrication of barium titanate based electro-optic modulators.

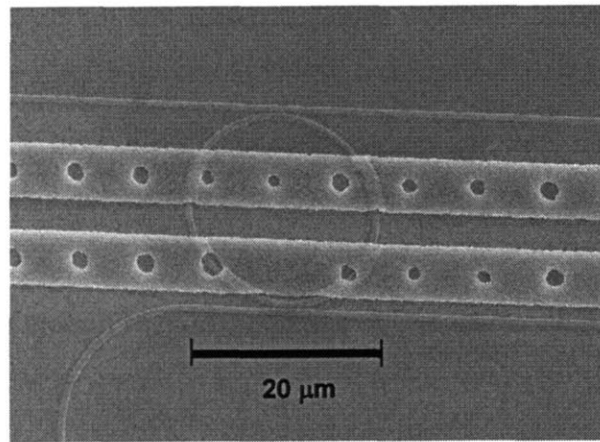
4.1 MEMS-switch Results

4.1.1 Fabrication Results

Optical and scanning electron microscopy were used to visualize the fabricated MEMS devices. A SEM micrograph of a typical MEMS switch and a close-up of the device near the ring-resonator are shown in Figure 4-1.



A)



B)

Figure 4-1 SEM micrographs of a typical MEMS ring-resonator switch. A) Top view of entire MEMS device on top of a ring resonator with anchors on either side of the beams and contact pad on the left. B) Close-up of the MEMS structures near the ring resonator.

From the top view of the devices, it can be seen that the beams were not perfectly aligned with the ring resonator. This was due to misalignment of the alignment marks of the aluminum mask and the nitride waveguide layer during the contact lithography alignment process step. One of the key optical requirements in the ring resonator design was that the lossy/absorbing layer be at least $1\ \mu\text{m}$ away from the throughput and drop waveguides. The misalignment of the MEMS beams could contribute to optical loss in these waveguides.

4.1.2 MEMS Optical Test Results

The spectral response, i.e. the variation in intensity as a function of wavelength in the drop and throughput ports, with and without applied voltage on the MEMS bridge was measured. The relative transmission was calculated and is plotted in Figure 4-2.

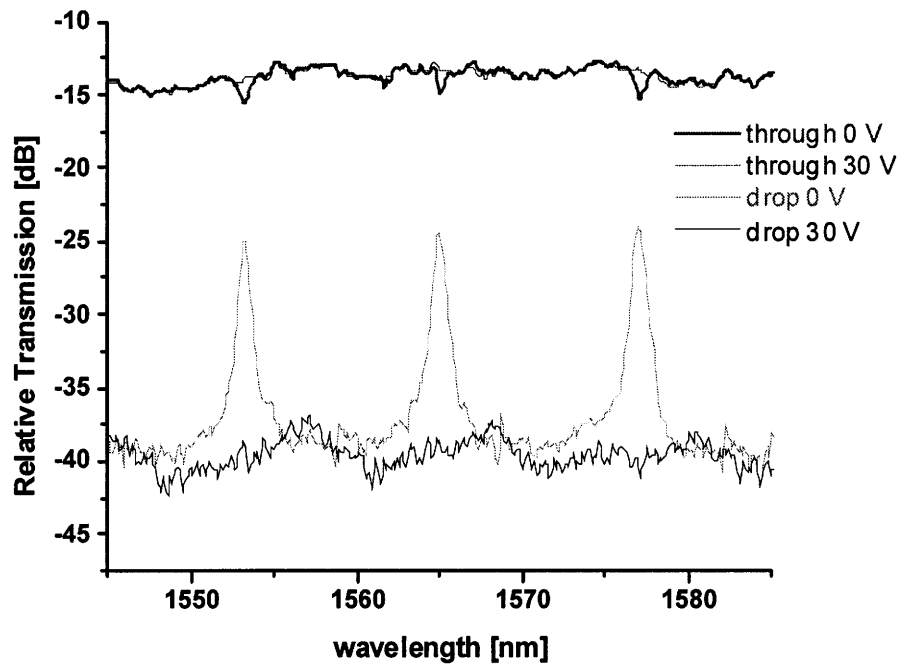


Figure 4-2 Relative transmission in the throughput and drop ports of the optical ring resonator with and without applied voltage to the MEMS structure. The relative transmission was measured as a function of wavelength.

With no voltage applied, the beam remains displaced from the ring resonator, and the switch is in its “on” state, such that the wavelength that is in resonance with the ring resonator is coupled to the drop port. This can be seen in Figure 4-2. For example, consider the switch response at the 1565nm resonance wavelength. At this wavelength, with no voltage applied, optical power in the throughput port is transferred to the drop port, evidenced by the minimum in the throughput port transmissivity and the peak in the

drop port transmissivity at this wavelength. The peaks and troughs at 1553nm and 1576nm correspond to resonances of higher and lower order respectively.

An essential requirement of the optical switch is the switching speed. To measure the switching speed, the temporal response of the ring resonator switch was measured at a fixed wavelength. The wavelength corresponded to one of the resonance wavelengths of the ring resonator. For the temporal response measurements, a square wave cyclic voltage was applied at 8 kHz drive frequency. The relative transmissivity in the throughput port was measured as a function of time and the results are shown in Figure 4-3.

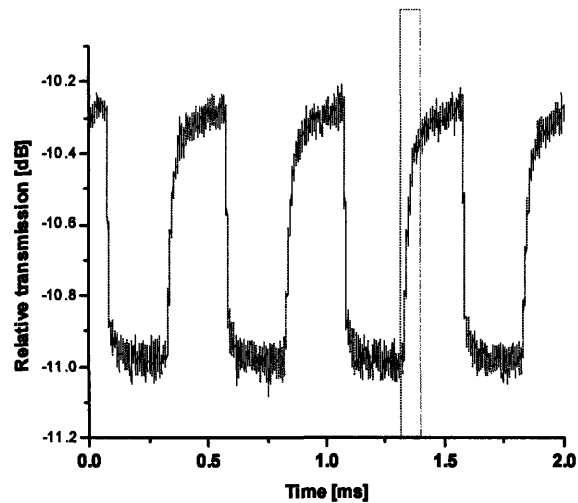


Figure 4-3 Temporal response of the ring resonator. The relative transmission in the throughput port is shown.

By examining Figure 4-3, it can be seen that the switching contrast in the throughput port was approximately 0.7 dB. The switch time, determined by the rise time of the relative transmission from 10% to 90% of the full range, was approximately 60 μ s for switching the resonator “off”. The switch “on” time was approximately 10 μ s.

4.1.3 TiN based mechanical beams

The optical switch devices fabricated with aluminum were observed to have significant plastic deformation due to residual stresses. TiN was examined as a potential alternative.

TiN has a superior stiffness to density ratio (compared to aluminum and silicon - see Appendix A for material properties), has non-stick surface properties and potentially large failure strength given its high hardness value (as high as 24 GPa [56]).

TiN was deposited by reactive sputtering of a titanium target. TiN was deposited on silicon substrates and on silicon-silicon dioxide-poly-silicon substrates.

Beams fabricated out of TiN were found to be significantly buckled after release, i.e. following removal of the sacrificial poly-silicon layer by XeF_2 . The deflection of beams due to buckling was characterized by white light optical interferometry using a Zygo optical microscope. This buckling was due to residual stresses originating from the sputter deposition of TiN. The vertical deflection of a beam along its length was measured using the Zygo interferometer and the results are shown in Figure 4-4.

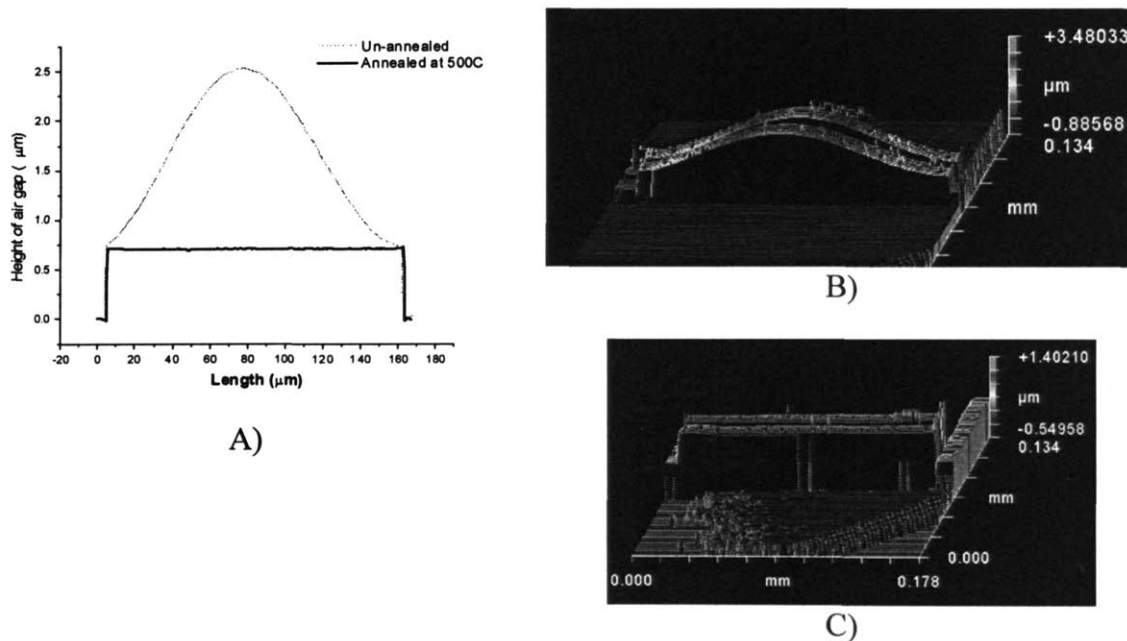


Figure 4-4 Results of residual-stress induced buckling in post-released fixed-fixed beams. A) Beam deflection data pre- and post- anneal. B) Zygo deflection contour plot of a typical MEMS beam pre-anneal and post-released. C) Contour plot showing beam deflection after anneal and release.

It can be seen from Figure 4-4B that the deflection at the center point of the beam was approximately 2.5 μm .

The residual stresses in TiN were controlled by annealing at high temperatures in a nitrogen environment. The average stress in the thin film is shown as a function of temperature in Figure 4-5.

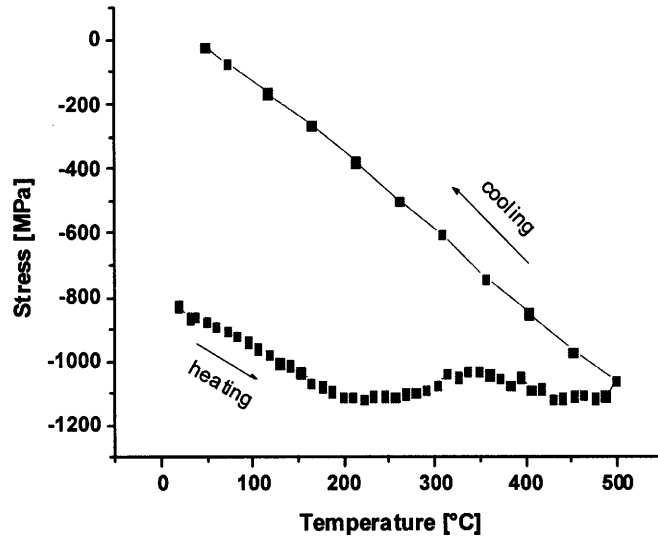


Figure 4-5 Stress evolution in TiN during annealing of as-deposited thin film on bare silicon wafer substrate.

In Figure 4-5, it can be seen that the as-deposited film stress was approximately -800 MPa. Heating the film lead to an increase in the compressive stress up to 200°C which was approximately maintained up to 500°C. Upon cooling, the stress decreased linearly reaching a final room temperature stress level of approximately +50MPa.

The stress measurement was repeated on a film stack mimicking the actual device fabrication. The thin film stack was comprised of silicon dioxide and poly-silicon on a silicon substrate. The evolution of the stress during the anneal process is shown in Figure 4-6.

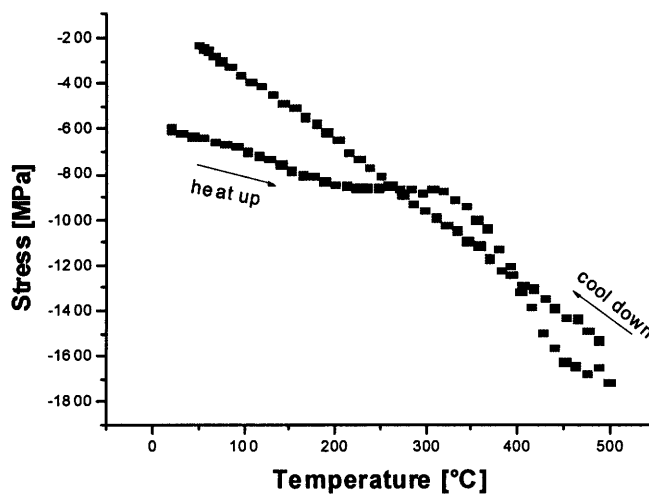


Figure 4-6 Stress evolution during annealing of TiN sputter deposited thin film on silicon (substrate)-silicon dioxide-poly-silicon stack.

Comparison of Figure 4-5 and Figure 4-6 shows differences in the room temperature stress levels of TiN deposited on bare silicon wafer (Figure 4-5) and on silicon-silicon dioxide-poly-silicon stack (Figure 4-6). The starting and final stress levels, as well as the stress level at the highest anneal temperature, 500°C, are significantly different. These differences were due to the differences in the composition of the underlying layers. The stress measurement shown in Figure 4-5 was carried out on TiN films deposited on a bare silicon substrate. The results shown in Figure 4-6 were carried out on TiN thin film deposited on poly-silicon which was deposited on low-temperature chemical vapor deposited silicon oxide grown on bare silicon substrate. This latter structure was more representative of the actual device fabrication situation. Thus characterizing the stress of the TiN on composite silicon oxide and poly-silicon thin films is crucial.

X-ray diffraction was used to characterize the phase and crystallinity of the as-deposited and post-annealed TiN films. A typical x-ray spectrum is shown in Figure 4-7.

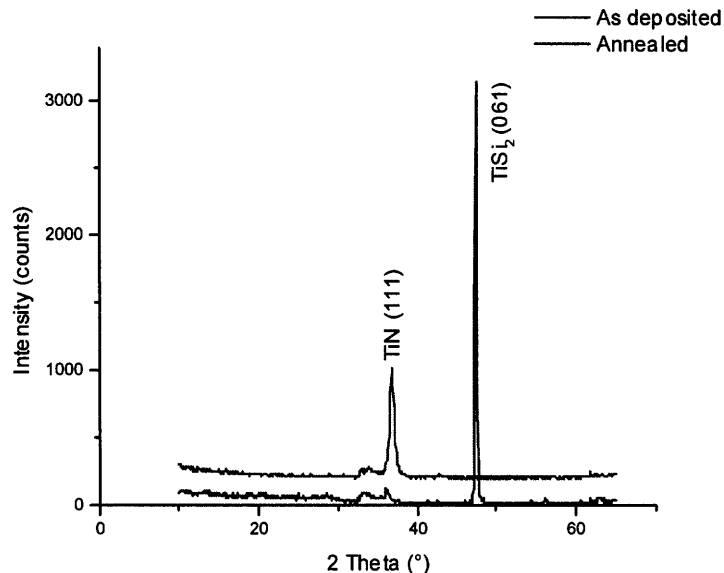


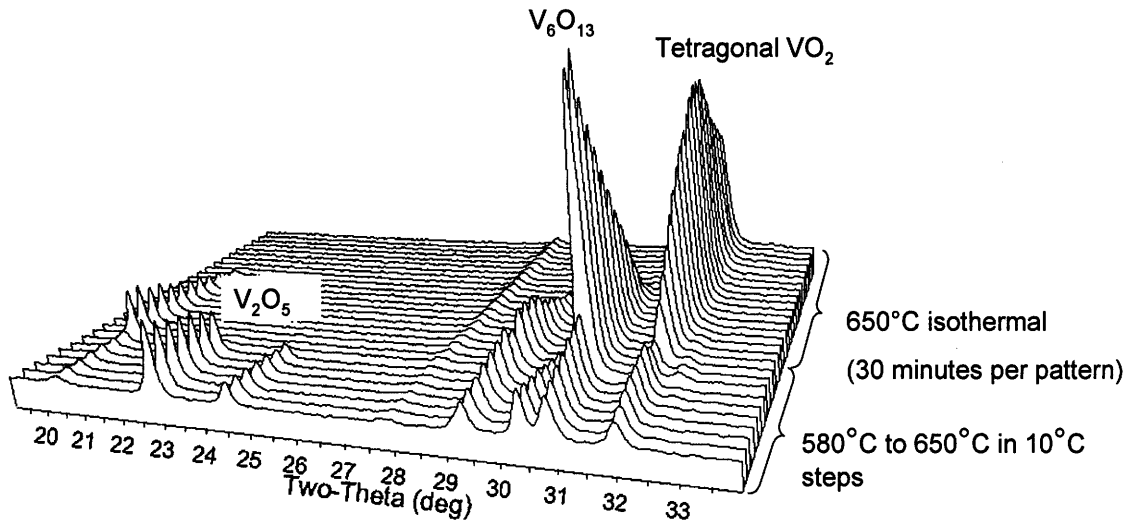
Figure 4-7 Theta-2Theta x-ray spectrum of as-deposited and post annealed TiN thin film.

From the x-ray spectrum it can be seen that the as-deposited TiN has reacted to form TiSi₂. The diffraction peak at approximately 38° 2-theta in the as-deposited film indicates crystalline TiN. However, this peak was barely observed in the post-annealed x-ray spectrum. In the post-annealed film, a new peak appeared at approximately 48° 2-theta. This new peak was representative of TiSi₂.

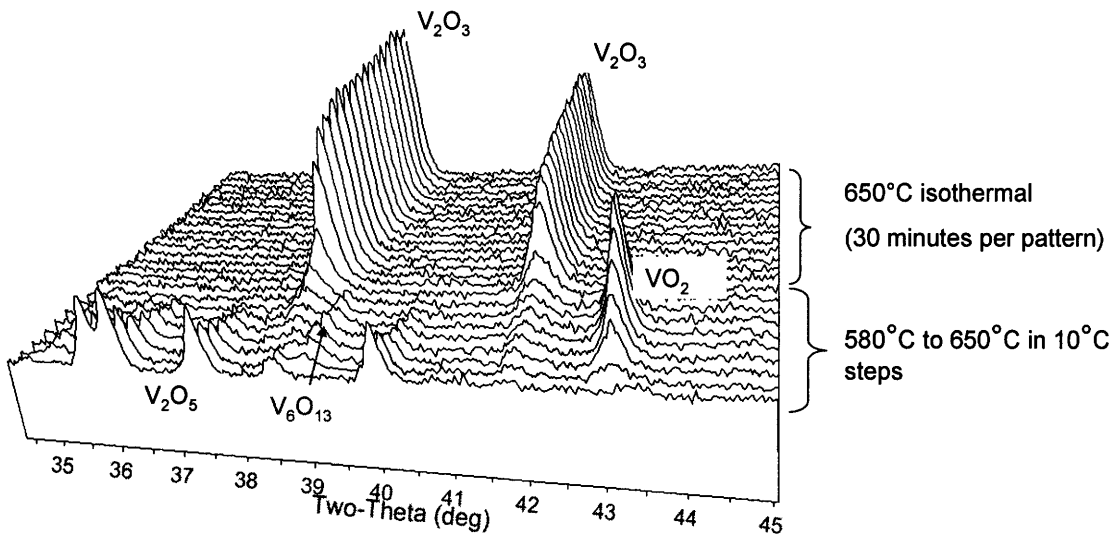
4.2 Vanadium (IV) Oxide

4.2.1 High Temperature X-ray Diffraction

In-situ x-ray diffraction studies were carried out on powder samples at 650°C between oxygen partial pressures of 10⁻¹¹ and 10⁻¹⁸ atms. This measurement was performed by Scott Mixture at Alfred University. The results shown in Figure 4-8 show the transformation of V₂O₅ powders to V₆O₁₃, VO₂ and V₂O₃.



A)



B)

Figure 4-8 High temperature in-situ x-ray diffraction spectrum taken between 580°C and 650°C in A) 100ppm CO/CO₂ gas mixture and B) 700ppm CO/CO₂ gas mixture.

When V₂O₅ powder was heated in a 100 ppm CO/CO₂ mixture, the V₂O₅ phase was found to transform to V₆O₁₃ followed by transformation to VO₂ after being held at 650°C for 390 min. In a repeat of the measurement in a 700 ppm CO/CO₂ mixture, the VO₂ transformed to V₂O₃. From the high temperature in-situ x-ray diffraction studies, it can be

concluded that the phase transformation from VO_2 to V_2O_3 occurred between 1.3×10^{-15} atm and 2.7×10^{-17} atm.

4.2.2 Thin Film X-ray Diffraction

X-ray diffraction was used to identify the phase of the PLD deposited thin films. A typical x-ray diffraction spectrum of the VO_2 thin films is shown in Figure 4-9. The films were deposited on fused quartz substrates heated to 600°C . The specific deposition conditions were listed in the experimental section.

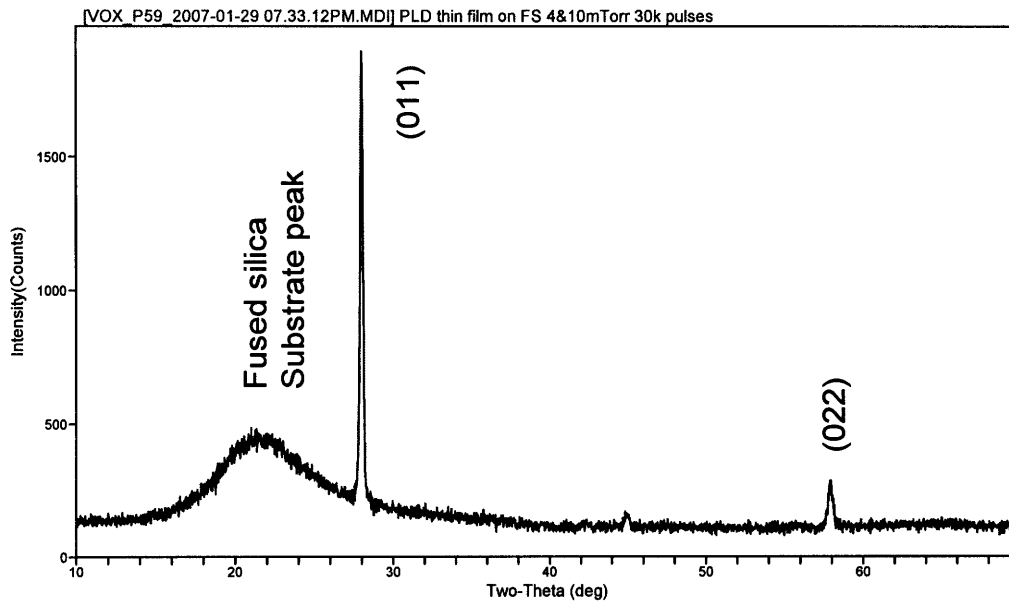


Figure 4-9 A typical x-ray diffraction spectrum for a VO_2 thin film deposited on a fused quartz substrate.

4.2.3 DC Electrical Conductivity – Bulk Samples

DC electrical conductivity measurements were performed on bulk, polycrystalline samples of VO_2 between 1050°C and 850°C . These measurements were performed as a function of oxygen partial pressure. Results of these measurements are shown in Figure 4-10.

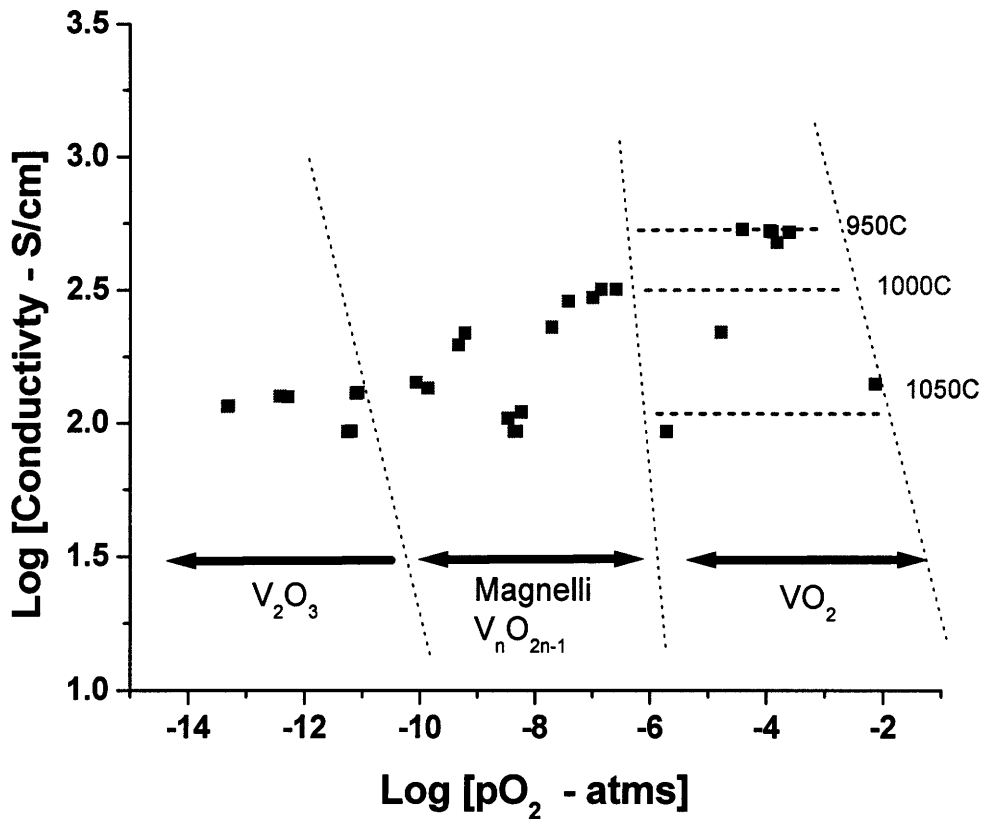


Figure 4-10 DC electrical conductivity of VO_x as a function of PO_2 for a series of temperatures.

In this plot, the boundaries of the stability ranges of the different VO_x phases are indicated. An increase in conductivity can be observed as one goes from V_2O_3 to VO_2 at the 1000°C isotherm. The conductivity is observed to be relatively independent of PO_2 in the VO_2 regime

4.2.4 Thermoelectric Power – Bulk Samples

The thermoelectric power of bulk, polycrystalline samples was measured as a function of oxygen partial pressure. These measurements were carried out together with the DC electrical conductivity measurements described above. The temperature range of measurement was 850°C to 1050°C . The thermoelectric power results are shown in Figure 4-11. One notes that the TEP coefficient decreases with increasing PO_2 . This trend was observed for both temperatures at which the TEP coefficient was measured. One also

notes the low magnitudes of the TEP ($\sim 10\text{-}35 \mu\text{V/K}$), consistent with the high electrical conductivities ($\sim 300 \text{ S/cm}$) measured under these circumstances.

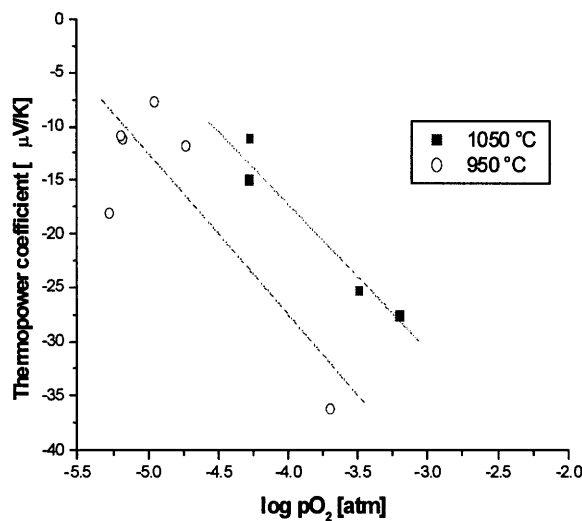


Figure 4-11 Thermoelectric power as a function of oxygen partial pressure for bulk VO₂ samples measured at elevated temperatures.

4.2.5 Low Temperature Iso-stoichiometric electrical conductivity measurements– Bulk VO₂

Iso-stoichiometric measurements were carried out by freezing-in the high temperature stoichiometry using the iso-stoichiometry measurement setup described in section 3.2.4.4. This experiment permits the measurement of the low temperature semiconducting phase transport properties as a function of the stoichiometry established under high temperature oxygen partial pressure anneal conditions. The bulk samples were annealed at 1000°C between oxygen partial pressures of 10^{-6} atm and 10^{-2} atm. Results of these measurements are shown in Figure 4-12. Iso-stoichiometry temperature dependent conductivity measurement over an extended temperature range above the phase transformation temperature for a sample annealed at 1000°C in a 1000 ppm O₂ ambient is shown in Figure 4-13. From this figure it can be seen that $\log \sigma$ goes through a maximum at approximately 1.5×10^{-3} reciprocal Kelvin which corresponds to approximately 600°C.

Thermoelectric power (TEP) measurements were made over the same temperature range (see Figure 4-14). The TEP coefficient varied between $-3 \mu\text{V/K}$ and $-6 \mu\text{V/K}$. The sign of the TEP coefficient was negative, indicating electronic carriers. The TEP values measured for this metallic-like higher temperature phase are consistent with values observed for other metallic oxides such as $(\text{La}_{1-x}\text{Sr}_x)_2\text{CuO}_{4-y}$. [13]. It can be noted that the TEP coefficient has a very weak temperature dependence, decreasing with increasing temperature.

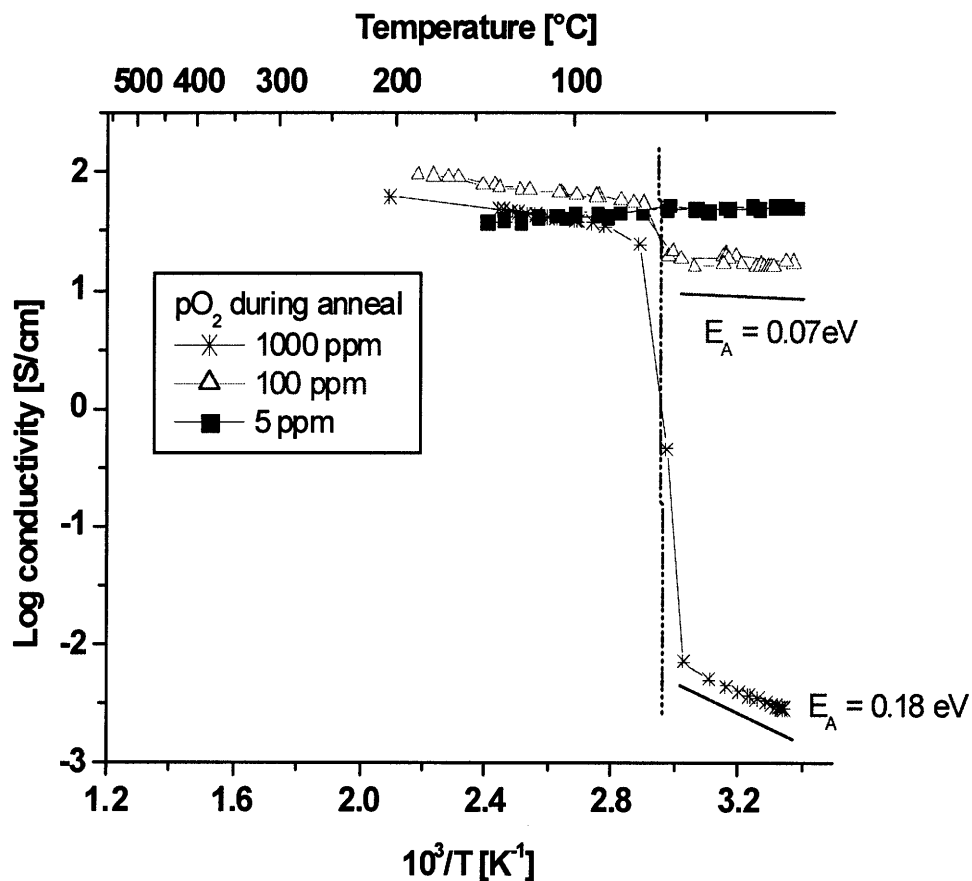


Figure 4-12 Electrical conductivity vs reciprocal temperature of bulk VO_2 samples with *frozen-in* stoichiometry.

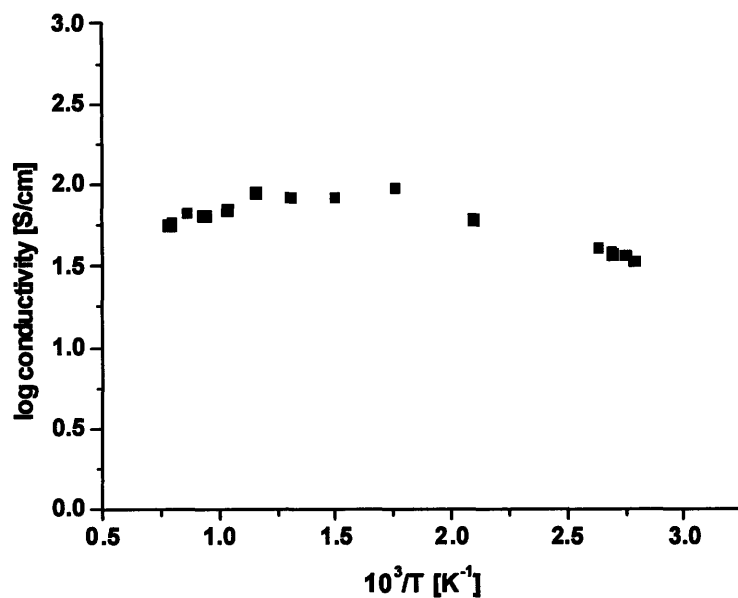


Figure 4-13 Temperature dependent electrical conductivity of a bulk VO₂ sample above the phase transition with *frozen-in* stoichiometry annealed in a 1000ppm O₂ ambient.

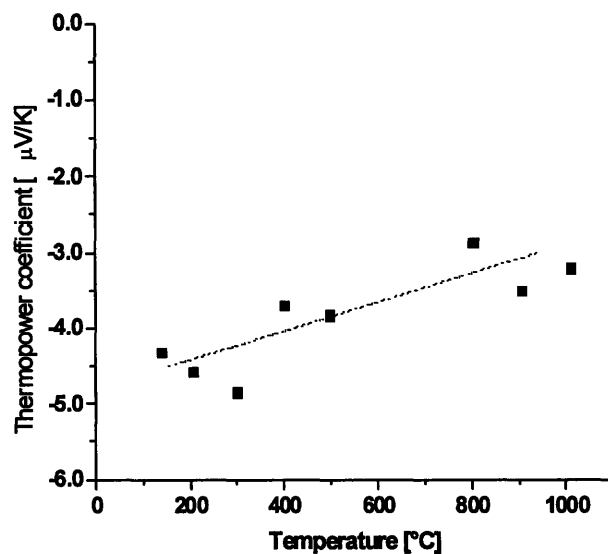


Figure 4-14 Temperature dependent of the TEP coefficient in a bulk VO₂ sample above the phase transition with *frozen-in* stoichiometry annealed in a 1000ppm O₂ ambient.

4.2.6 Low Temperature Thermoelectric power – Bulk

Thermoelectric power measurements were carried out on the bulk samples with *frozen-in* stoichiometry. Thermoelectric power gives a measure of the carrier type and density in the material. A negative thermoelectric power coefficient indicates predominant n-type carriers and a positive value indicates predominant p-type carriers. The thermoelectric power measurements were carried out between 25°C and 120°C in air. These results are shown in Figure 4-15.

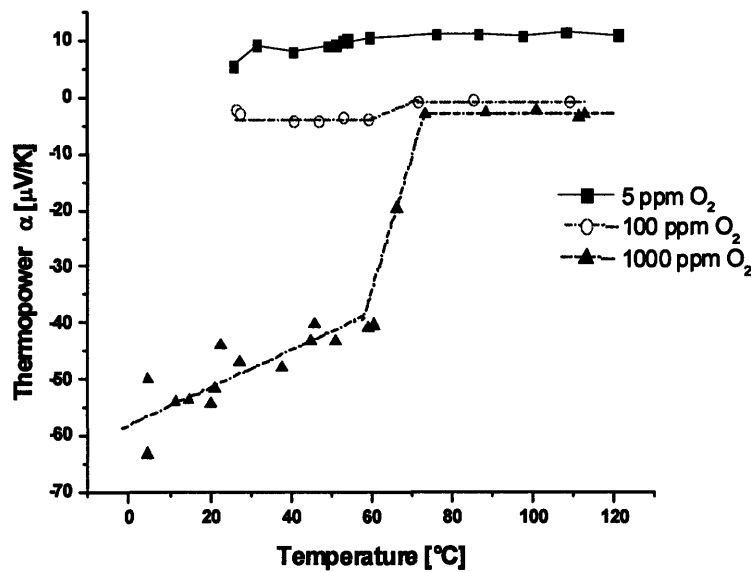


Figure 4-15 Thermoelectric power measurements on bulk samples with *frozen-in* stoichiometry. The oxygen partial pressures in the box on the right indicate the value used during the high temperature anneal.

The thermal activation of the thermopower indicates that the carrier concentration is thermally activated. This activation energy was calculated to be approximately $0.02 \text{ eV} \pm 0.001 \text{ eV}$ for the 1000 ppm sampled. Compared to the conductivity activation energy, $0.16 \text{ eV} \pm 0.001 \text{ eV}$ for the same sample, it can be clearly seen that there is a small temperature dependent activation of electrons and a stronger temperature dependence of the mobility. This thermally activated mobility indicates either a small polaron hopping behavior or a trapped mobility behavior.

If this sample is modeled as exhibiting small polaron behavior, the carrier concentration can then be calculated from the thermopower assuming the density of states in the conduction band is equal to the vanadium cation density. Assuming a cation density of $\sim 10^{22} /\text{cm}^3$, the calculated room temperature carrier concentration is 5.64×10^{21} carriers/ cm^3 . The mobility can then be calculated using this carrier concentration and equation 19. The calculated mobility is $4.7 \times 10^{-5} \text{ cm}^2/\text{Vs}$. This is a rather low mobility value, but is consistent with typical mobilities observed for other materials exhibiting small polar behavior [66].

This behavior can also be modeled like conventional semiconductor behavior, like silicon. The carrier concentration in this case can be calculated assuming an effective mass of $3 \cdot m_e$ giving an effective density of states of in the conduction band of $1.3 \times 10^{19} /\text{cm}^3$. The carrier concentration and mobility thus calculated were: 7.33×10^{19} carriers/ cm^3 and $3.66 \times 10^{-2} \text{ cm}^2/\text{Vs}$ respectively. Therefore, it can be seen that assuming even the most extreme conditions, the low mobility calculated demonstrates an activated mobility mechanism.

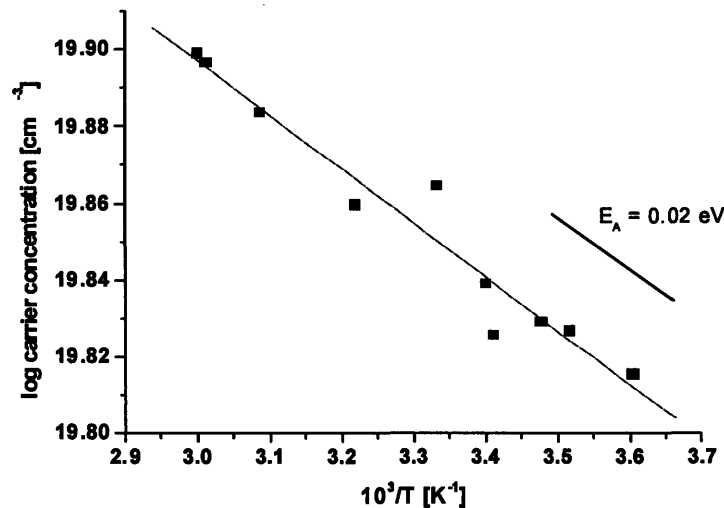


Figure 4-16 Log of carrier concentration vs reciprocal temperature in the semiconducting phase of VO₂ for a sample annealed at 1000 ppm O₂ and *frozen-in* stoichiometry assuming an effective mass of $3 \cdot m_0$.

4.2.7 Low temperature conductivity and TEP – thin films

The electrical conductivity of thin films deposited by pulse laser deposition was characterized between 25°C and 120°C. The effect of deposition oxygen working pressure on the conductivity was characterized and is shown in Figure 4-17. One observes that both the high and low temperature conductivities are affected by the oxygen working pressure. Samples deposited at relatively lower oxygen pressures (1 and 4 mTorr) had an order of magnitude higher conductivity in the metallic and semiconducting phases compared to samples deposited at relatively higher oxygen pressure (10 and 12 mTorr).

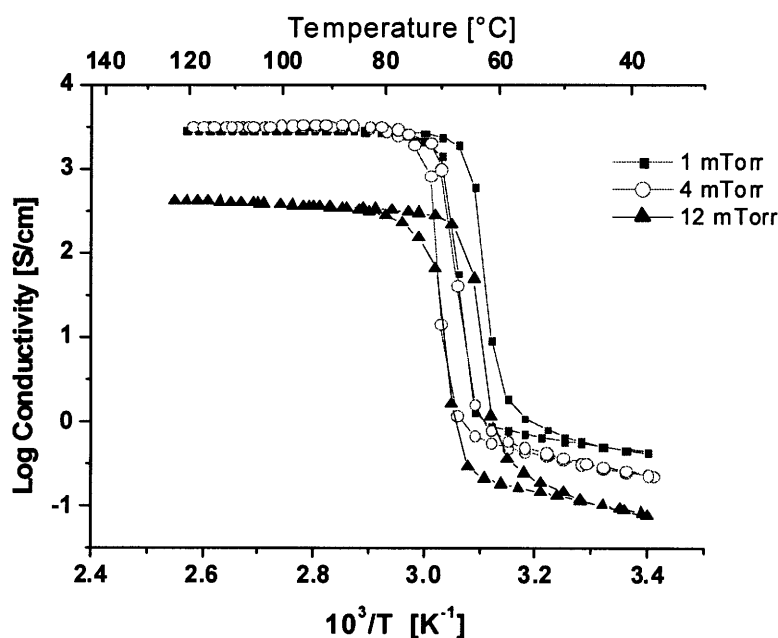


Figure 4-17 DC electrical conductivity of thin films of VO₂ deposited at different oxygen working pressures during pulse laser deposition.

4.2.8 Coulometric Titration

Coulometric titration measurements were used to characterize the stoichiometry of VO₂. This is done by measuring the number of moles of oxygen pumped electrochemically through a zirconia crucible as described in the section 3.2.4.6. These measurements were carried out on powder samples between 500°C and 650°C. A plot of the number of moles

of oxygen pumped versus the equilibrium oxygen partial pressure in the titration cell is shown in Figure 4-18.

In this figure, plateau areas where the equilibrium oxygen partial pressure shows no significant change with number of moles of oxygen pumped indicates two phase regimes. Regions where there are steep changes are indicative of non-stoichiometry in a single phase regime. The oxygen partial pressure range over which VO_2 is stable was shown in Figure 1-5 in the introduction chapter. Based on that stability data, the existence range of VO_2 is indicated in Figure 4-18 with horizontal lines for each temperature curve.

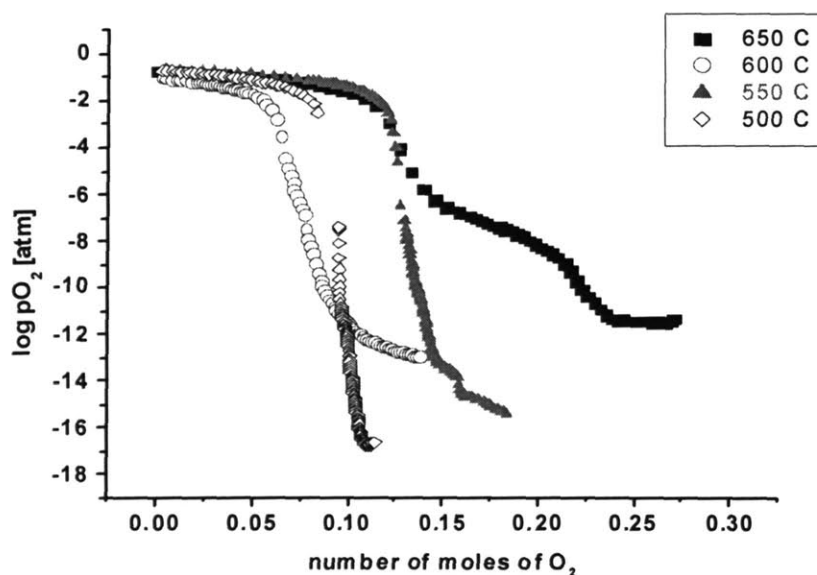


Figure 4-18 Raw data from coulometric titration measurements between 500C and 650C. The plot shows the equilibrium oxygen partial pressure as a function of amount of oxygen pumped out of the titration cell.

Based on the existence range of VO_2 the raw data in Figure 4-18 the amount of oxygen pumped out within the VO_2 phase and the associated equilibrium oxygen partial pressure is shown in Figure 4-19.

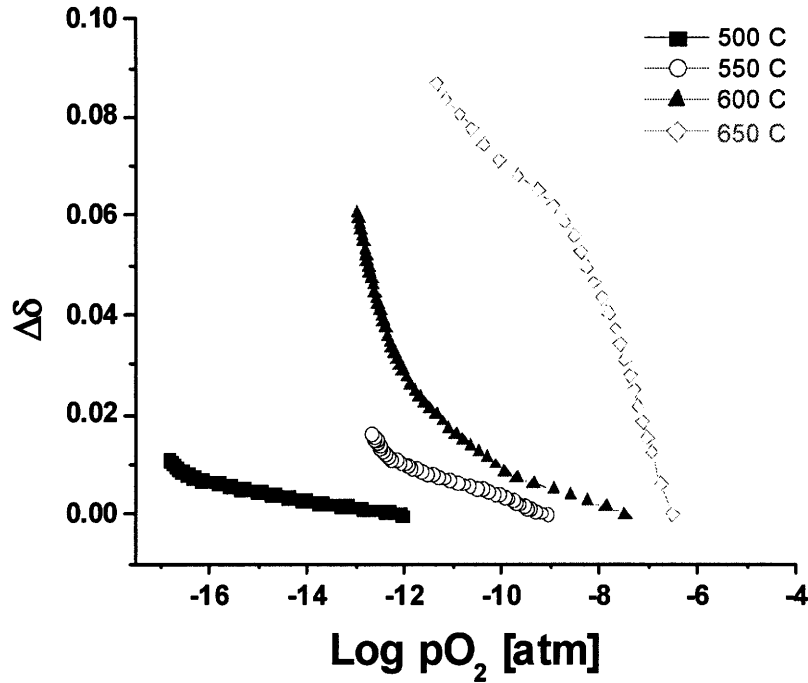


Figure 4-19 The equilibrium oxygen partial pressure as a function of total non-stoichiometry in VO₂.

The absolute non-stoichiometry, δ , in VO_{2- δ} can be extracted from Figure 4-19. The information obtained thus far from coulometric titration has provided only the overall non-stoichiometry in VO₂. That is, if VO₂ exists between VO_{2- δ (1)} and VO_{2- δ (2)}, then the information that has been obtained thus far is $|\delta(1)| + |\delta(2)|$ which will be referred to as $\Delta\delta$.

If it is assumed that oxygen nonstoichiometry, δ , is defined as the oxygen deficiency with respect to the stoichiometric composition, $\delta = 0$, then a change in nonstoichiometry, $\Delta\delta$, is related to the oxygen content in the sample as:

$$\Delta\delta = \delta - \delta^* \quad (32)$$

where δ^* is the oxygen deficiency at the start of the titration. If as was discussed earlier, the primary ionic defect in VO₂ is assumed to be $[V_i^{4+}]$ in the reducing regime and $[V_V^{4-}]$ in the oxidizing regime, that is assuming Frenkel defect formation, then:

$$\frac{N_A}{V_m} \delta = [V_i^{4+}] - [V_V^{4-}] \quad (33)$$

where N_A is the avogadro's number and V_m is the molar volume of VO_2 (19.9g/cm^3).

Therefore, substituting for $[V_i^{4+}]$ and $[V_V^{4-}]$ from equations 2 and 6 gives:

$$\frac{N_A}{V_m} \delta = [V_i^{4+}] - [V_V^{4-}] = \frac{1}{4}(4K_R)^{1/5}(PO_2)^{-1/5} - \frac{K_F}{(4K_R)^{1/5}}(PO_2)^{+1/5} \quad (34)$$

Thus, the measured change in stoichiometry, $\Delta\delta$, is related to the absolute stoichiometry by:

$$\Delta\delta = \delta - \delta^* = \frac{N_A}{V_m} \left[\frac{1}{4}(4K_R)^{1/5}(PO_2)^{-1/5} - \frac{K_F}{(4K_R)^{1/5}}(PO_2)^{+1/5} \right] - \delta^* \quad (35)$$

An equation of the form:

$$y = P(1) * x^{1/5} - P(2) * x^{+1/5} - P(3) \quad (36)$$

was used to fit the $\Delta\delta$ vs PO_2 data, where P(1), P(2), and P(3) were three independent fitting parameters. From these three fitting parameters, K_R , K_F , K_E and δ^* were calculated from:

$$\begin{aligned} K_R &= \frac{(4 * P(1))^5}{4} \\ K_F &= \frac{P(2) * (4 * K_R)^{1/5}}{4} \\ K_E &= \frac{(K_R)^{1/2}}{(PO_2^*)^{1/2} (K_F)^{1/4}} \\ \delta^* &= P(3) \end{aligned} \quad (37)$$

where PO_2^* corresponds to the partial pressure where $\delta = 0$. Equation 36 was used to fit $\Delta\delta$ vs PO_2 data for VO_2 . The absolute stoichiometry as function of PO_2 in VO_2 determined based on the fitting parameters is shown in Figure 4-20.

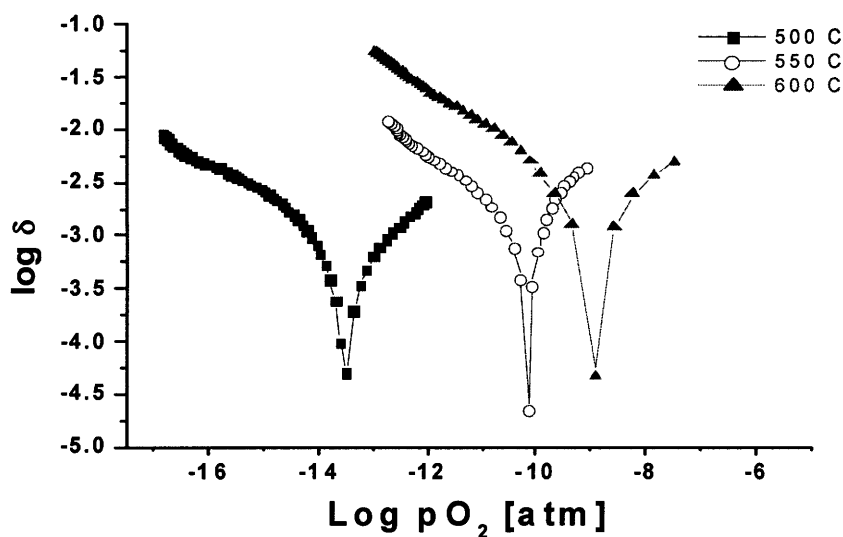


Figure 4-20 Dependence of absolute stoichiometry, δ , in $\text{VO}_{2-\delta}$ as a function of oxygen partial pressure.

From the fitting parameter obtained, K_F , K_R , and K_E were calculated by equation 37. These values were plotted as a function of inverse temperature and the results are shown in Figure 4-21, Figure 4-22, and Figure 4-23

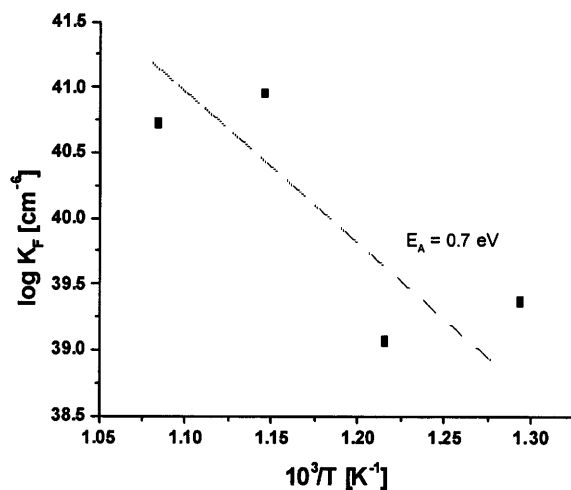


Figure 4-21 Temperature dependence of $\log[K_F]$ determined from fitting the titration data.

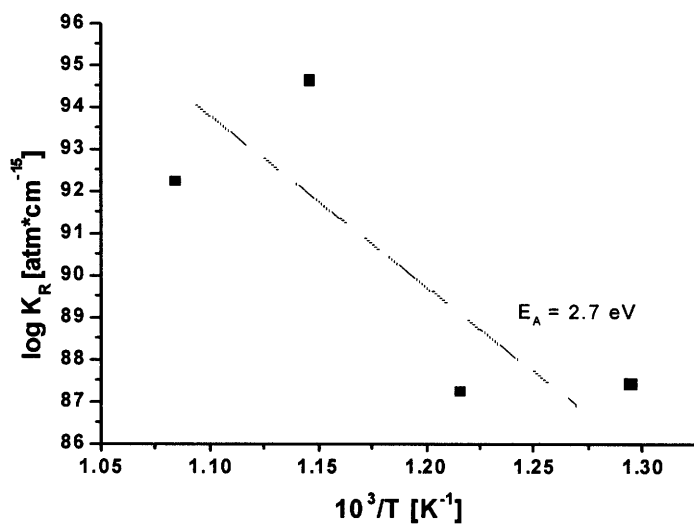


Figure 4-22 Temperature dependence of $\log[K_R]$ determined from fitting the titration data.

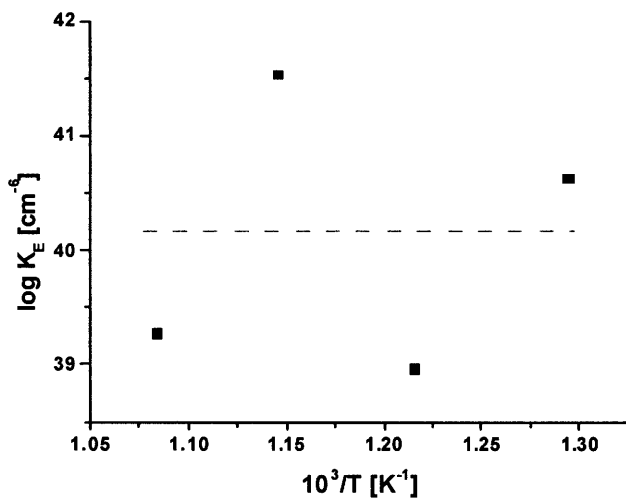


Figure 4-23 Temperature dependence of $\log[K_E]$ determined from fitting the titration data.

The activation energy of K_F was determined to be 0.7eV and K_R was determined to be 2.7eV. K_E was found, within experimental error, to be temperature independent.

4.2.9 Optical Properties

The optical absorption of PLD deposited thin films of VO₂ was measured with the wavelength dependence of the optical transmission both above and below the phase transition. The optical transmission plot is shown in Figure 4-24. The substrate used was fused quartz, which was confirmed to be nearly fully transparent within the wavelength range of interest. In the lower temperature semiconducting phase, the film is approximately 40% transparent at 1550nm. In contrast, in the metallic phase (at 100°C) the film is nearly 100% absorbing.

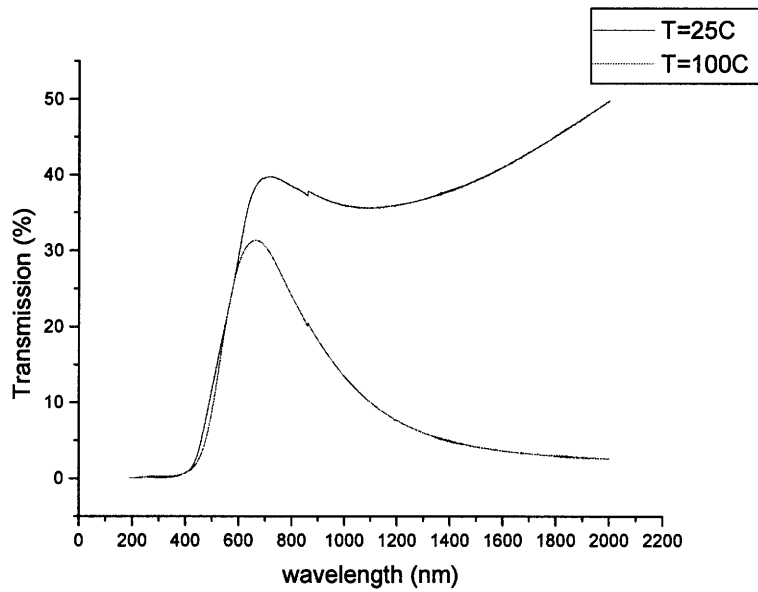


Figure 4-24 Wavelength dependence of optical transmission above and below the phase transition in VO₂ for PLD as-deposited thin films.

The dependence of optical absorption coefficient with energy for VO₂ thin films with different levels of nonstoichiometry controlled in-situ during the PLD film deposition, is shown in Figure 4-25. The variation of the absorption coefficient at 1550nm wavelength for the same set of thin films is shown in Figure 4-26. The optical indices of VO₂ thin films was determined by ellipsometry measurements. The wavelength dependence of the

real and imaginary parts of the refractive index for a thin film deposited at 4 mTorr total oxygen pressure is shown in Figure 4-27.

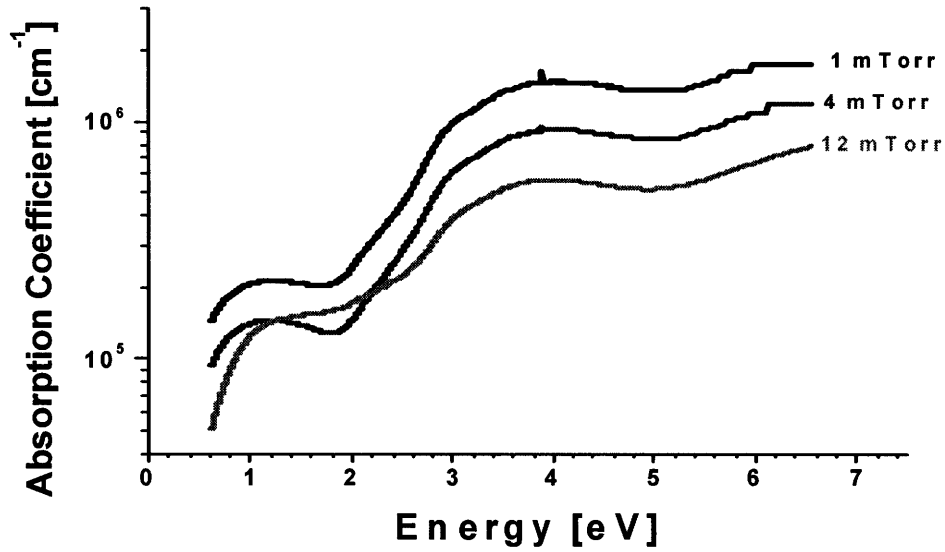


Figure 4-25 Dependence of absorption coefficient of semiconducting VO₂ as a function of energy for thin films under different oxygen working pressures during PLD deposition.

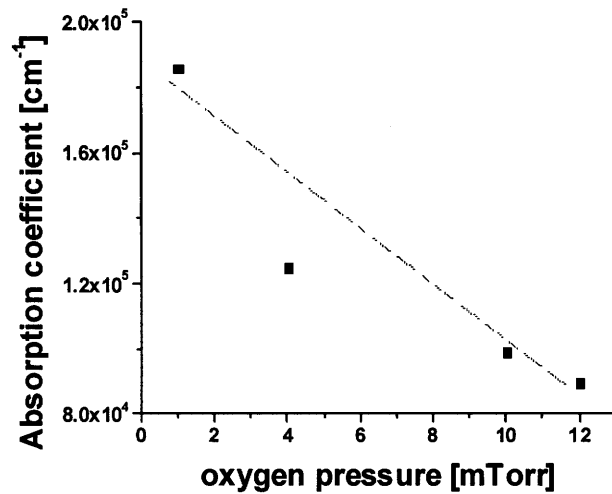


Figure 4-26 Plot of the dependence of the absorption coefficient of VO₂ at 1550 nm wavelength as a function of oxygen total pressure during PLD deposition.

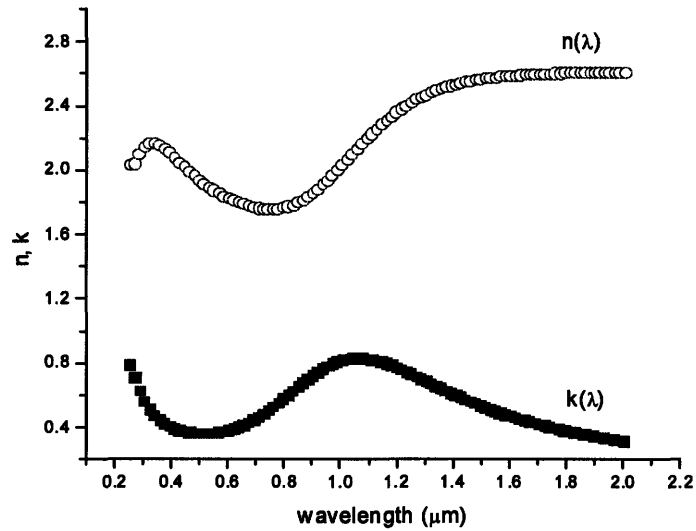


Figure 4-27 Real and imaginary part of the refractive index determined by ellipsometry of thin VO₂ film deposited by PLD at 4 mTorr oxygen total pressure.

4.3 Barium Titanate based E-O Modulator

4.3.1 Thin film growth results

CMOS compatible processing steps were used to fabricate the BT modulator. Control of the orientation of the BT thin film is critical to good performance of the E-O modulator. Thin films grown using pulse laser deposition (PLD) were characterized by x-ray diffraction by Jussi Hiltunen [28], a visiting student and collaborator in this work. The effect of oxygen working pressure during film growth is shown in the x-ray spectra in Figure 4-28. From this figure, it can be seen that films grown at oxygen partial pressures between 1.5mTorr to 20mTorr show BT films highly oriented in the (001)/(100) direction. At higher oxygen pressure, secondary phase peaks appeared.

Rocking curve measurements, also performed by Jussi Hiltunen, showed that films grown at 1.5 mTorr, 10 mTorr and 15 mTorr were epitaxial in nature, given by the nearly zero intensity between the symmetrical reflections. His rocking curve measurements are shown in Figure 4-29.

4.3.2 E-O Modulator Device Simulations

Two different E-O modulator designs were investigated. However, one of the designs was chosen due to ease of fabrication. The approach chosen was a strip-loaded design consisting of a Si_xN_y waveguiding layer on top of the active BT thin film. This design was preferred due to the ease of patterning Si_xN_y compared to patterning the BT thin film. The design of the E-O modulator requires a significant fraction of the optical field to be present in the BT layer so that there is maximum interaction of the applied electric with the optical field.

Optical simulations were carried out using a commercially available mode solver, FimmWave, by Jussi Hiltunen. From the simulations, the optimum thickness of the waveguiding Si_xN_y layer compared to the BT layer was determined so as to maximize the optical field intensity in the the BT layer. A contour plot of the optical field distribution for the stip loaded design is shown in Figure 4-30.

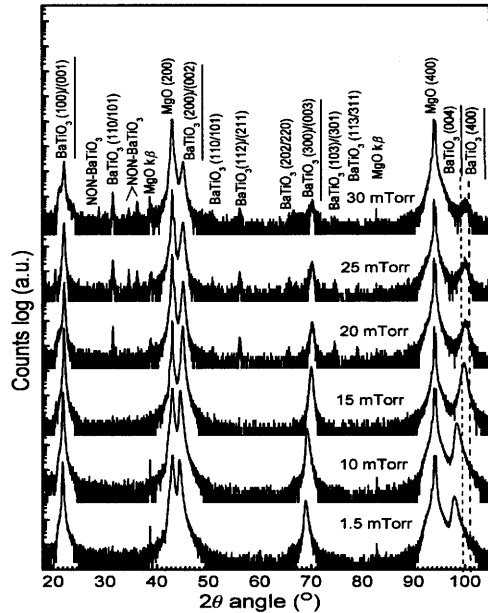


Figure 4-28 θ - 2θ x-ray spectra of thin films of BT grown by PLD. Data courtesy of Jussi Hiltunen.

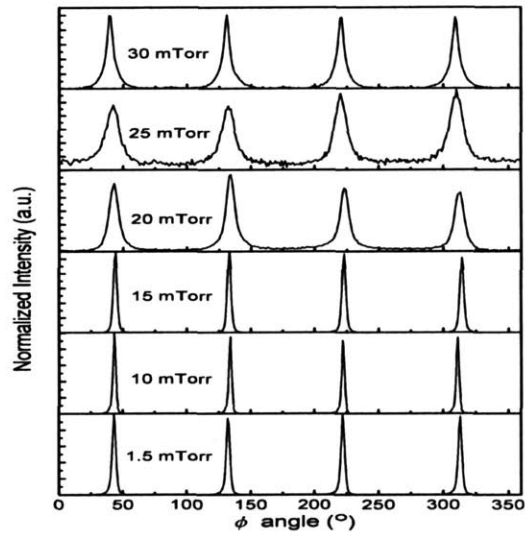


Figure 4-29 X-ray rocking curve results showing the four fold symmetry of the (100)/(001) planes normal to the BT film surface. Data courtesy of Jussi Hiltunen.

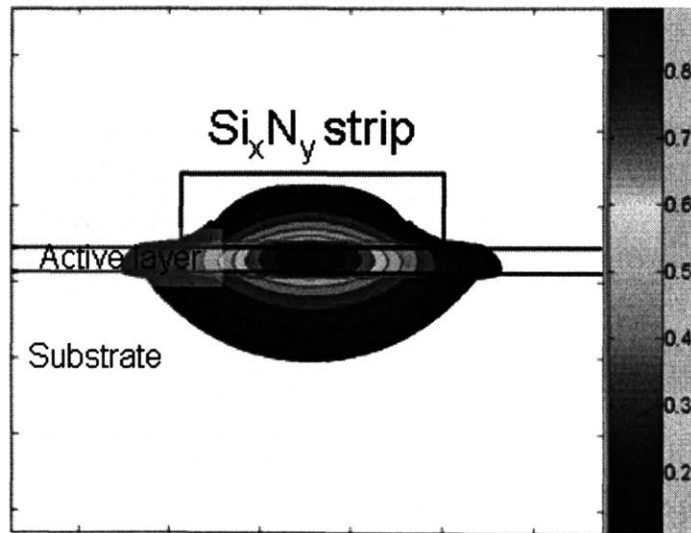


Figure 4-30 Contour plot of optical field intensity distribution for the strip loaded MZ modulator design. Data courtesy of Jussi Hiltunen.

4.3.3 E-O Modulator Fabrication Results

The BT based electro-optic modulator was fabricated using CMOS compatible processing steps. The detailed process steps were given in the experimental section. The final device was imaged and inspected using scanning electron microscopy. A SEM cross section of a typical modulator structure and a top view optical micrograph of a section of the modulator are shown in Figure 4-31.

From the SEM micrograph the square edges of the SiN waveguide can be observed. In addition, the edge walls of the waveguide are relatively smooth, less than 1 nm RMS roughness.

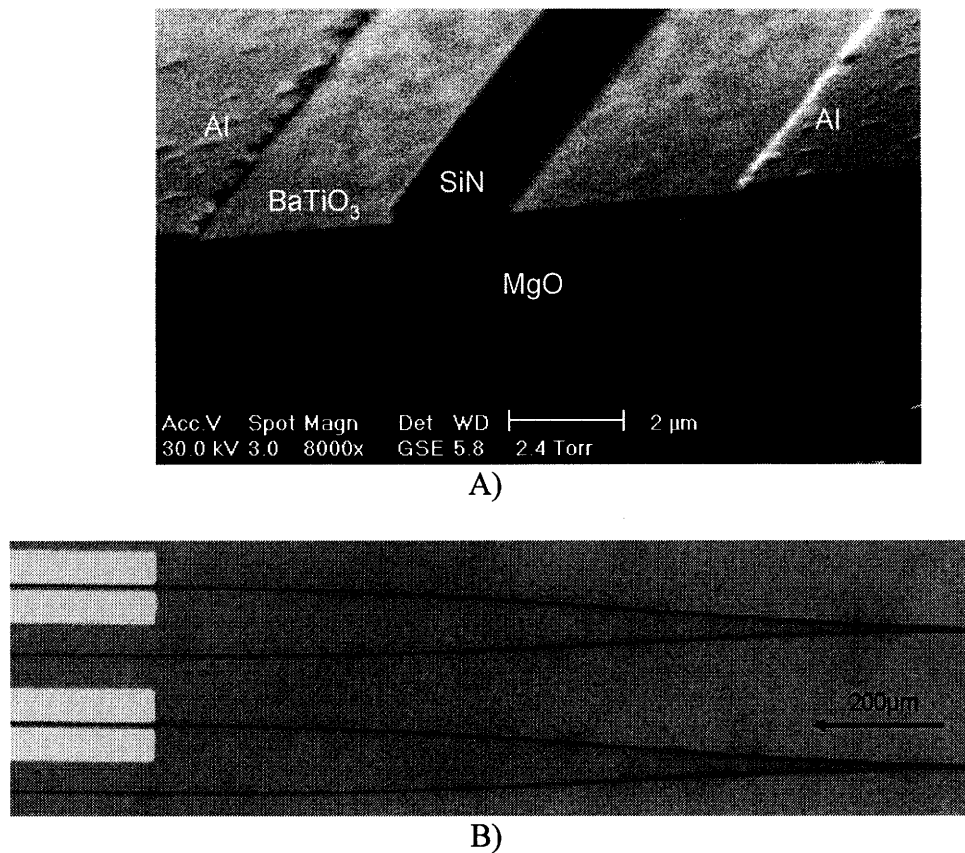
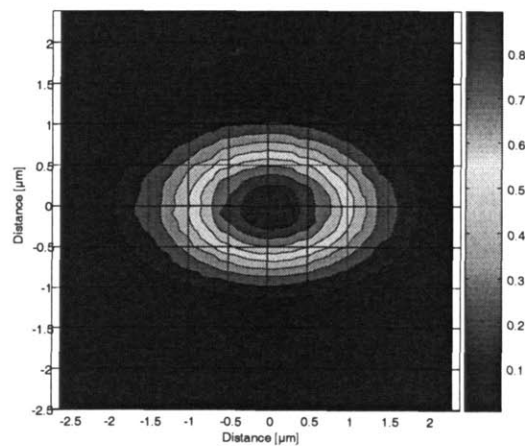


Figure 4-31 A) SEM cross-section image of a fabricated BT E-O modulator. B) Top view optical micrograph showing part section of the Mach-Zehnder structure of two test devices next to each other. The Y-split of the MZ waveguide arms can be seen.

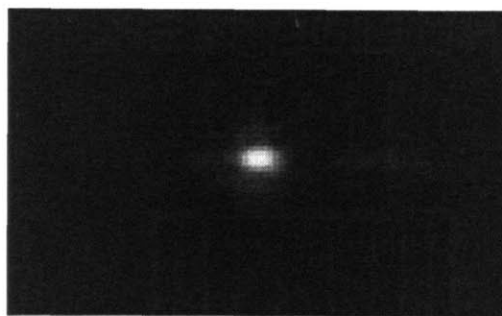
4.3.4 E-O Modulator Test Results

The BT based MZ modulators were tested to determine the active layer electro-optic coefficient. The localized light output from the MZ modulator, with no applied field is shown in Figure 4-32. From this figure it can be seen that the light is guided to within 1 μm diameter, thus demonstrating good confinement of the optical field.

The modulation of intensity in the output side of the MZ modulator was measured as a function of applied electric field between the electrodes of one of the arms of the modulator. A typical intensity versus applied field plot is shown in Figure 4-33.



A)



B)

Figure 4-32 A) Contour plot of the measured optical field intensity as function of position at the output side of the MZ modulator. B) Near-field image captured with an infra-red camera.

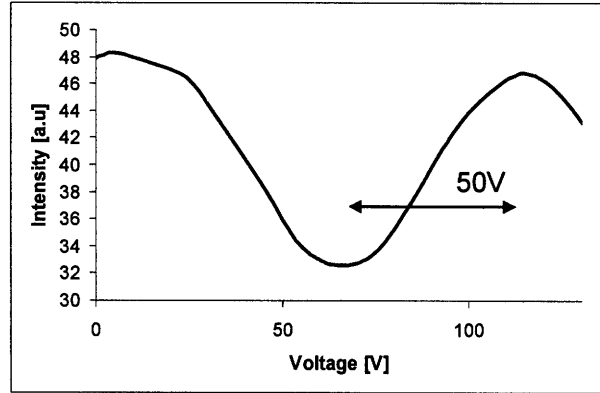


Figure 4-33 Typical intensity modulation in a MZ test structure as a function of applied voltage.

By using the expression [69]

$$r_{eff} = \frac{\lambda \times g}{n^3 \times V_{\pi} \times L \times \Gamma} \quad (38)$$

the effective electro-optic coefficient value r_{eff} can be extracted. V_{π} is the voltage required to cause a 180 degree phase shift in the active arm, n refractive index, g electrode separation, L electrode length and λ the operating wavelength. The overlap factor Γ between the optical and the applied electric field can be obtained by simulation. [69].

The effective electro-optic coefficient was measured for BT films deposited under different oxygen working pressures. The results are tabulated in Table 7.

Table 7 lists the measured effective electro-optic coefficient for different materials and deposition conditions of BT.

Composition	r_{eff} [pm/V]
BT 10mTorr	20
BT 15mTorr	25
BT 20mTorr	no localized output
Ba _{0.6} Sr _{0.4} TiO ₃ (BST)	30
BTO:STO superlattice	73

Chapter 5: Discussion

The objective of this thesis was to design and develop new optical switch and modulator designs and materials for integrated photonic applications. Towards this end, a wavelength selective MEMS-based ring resonator optical switch was designed, fabricated and tested. The results of the MEMS switch, its capabilities and limitations will be discussed further in this chapter.

VO₂ was identified as potential phase-transition based optical switch with, in contrast to the MEMS switch, no macroscopic moving parts. However, the transport properties of VO₂ and the effects of non-stoichiometry on its electrical and optical properties were not systematically studied in the literature. In this thesis, systematic studies of non-stoichiometry and its effects on the optical and electrical properties were performed, the results of which were presented in the results chapter. The implications of these studies in terms of developing a defect and transport model and the implications for optical switching will be discussed in this chapter.

Optical modulation was also identified as a potential opportunity in integrated photonics requiring introduction of new materials. Barium titanate had been identified as a potential material for electro-optic modulation. In this thesis, the results related to the fabrication and testing of a thin film electro-optic modulator were reported. In this chapter the performance of the electro-optic modulator will be discussed.

5.1 MEMS-switch

The SEM images of the fabricated MEMS devices were shown earlier in Figure 4-1. The test results of the integrated MEMS-based ring resonator switch were also demonstrated. This represented the first demonstration of the use of ring resonators for optical switching. Given that the ring resonators are wavelength selective, this was also a first in terms of integrated wavelength selective switching.

The spectral response results showed a switching contrast of 13 dB in the throughput port and 2 dB in the drop port. The switching contrast was much smaller than the designed values, which were 40 dB change in each port. This discrepancy was due to a combination of the imprecise control of the air gap between the top of the ring resonator

and the bottom of the MEMS beams and the less than optimal horizontal alignment of the beams with respect to the throughput and drop ports. As highlighted in the results section, the MEMS beams were slightly displaced in plane towards one of the waveguides, specifically the drop port. This misalignment can be clearly seen from the SEMS images of the ring resonator switch.

In addition, residual stress induced deformation of the beams resulted in a lower than anticipated air gap between the beams and top of the ring resonator, resulting in further optical losses. The residual stresses in the aluminum beams originated from the sputter deposition process and thermal anneal of the aluminum films. The magnitude of the residual stresses in the aluminum thin film was characterized by Gregory Nielson [50] using a cantilever deflection method. The average stress in the aluminum films was determined to be approximately +111 MPa. The net residual stress from the deposition and thermal treatments contributed to plastic deformation of the beams which resulted in buckling and mechanical yielding of the support anchors.

A finite element simulation carried out by Gregory Nielson [50] showed that the Von Mises stress at the anchors, after taking into account the thin film aluminum residual stresses, was in excess of 250 MPa. This value is much higher than the thin film yield stress of aluminum. This plastic deformation at the anchors contributed to the air gap being approximately 0.4 μm compared to the designed valued of 1.2 μm . The combination of residual stress induced deformation and misalignment of the beams during lithography, contributed to the relatively low switching contrasts.

Temporal measurements were carried out to test the switching speed of the ring resonators. The results of the temporal response were shown in Figure 4-3. From this figure it can be clearly seen that the response in the drop and throughput port were in synchrony, having the same response speed. It can also be noted that “switching off” of the resonator, which corresponds to pulling-in the MEMS structure, is much slower, compared to “switching on” the resonator, which corresponds to releasing the pulled-in MEMS structure. The switch time was characterized as the time it takes for the response signal to change from 10% to 90% of full range. The “switch off” time was approximately 60 μs , compared to the “switch on” time which was 10 μs . The slower

“switch off” time was partly due to the relatively slow voltage driver. The voltage amplifier that was used was driven at its maximum speed, at 8 kHz. A square wave voltage was used. At this maximum frequency, the voltage amplifier took about 60 μ s to reach the maximum of the square wave voltage. Thus the “switch off” speed was equipment limited.

5.1.1 Titanium Nitride for enhanced optical switch contrast

Titanium nitride was identified as a candidate CMOS compatible material to replace aluminum as the material for the mechanical beam [64]. TiN having a superior density to stiffness ratio compared to aluminum and silicon, for example, was one reason for this choice. Control of the residual stress was another major reason. As stated earlier, due to the relatively low yield stress of aluminum coupled with significant residual stress resulting from the deposition process, an alternate material with larger yield stress was desired. Young’s modulus values reported for TiN tend to be as high as 400 GPa [41]. The failure strength of TiN is of the order of 5 GPa. Given this high stiffness and failure strength, TiN is capable of sustaining larger residual stresses, without yielding.

Yet, the TiN films deposited by reactive sputtering showed significant as-deposited compressive stress, approximately 1GPa. Given the nature of the deposition process, shot-pinning, a phenomenon where Ar ions from the sputter plasma, was believed to result in Ar ions being embedded within the TiN film. The Ar atoms, being larger than both Ti and N, are believed to have contributed to the compressive stress by occupying more volume than is available in the TiN lattice. The phenomenon of shot-pinning is a very common occurrence in sputter deposited films.

TiN beams that were released before any thermal treatment showed significant buckling due to compressive stress. The average stress was controlled through high temperature anneals. TiN films annealed at 500°C in a nitrogen ambient showed an average residual stress at room temperature of +40 MPa. TiN beams released after the anneal step showed very minimal buckling compared to aluminum. The influence of the temperature treatment on the beams can be seen in Figure 4-4.

Whilst the high temperature anneal step helped minimize residual stresses, one of the draw backs of the heat temperature treatment of TiN was the formation of TiSi₂ as confirmed by XRD results in Figure 4-7.

A potential solution for circumventing the formation of TiSi₂ is to sacrificially remove the poly-silicon layer before the thermal treatment. This approach was not successful, however, as the as-deposited stress was significant and when released, the beams were significantly damaged. Therefore, it is necessary to control the deposition stress. The compressive stress during sputtering can be controlled by controlling the substrate bias during deposition. This approach has been reported to give good results [31].

Once the problem of silicidation of Ti can be overcome, TiN promises to be an attractive solution for replacing aluminum in the optical switch. As mentioned, given the high stiffness to density ratio and larger failure strength of TiN compared to many other metals used in MEMS devices, TiN is a very attractive material for use in MEMS devices. TiN is also known to have a passivated surface. This is an additional advantage for MEMS devices, as the passivated surface minimizes stiction effects, a common problem in MEMS devices.

5.1.2 Summary of MEMS Switch

Despite the relatively low switching contrast reported, the device concept of using ring resonators for wavelength selective optical switching was clearly demonstrated. This represents the first reported results in the literature showing optical switching of wavelength selective ring resonators and is quite significant as it provides a potential solution to wavelength selective optical switching of reconfigurable add-drop multiplexers (ROADM). The reported switching time of 60 μ s is well within the requirements for such a function in an optical network. This MEMS-based switch occupies a much smaller footprint when compared to other MEMS-based optical switches. The MEMS switches reported here occupy an area of approximately 150 μ m x 20 μ m which can be contrasted with reported MEMS free-space based optics which are reported to occupy areas of few square millimeters. Furthermore, given that the mechanical beams used in the MEMS devices in this report were electrostatically

actuated, this resulted in currents during switching of less than a few micro amps. This led to a total power consumption of approximately $1 \mu\text{W}$.

Given the advantages of small device footprint, low power consumption, relatively fast switching speeds and wavelength selective optical switching, we believe that this work has contributed significantly towards the realization of integrated optical add-drop multiplexers (OADM's).

The relatively low switch contrast observed in the throughput port, approximately 2dB, compared to design expectation of 40dB, was due to the residual stresses introduced in the aluminum film. The residual stresses were significant enough to contribute to plastic yield at the anchors of the beams, leading to *pulled-in* structures, which in turn resulted in the air gap between the top of the resonator and bottom of the aluminum structure being as much as 1/3 of the designed value. Control of the residual stresses in aluminum was found to be challenging as temperature excursions as small as 50°C lead to significant stress gradients. Given the relatively low value of the yield strength of aluminum (~ 200 MPa), yielding was inevitable.

TiN, having a failure strength of approximately 3 GPa, was identified as a solution to this problem. TiN was also identified to have a superior stiffness/density ratio compare to poly-silicon, which is a standard MEMS material. Optical switching of ring resonators with TiN membranes was not carried out due to early termination of the project by the sponsors. As future work, it is recommended that TiN be used as the mechanical membrane in ring the ring resonator switch, with potentially larger switch contrasts expected, compared to what was obtained with aluminum.

5.2 Vanadium (IV) Oxide

It had been shown in the literature that VO_2 has a semiconductor-metal transition accompanying a monoclinic-tetragonal phase transition. This phase transition based discontinuity of the electrical conductivity could be exploited for optical switching, utilizing the corresponding change in the absorption coefficient. However, the results reported in the literature showed significant scatter in the absolute conductivities in the semiconducting and metallic phases. In addition, the conductivity jump at the phase

transition temperature varied between a factor of 100 to 5000. In order to understand the origins of the scatter of the data, the effects of non-stoichiometry on the electrical and optical properties were investigated. A transport model for VO₂ was developed based on electrical property measurements. The results and their implications are discussed further in the following sections.

5.2.1 Electrical Properties of VO₂

Vanadium (IV) oxide displays a characteristic phase transition as was shown by the x-ray diffraction results of the vanadium oxide powder as a function of temperature between 25°C and 100°C. The change in crystal structure from the low temperature monoclinic to the high temperature tetragonal phase was observed at 65°C.

While the high temperature phase ($T > 65^\circ\text{C}$) of VO₂ is known to be metallic-like, its electrical properties had not been examined at elevated temperatures under conditions where the material could come into equilibrium with its environment. Its metallic nature under these conditions was confirmed by high temperature electrical conductivity measurements (see figures 4-10, 4-13 and 4-15). Furthermore, the magnitude of the conductivity above the phase transition, approximately 100 to 5000 S/cm, was found to depend on the degree of non-stoichiometry of VO₂ and the temperature.

Given VO₂'s metallic character, it was further surprising to see a conductivity maximum, at approximately 600°C, in the $\log \sigma$ vs reciprocal temperature plot obtained at fixed stoichiometry between 100°C and 1000°C (figure 4-13). Of particular concern was the appearance of a thermally activated conductivity from above the phase transition to approximately 600°C. To investigate this further, thermoelectric power (TEP) measurements were carried out over the same temperature range. The TEP exhibited little change varying only between $-5\mu\text{V/K}$ and $-10\mu\text{V/K}$. The sign of the TEP coefficient was negative, pointing to electrons as the majority carriers. The carrier concentration calculated from the TEP coefficient, was of the order of 10^{22} carriers/cm³, clearly consistent with metallic conductivity (see figure 4-14).

The temperature invariant thermoelectric power coefficient at temperatures above the phase transition indicates an invariant carrier concentration over that temperature range.

Given that conductivity is a product of $nq\mu$ (where n is the carrier concentration, q , the elementary charge and μ , the mobility) and given that the carrier concentration was invariant with temperature, the change in conductivity must, therefore, be due to an activated mobility, for example, by the small polaron mechanism. The expression for activated mobility is given by:

$$\mu = \frac{\mu_0}{T} \exp\left(-\frac{E_A}{kT}\right) \quad (39)$$

Incorporating the above equation into the conductivity expression (equation 19) leads to a modified conductivity expression for mobility activated conductivity:

$$\sigma = \frac{\sigma_0}{T} \exp\left(-\frac{E_A}{kT}\right) \quad (40)$$

where E_A corresponds to the activation energy for mobility. Based on this equation, a plot of $\log(\sigma T)$ versus $1/T$ should be linear as demonstrated, within experimental error, in Figure 4-14. The magnitude of the activation energy calculated from this plot, 0.08eV, is in the range reported for highly conducting metal oxides, e.g. $\text{La}_{1-x}\text{Sr}_x\text{MnO}_{3+d}$ [47]

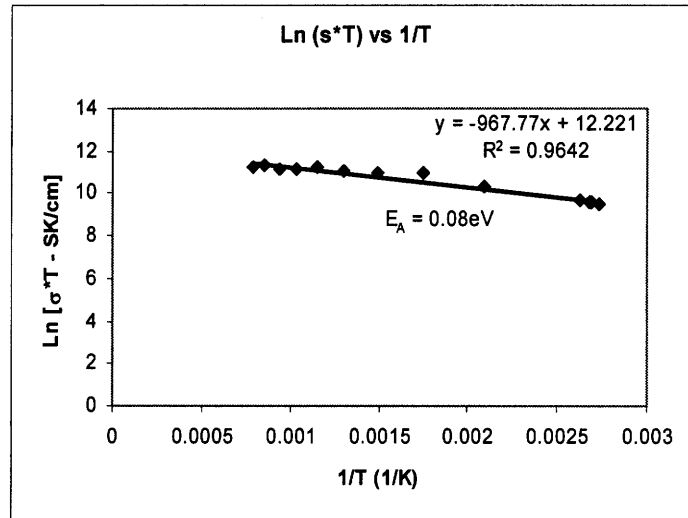


Figure 5-1 Plot of conductivity vs reciprocal temperature assuming an activated mobility model.

5.2.2 PO₂ dependence of conductivity

High temperature conductivity measurements were carried out as a function of oxygen partial pressure between 10^{-2} atm and 10^{-14} atm on bulk samples. Measurements were carried out at 950°C, 1000°C, and 1050°C. Measurements carried out at lower temperatures required extremely long equilibration times and were therefore avoided. Based on literature reports, the VO₂ phase is stable between approximately 10^{-3} atm and 10^{-6} atm in this temperature range. The actual VO₂ stability range was mapped onto the conductivity vs oxygen partial pressure plot (figure 3-10). From the conductivity data, a change in conductivity of factor of five can be seen at PO₂'s between 10^{-10} atm and 10^{-6} atm. This is suspected to be due to a phase changes in going from V₂O₃ to the V_nO_{2n-1} Magnelli phases and then on to VO₂. The gradual change in conductivity between 10^{-10} atm and 10^{-6} atm is consistent with transitions through closely spaced Magnelli phases.

Within the VO₂ phase range, the conductivity remained largely independent of oxygen partial pressure. Based on the defect model that was developed earlier, a 1/5th dependence in the log-log plot of conductivity vs PO₂ would be expected. However, given that in this high temperature range VO₂ is metallic, having carrier concentrations of the order of 10^{22} carriers/cm³, a change in conductivity due to oxygen partial pressure dependent carrier concentration is not expected.

TEP measurements carried out over the same oxygen partial pressure ranges revealed an increase in the TEP coefficient in going from the reduced end of the VO₂ phase boundary to the oxidized end. This is consistent with a decreasing number of electrons with increasing PO₂. The slope of the logarithm of the calculated carrier concentration (assuming a density of states in the conduction band of 10^{22} states/cm³) versus log PO₂ was equal to -0.07, a value again, much smaller than that expected from the dilute solution approximation.

In conclusion high temperature oxygen partial pressure measurements revealed little additional information regarding the defect properties of VO₂ given its metallic character. However, changes in stoichiometry are still expected as a function of PO₂. The influence of PO₂ on the properties of VO₂ should be more apparent in the properties of the

semiconducting phase. This hypothesis was tested through the iso-stoichiometry conductivity and TEP measurements.

5.2.3 Non-stoichiometry effects on Semiconducting Properties of VO₂

The effects of non-stoichiometry on the semiconducting properties of VO₂ were measured through iso-stoichiometry conductivity and TEP measurements. The bulk samples were annealed at high temperature at controlled PO₂ to obtain controlled values of δ , in VO_{2- δ} . These compositions were then slow cooled in a small sealed quartz tube.

As explained in the experimental section, the buffering action of the bulk material fixes δ in VO_{2- δ} . The electrical conductivity measurements for samples annealed under different oxygen partial pressure, and hence different δ values was shown in figure 4-12.

Due to the narrow PO₂ range over which VO₂, it was not possible to freeze high temperature nonstoichiometry down to room temperature by simply cooling in a fixed PO₂ environment due phase changes. Evidence of this can be seen, for example, in Figure 4-3. Hence, this alternate method of freezing the non-stoichiometry by cooling in a sealed environment.

From this figure, it can be clearly seen that high temperature anneal conditions, and hence non-stoichiometry δ , has a significant impact on the semiconducting properties. The conductivity jump between the metallic and semiconducting phase was only 10¹ for samples annealed (at 100 ppm O₂) close to the reduced end of the VO_{2- δ} . The conductivity jump for samples annealed at the oxidized end (at 1000 ppm O₂), on the other hand, was approximately 10^{3.5}.

Room temperature x-ray diffraction results of the post-annealed samples confirmed the monoclinic VO₂ phase for the 100 ppm and 1000 ppm O₂ anneal conditions. Therefore, given that the phase was the same, the only explanation for the difference in the conductivity jump is a non-stoichiometry effect on the samples.

The magnitude of the conductivities in the semiconducting phase at a given temperature differed between specimens by up to 3.5 orders of magnitude. This difference in

magnitude of the conductivity, induced by the different high temperature anneals, is also correlated to changes in the degree of non-stoichiometry.

Based on our defect model, oxygen deficiency is accommodated in VO_2 by introduction of interstitial vanadium ions. Interstitial vanadium ions are expected to serve as donors. As the non-stoichiometry increases, the number of interstitial vanadium ions incorporated into the $\text{VO}_{2-\delta}$ lattice increases, thereby contributing to a larger free carrier concentration in the semiconducting phase compared to the sample with a lower degree of non-stoichiometry. The free carrier concentration will vary linearly with the number of donors, N_D , if in the saturation regime and as $N_D^{1/2}$ if in the freeze out regime [60].

Next, the position of these donor states relative to the conduction band edge is addressed.

The activation energy of the electrical conductivity in the semiconducting phase was typically quite low and dependent on stoichiometry. The activation energy was 0.07 eV for samples annealed near the reduced end and 0.16 eV for samples annealed near the oxidized end of the phase boundary. The question to address is what fraction of these activation energies are related to carrier generation versus carrier mobility. TEP measurements, which are sensitive only to carrier concentration, are examined to clarify this question.

Based on the defect model, which assumed an n-type behavior, samples annealed at the oxidized end of $\text{VO}_{2-\delta}$ should have lower carrier concentration due to lower number of vanadium interstitial defects. This was indeed confirmed by TEP measurements (see figure 4-15). Samples annealed at the reduced end of the phase boundary (samples annealed at 100 ppm O_2) exhibited lower TEP values as compared to samples annealed at the oxidized end of the phase boundary (samples annealed at 1000 ppm O_2). The sign of the TEP coefficient confirmed that the majority carriers in the semiconducting phase were also n-type.

The thermal activation of the thermopower indicates that the carrier concentration is thermally activated. This activation energy was calculated to be approximately $0.02 \text{ eV} \pm 0.001 \text{ eV}$ for the 1000 ppm sampled. Compared to the conductivity activation energy, $0.16 \text{ eV} \pm 0.001 \text{ eV}$ for the same sample, it can be clearly seen that there is a small temperature dependent activation of electrons and a stronger temperature dependence of

the mobility. This thermally activated mobility indicates either a small polaron hopping behavior or a trapped mobility behavior.

If this sample is modeled as exhibiting small polaron behavior, the carrier concentration can then be calculated from the thermopower assuming the density of states in the conduction band is equal to the vanadium cation density. Assuming a cation density of $\sim 10^{22} /\text{cm}^3$, the calculated room temperature carrier concentration is 5.64×10^{21} carriers/ cm^3 . The mobility can then be calculated using this carrier concentration and equation 19. The calculated mobility is $4.7 \times 10^{-5} \text{ cm}^2/\text{Vs}$. The low magnitude of mobility ($< 1 \text{ cm}^2/\text{Vs}$) obtained here is quite typical of solids exhibiting small polaron behavior [76].

This behavior can also be modeled like conventional semiconductor behavior, like silicon. The carrier concentration in this case can be calculated assuming an effective mass of $3 \cdot m_e$ giving an effective density of states of in the conduction band of $1.3 \times 10^{19} /\text{cm}^3$. The carrier concentration and mobility thus calculated were: 7.33×10^{19} carriers/ cm^3 and $3.66 \times 10^{-2} \text{ cm}^2/\text{Vs}$ respectively. Therefore, it can be seen that assuming even the most extreme conditions, the low mobility calculated demonstrates an activated mobility mechanism.

The temperature dependent TEP measurements in the semiconducting phase were used to determine the carrier concentration dependence on temperature, which enabled the determination of the activation energy for carrier generation. A plot of the logarithm of carrier concentration versus reciprocal temperature was used to extract the activation energy of the carrier concentration (see figure 4-16) and was found to be $0.02 \text{ eV} \pm 0.001 \text{ eV}$ for the sample annealed at 1000 ppm O_2 . This indicates that the donors, believed to be vanadium interstitials are quite shallow, similar in magnitude to donor level ionization energies found in more conventional semiconductors like silicon where values range between 0.02 eV to 0.05 eV depending on the donor element. This low value for the donor ionization energy is entirely consistent with the high reported relative dielectric constant of VO_2 of approximately 100 [46].

The donor ionization energy of the order of 20 meV therefore suggests that the majority of the measured activation energy for conduction is related to the electron migration or

hopping energy. This would suggest therefore that the migration energy varies from 0.05 eV for samples annealed near the reduced end and 0.14 eV for samples annealed near the oxidized end of the phase boundary. Stoichiometry dependent migration energies in solids exhibiting small polaron behavior has been observed before and is attributed to variations in wavefunction overlap between cations due to differences in defect ordering [76]. Furthermore, it is worth noting that VO_{2-x} with a lower degree of non-stoichiometry has the low number of defect states and therefore, a lower free carrier concentration. In the small polaron hopping model, the positive ion cores of the lattice contribute to the ‘drag’ of the electrons. As the number of free electrons increase, these free electrons are better shielded from the ion cores and therefore may be expected to exhibit a lower activation energy for electron mobility.

The activation energies for conductivity and carrier concentration reported here are not consistent with one other early report in the literature by Kitahiro et al [35]. In their report, the thermoelectric power (TEP) and DC electrical conductivity were measured as a function of temperature in single crystal VO_2 whiskers. The carrier concentration dependence on temperature determined from the TEP measurements was found to have the same activation energy as the DC electrical conductivity implying that carrier generation was dominating the temperature dependence. It should be noted, however, that their material exhibited much lower carrier concentration suggesting a compensated rather than a donor-dominated material. This may be related to the manner in which the whiskers were grown, possibly incorporating compensating impurities during crystal growth.

5.2.4 Non-stoichiometry

Non-stoichiometry in VO_2 was measured between 500°C and 650°C by coulometric titration. The total non-stoichiometry and absolute non-stoichiometry were determined. The starting oxygen partial pressure inside the titration cell was 0.21 atm. At this partial pressure and temperature range of testing (500°C – 650°C) the stable phase in the VO_x system is V_2O_5 . As oxygen was pumped out, the powder inside the titration cell was reduced. The change in the equilibrium oxygen partial pressure inside the titration cell as a function of amount of oxygen pumped out was shown in figure 4-15.

In this figure, oxygen partial pressure plateau regions correspond to two phase regimes. Regions of sharp change in PO_2 with amount of oxygen pumped correspond to single phase regimes. The non-stoichiometry was therefore, the width of the sharp PO_2 change regime. From the data shown, the onset of the single phase regime of VO_2 near the oxidized end of the phase boundary was not quite clear. The two phase plateau of V_6O_{13} and $VO_{2-\delta}$ was not entirely flat. A small slope was observed. This slope was probably due to polarization effects inside the cell, and insufficient time given to de-polarize the cell. Nonetheless, the transition to single phase regimes was determined by the presence of an inflexion point. The PO_2 's at the upper and lower phase boundary, as determined from the coulometric titration data match closely to those reported by Bruckner et al [7] within a margin of error.

From the plot of the number of moles of oxygen pumped as a function of PO_2 , the total non-stoichiometry, $\Delta\delta$, was calculated. $\Delta\delta$ was calculated assuming $\delta = 0$ at the oxidized side of the VO_2 phase boundary. The total non-stoichiometry, $\Delta\delta$, ranged from 0.1 at 650°C to 0.01 at 500°C. This implies that the total non-stoichiometry increases with increasing temperature as commonly observed in nonstoichiometric solids [37].

As described in the results section 4.2.8, the absolute stoichiometry, δ , was determined by non-linear least squares fitting the total non-stoichiometry by an expression of the form given in equation 5. The results of the fitting indicated an interstitial-vacancy transition in VO_2 for 500°C, 550°C, and 600°C. The fit for data of 650°C was not of good quality, possibly due to noisy data points resulting from leakage, yielding an unreasonable δ^* value.

Based on the fitting, $\delta = 0$ in $VO_{2-\delta}$ occurs at $10^{-13.5}$ atm, $10^{-10.2}$ atm, and $10^{-8.9}$ atm at 500°C, 550°C, and 600°C respectively.

From the non-linear least square fit, values of K_R , K_F and K_E , the equilibrium constants for reduction, frenkel defect formation and electronic-defect formation respectively were determined. Activation energies for K_R , K_F and K_E were found to be 2.7 eV, 0.71 eV and 0 eV respectively. The low activation energy for the frenkel defect formation implies an intrinsically highly defective material. This correlates well with the measured total non-stoichiometry as high as 5%.

It should be pointed out that the model developed for VO₂ assumed a dilute solution model of defects. The electron concentration was assumed to be equal to the hole concentration at high temperatures. These assumption are normally valid at high temperatures for semiconducting oxides. However, given that above 65°C VO₂ is metallic like, having a large carrier concentration (of the order of 10²¹ carrier/cm³), the assumption of dilute solution of electronic defects can not be valid. Nevertheless, it may be useful to examine the related scenario of a metallic phase in which the electron density is also independent of PO₂.

In the stoichiometric regime where $n = p$, the expected power law dependence of PO₂ versus δ is -1 in the reducing regime and +1 in the oxidizing regime, as was shown in Table 3. The best fit obtained however indicated a power law dependence of -1/5 and +1/5 in the reducing and oxidizing regimes respectively.

In the dilute solution model in the near stoichiometric regime where $n = p \neq f(\text{PO}_2)$, the expected power law dependence of δ versus PO₂ is -1 in the reducing regime and +1 in the oxidizing regime, as was shown in Table 3. It is understood that if the electron concentration is high, its concentration should be replaced by its activity in any mass action relation. As long as its activity is PO₂ independent, one can still expect other defects in low concentrations to follow the predictions of the dilute solution model. Therefore, an attempt was made to fit the nonstoichiometry data to the power law dependences of ± 1 . The best fit, however, was obtained with a power law dependence of -1/5 and +1/5 in the reducing and oxidizing regimes respectively.

In considering this continued discrepancy, the lower than expected power law values are likely related to one or more features of the VO₂ system. First, is the very narrow existence range of VO₂ and the difficulty with the titration data to very precisely establish the exact bounds of the VO₂ phase field. This latter factor, we suspect, is due to somewhat sluggish kinetics and potential oxygen leakage through the titration cell seals. This coupled with the already high degrees of nonstoichiometry exhibited by the VO₂ phase would tend to weaken the apparent δ versus PO₂ dependence.

Despite this anomaly, the observed temperature independent K_E is at least consistent with the observation that VO₂ is metallic with a temperature independent carrier concentration.

5.2.5 Thin film electrical properties

The DC electrical conductivity of VO₂ thin films deposited by PLD displayed similar characteristics to the bulk properties. The jump in conductivity at the phase transition was approximately a factor of 10³. The activation energy in the semiconducting phase varied between 0.21 eV to 0.31 eV. The lower activation energy was obtained for samples deposited in lower oxygen working pressures (pressure of approximately 1 mTorr). Samples deposited at 12 mTorr showed the higher activation energy of 0.31 eV.

The main difference between the thin film and bulk conductivity measurements was that in the thin films, there was very little difference in the magnitude of the conductivity jump at the phase transition. In the bulk samples, the conductivity jump varied between 10 to 5000. In the thin films, the change was consistently approximately 1000.

This measurement nonetheless, showed once again that the transport properties are significantly affected by the oxygen content in the sample as evidenced by the change in activation energies and in the magnitude of conductivity.

5.2.6 Optical Properties of VO₂ thin films

Optical absorption measurements were performed on thin films of VO₂ that were deposited at different oxygen working pressures during PLD deposition. Peaks in the absorption spectrum were observed at approximately 1 eV, and the development of a absorption peak shoulder at approximately 2.5eV was also observed. An additional peak was observed at ~ 4 eV.

The absorption coefficient of the films were observed to increase with decreasing oxygen working pressure. From the electrical conductivity measurements (Figure 4-17) it was observed that films deposited at lower oxygen total pressures led to larger room temperature conductivities which possibly implies the presence of a higher concentration of free carriers in these more reduced films. Thus, the observed increase in the absorption coefficient can be correlated with increasing free carrier concentration. This observation is consistent with the electrical transport model developed in this thesis, where it was argued that lower oxygen partial pressures within the VO₂ existence range leads to a higher degree of frozen-in donor defects which in turn results in larger free carrier

concentration. The dependence of the absorption coefficient on free carrier concentration in semiconductors is given by equation 41 [49, 55]

$$\alpha = \frac{\lambda^2 q^3}{4\pi^2 c^3 n \epsilon_0} \left(\frac{N_n}{m_n \mu_n} \right) \quad (41)$$

where α = absorption coefficient, λ = wavelength, q = elementary charge, c = speed of light, n = real part of refractive (= 2.57 at 1550nm) index, ϵ_0 = permittivity of free space, N_n = free carrier concentration, m_n = effective mass of the free carrier, and μ_n = mobility of the free carrier.

The room temperature electrical conductivity ratio for the samples deposited at 12 mTorr and 1 mTorr respectively was approximately a factor of 6. The experimentally observed variation of the absorption coefficient for the same two samples showed a similar factor of 6 difference which is consistent with the electrical measurements and supports a model in which absorption is controlled by the free electron density.

5.2.7 Summary of the Transport Characteristics of VO₂

The transport characteristics of semiconducting VO₂ are strongly influenced by the level of non-stoichiometry. At high temperatures, interstitial vanadium in VO₂ is assigned to be the dominant defect specie, contributing to the non-stoichiometry. The large degree of non-stoichiometry at high temperatures, when frozen-in below the semiconductor-metal phase transition, contributes to higher electrical conductivity in the semiconducting phase. This higher electrical conductivity in the semiconducting (monoclinic phase) can be explained by the increase in the carrier concentration due to larger number of shallow donor like ionized *frozen-in* defects.

As was pointed out earlier, the semiconducting nature of VO₂ in the monoclinic phase is due to reduced overlap between the vanadium d-orbitals, due to pairing of vanadium cations and distortion of the tetragonal structure to form the monoclinic form. At the largest distortion, the d-orbital overlap is minimum and conductivity lowest. This would correspond to the stoichiometric point. As VO₂ deviates from stoichiometry, in the reducing regime, more interstitial vanadium cations are formed leading to a higher carrier density. Further, as the number of interstitial vanadium cations increases, the distortion in

the monoclinic phase reduces, reducing the separation between paired set of vanadium cations, leading to higher degree of d-orbital overlap, thus increasing the mobility also observed in this study. For example, the migration energy of 0.14 eV for specimens annealed at 1000 ppm O₂ (lower degree of non-stoichiometry) reduces to 0.04 eV for specimens annealed at 100 ppm O₂ (larger non-stoichiometry), consistent with larger non-stoichiometry leading to lower lattice distortion of the monoclinic phase.

In the metallic phase, the carrier concentration was relatively high and temperature independent. Also, as in the semiconducting phase, a small polaron hopping like activated mobility, was observed.

5.2.8 Implications for VO₂ based optical switching

VO₂ was identified as a potential material that could be used in conjunction with ring resonator structures for optical switching. However, the absorption coefficient in the semiconducting phase was as high as $2 \times 10^5 \text{ cm}^{-1}$ at room temperature. Minimizing the absorption coefficient by control of the stoichiometry was identified as a possible approach. The study of the electrical transport properties of VO₂ showed that larger amounts of vanadium interstitial defects were frozen as VO₂ deviates from stoichiometry in the reducing regime. The large room temperature absorption was correlated to the free carrier concentration from the thin film measurements. However, the lowest obtained room temperature absorption coefficient was $9 \times 10^4 \text{ cm}^{-1}$. The absorption coefficient in the high temperature phase was approximately $5 \times 10^5 \text{ cm}^{-1}$. This almost factor of 5 change in the absorption coefficient could be utilized in a resonator type structure.

This high value of VO₂ implies that it cannot be used directly on top of an active waveguide, for example, on top of the ring resonator waveguides. A dielectric cladding layer between the VO₂ and the active waveguide is needed.

One potential advantage of exploiting the phase change in VO₂ as opposed to using a MEMS structure to switch the ring resonators is the faster switching speed possible, given the observed pico-second switching in VO₂ [9]. This fast switching speed coupled with the factor of 5 change in absorption coefficient could also be utilized for optical modulations applications. A possible means of actuating the phase transition is by current

induced heating of VO_2 , or possibly using a high electric fields as claimed possible by Kim [32] and Stefanovic [68]. A schematic showing the possible implementation of the VO_2 based ring resonator switch is shown in Figure 5-2

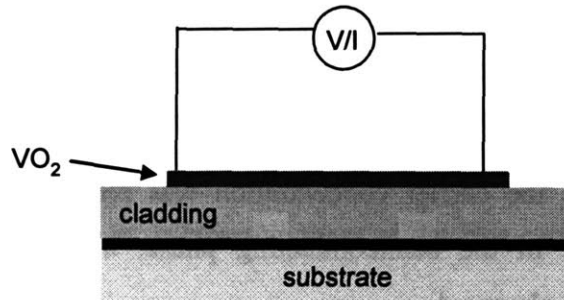


Figure 5-2 Schematic of possible implementation of a ring resonator switch using VO_2 .

5.3 Barium Titanate E-O Modulator

5.3.1 Structure

The effect of the oxygen working pressure during deposition of BT films was found to be crucial in controlling thin film orientation. The desired orientation was (001). This orientation was obtained at oxygen working pressures of 15 mTorr and lower. The measurements of the in-plane and out-of-plane lattice parameters showed the effective stress in the films in samples grown at 1.5 mTorr, 10 mTorr and 15 mTorr.

For the optimum electro-optic effect, the ferro-electric phase of BT was preferred. BT displays ferroelectric properties in the tetragonal phase. In bulk BT, a ferroelectric to paraelectric phase transition occurs at 120°C. This corresponds to a change in crystal structure from tetragonal to cubic. Thus stabilizing the tetragonal crystal structure is needed given that during processing, the transition temperature would normally be exceeded. In-plane tensile stresses for (001) oriented films could drive BT from tetragonal to cubic, thus inducing the ferro- to para- electric transition.

Measurements of dielectric constant and in-plane and out-of-plane lattice constants of the films as a function of temperature, however, showed that the ferro- to para- electric transition was displaced to higher temperatures [28]. The characteristic sharp discontinuity in the dielectric constant observed in bulk BT was not observed in the thin

films. A rather broad peak in the dielectric constant was observed. The peak position was at approximately 300°C. The in-plane and out-of-plane lattice parameter measurements at high temperatures converged towards cubic lattice parameters, but were never quite cubic. The crystal structure remained slightly tetragonal.

The dielectric constant and lattice parameter measurements confirmed that BT films grown at 1.5 mTorr, 10 mTorr and 15 mTorr were ferroelectric in nature and that the ferro-electric phase was stabilized up to 300°C.

5.3.2 Electro-optic Performance

The effective electro-optic values measured for the different growth conditions ranged from 18 pm/V to 25 pm/V for BT. These were effective electro-optic coefficients, r_{eff} . The r_{42} value calculated from the effective E-O coefficient was 70 pm/V for the 10 mTorr sample. An r_{42} value for the 15 mTorr sample could not be determined as that sample had mixed (001) and (100) orientations out of plane.

The r_{42} value determined for the 10mTorr sample was much smaller than the bulk value ($r_{42} = 820$ pm/V). This significant difference could be due to the clamping of the BT lattice due to lattice parameter mismatch.

Wessel's group in Northwestern University have published a series of report on the performance of BT-based thin film modulators [69-73]. In their reports, the effective E-O coefficients were increased from 35 pm/V to as high as 380 pm/V. No explanations for the observed increases in effective E-O values were given. Their films were grown by a MO-CVD process. It could, therefore, be argued that this process permits layer by layer deposition of BT films, thus minimizing deposition induced residual stresses leading to better epitaxy. None of their reports show x-ray characterization data. Therefore, we were unable to quantify the quality of their epitaxy compared to that in this report.

The effective E-O coefficient measured for the 15 mTorr sample is comparable in performance to LiNbO₃ based commercial bulk crystal modulators. This implies that the bulk crystal function of LiNbO₃ can be replaced with an integrated thin film E-O modulator based on BT thus demonstrating the potential of using BT as a the E-O modulator material in integrated photonics.

Whilst the integration of the BT modulator is attractive, the drive voltage and device sizes were still of the same magnitude as commercial LiNbO_3 based technology. The BT modulator active device length was 3 mm. Despite the success in achieving BT based thin film modulator performance comparable to commercial LiNbO_3 , these effective E-O coefficient for BT are still a factor of 10 smaller than the Wessels group reports [73].

To enable smaller devices, high effective E-O coefficient materials are needed. Several other materials were investigated towards this end. Of particular note was a barium titanate (BT)-strontium titanate (ST) superlattice structure grown by Jussi Hiltunen. The effective E-O coefficient measured for this BT-ST structure was 73p m/V. This value is over a factor of two better than the performance of commercial LiNbO_3 modulators. There are indications that possible further improvements in the effective E-O coefficient based on BT-ST superlattices could be achieved by optimizing the thickness of the BT-ST layers. It has been shown that dielectric tunability (which is a change in the dielectric constant as a function of applied electric field) of BT-ST structures can be optimized by a factor of 10 by manipulation of the BT-ST layer thicknesses. Given the dielectric constant is related to the refractive index and that the E-O effect is essentially a measure of the refractive index tunability (i.e. change in the refractive index with applied electric field), there is promise for a further enhancement of the E-O coefficient in BT-ST super lattice structures.

5.3.3 Summary of BT E-O Modulator

An integrated barium titanate based electro-optic modulator with performance comparable to commercial bulk LiNbO_3 was demonstrated. This is an important achievement given that a thin film modulator can now be integrated on a substrate with a light source and other optical functions such as switches and detectors. Therefore, the demonstration of the thin film E-O modulator addresses one of the key requirements for integrated photonics. Enhancements in the thin film modulator performance were achieved by employing superlattice structures of BT-ST. The performance of this latter device was 2.5 times better than LiNbO_3 . This implies that modulator device sizes can be scaled down by that same factor and therefore, signal significant promise towards enabling integrated photonic devices and modules.

Chapter 6: Conclusions

The increasing demand for bandwidth in many applications ranging from computation to telecommunication was highlighted as a driver for integrated photonic devices. Key components of an integrated photonic chip are switches and modulators. In this thesis, new switch designs and materials and modulators concepts were investigated.

A MEMS-based approach was used to switch wavelength selective ring resonators. This MEMS-based switch was the demonstration of active switching of ring resonators. The approach employed here resulted in a small foot print ($3000 \mu\text{m}^2$ area) device, very low operating power (approximately $1 \mu\text{W}$) and wavelength selective optical switching. TiN was identified as an attractive MEMS structural material and fabrication requirements for effective use of TiN were identified.

VO_2 was identified as a possible optical switch material. The transport and electrical property characterization of VO_2 demonstrated that it has a high degree of non-stoichiometry, approximately 5% at 650°C . The level of non-stoichiometry has a strong impact on the electrical conductivity in the semiconducting phase and a much smaller effect in the metallic phase. A small polaron hopping mechanism was identified as the electron mobility mechanism in semiconducting and metallic VO_2 . Control of VO_2 's non-stoichiometry was demonstrated to be key in controlling the electrical and optical properties of the semiconducting phase. The high optical absorption observed in the semiconducting phase was found to be dependent on the free carrier concentration arising from donor level defects as well as possible band-band absorption. The observed factor of 2 contrast in the absorption coefficient between the semiconducting and metallic phase could be utilized in a ring resonator design for optical switching applications. Further enhanced of the absorption coefficient could be possible by compensation doping. The pico-second switch speeds reported in literature coupled with possible electric field induced phase transition also reported in the literature shows further promise of utilizing VO_2 for realizing fast switch and modulator devices. Further work is needed to explore these concepts.

The concept of barium titanate based thin film electro-optic modulation was explored and was found to have at least comparable performance to LiNbO_3 bulk crystal technology. A BT-ST super lattice structure was identified as a potentially better electro-optic material. This BT-ST thin film super lattice structure demonstrated 2.5 times better performance than bulk LiNbO_3 . Effective electro-optic coefficients as high as 73 pm/V were obtained for the BT-ST structure.

Overall, the demonstration of MEMS-based optical switching and the BT-based E-O modulator work showed significant promise in addressing the need for integrated, miniaturized, low power photonic devices for optical communication applications. The concepts demonstrated could have far reaching impact from practical devices for broadband communication to enabling optical interconnects on chip in memory and logic microprocessors.

Chapter 7: Future Work

7.1 MEMS Switch

The demonstration of switching ring resonators by use of electrostatically actuated MEMS-based bridge structures was a significant step forward. Improvements in the device performance, specifically, the switching contrast is needed. This can be achieved by utilizing TiN-based optical switches which exhibit many attractive features. Control of residual stresses in the mechanical beams is critical as residual stresses lead to unwanted buckling of released structures. It was shown that residual stress can be controlled by controlled temperature anneals. It is also expected that the deposition stress could be controlled by manipulating substrate sputter bias. Therefore, process optimization work is needed to identify the deposition parameters that will yield low-stress TiN.

7.2 VO₂ based switch

Based on the defect model developed for VO₂, and transport characteristics studied, there are several points that need follow up:

1. It was speculated that the difference in mobility activation energy for in the semiconducting phase was due to structural distortions. Physical characterisation of this distortion by synchrotron x-ray or neutron scattering experiments is needed to confirm the hypothesis.
2. In addition, the possibility of using VO₂ for optical switching should be investigated by fabricating optical switch devices. One possible design could involve a design similar to the MEMS switch without mechanical deflection. Optimum methods to actuate the phase transition should be investigated. Current-induced, Joule heating based actuation is one approach. Stress and electric field induced are other possibilities.

7.3 Barium Titanate based E-O modulators

The possibility of realizing a BT-based E-O modulator was demonstrated. However, the measured effective electro-optic values in the thin films were much lower than the bulk

values. The reason was speculated to be due to stress in the thin films. This hypothesis should be studied systematically, by use of buffer layers to tune the stress in the epitaxial films. Alternate methods to relieve stress in the BT layer such as thicker BT films and stress relieving buffer layers should be investigated.

For the BT-ST based E-O modulator, the super lattice structure should be optimized and the electro-optic effect characterized. Optimization of the superlattice structure could lead to significantly better electro-optic performance.

Appendix A – Material Properties of Titanium Nitride and Silicon

Table 8 List of Mechanical properties of TiN.

Property	Value	Source
Young's Modulus	106 – 640 GPa	[31, 41, 56]
Density	4500 – 5700 kg/m ³	[41, 56]
Hardness	12 – 24 GPa	[56]

Table 9 List of Mechanical properties of Silicon.

Property	Value	Source
Young's Modulus	160 GPa	[45]
Density	2697 kg/m ³	[45]
Failure Strength	7 GPa	[45]

Bibliography

1. B. Acklin, M. Schienle, B. Weiss, L. Stoll, and G. Muller, "Novel Optical Switches Based On Carrier Injection in 3 and 5 Wave-Guide Couplers - Tic and Sic," *Electronics Letters* 30 (3), 217-218 (1994).
2. V. A. Aksyuk, F. Pardo, D. Carr, D. Greywall, H. B. Chan, M. E. Simon, A. Gasparyan, H. Shea, V. Lifton, C. Bolle, S. Arney, R. Frahm, M. Paczkowski, M. Haueis, R. Ryf, D. T. Neilson, J. Kim, C. R. Giles, and D. Bishop, "Beam-steering micromirrors for large optical cross-connects," *Journal of Lightwave Technology* 21 (3), 634-642 (2003).
3. T. Barwicz, M. A. Popovic, P. T. Rakich, M. R. Watts, H. A. Haus, E. P. Ippen, and H. I. Smith, "Microring-resonator-based add-drop filters in SiN: fabrication and analysis," *Optics Express* 12 (7), 1437-1442 (2004).
4. J. F. Baumard and E. Tani, "Electrical-Conductivity and Charge Compensation in Nb Doped TiO₂ Rutile," *Journal of Chemical Physics* 67 (3), 857-860 (1977).
5. J. F. Baumard and E. Tani, "Thermoelectric-Power in Reduced Pure and Nb-Doped TiO₂ Rutile at High-Temperature," *Physica Status Solidi a-Applied Research* 39 (2), 373-382 (1977).
6. W. Bruckner, W. Moldenhauer, H. Wich, E. Wolf, H. Oppermann, U. Gerlach, and W. Reichelt, "The range of homogeneity of VO₂ and the Influence of the composition on the physical properties (II)," *Physica Status Solidi A* 29, 63-70 (1975).
7. W. Bruckner, H. Oppermann, W. Reichelt, J. I. Terukow, F. A. Tschudnowski, and E. Wolf, *Vanadiumoxide: Darstellung, Eigenschaften, Anwendung* (Akademie-Verlag, Berlin, 1983).
8. A. Cavalleri, C. Toth, C. W. Siders, J. A. Squier, F. Raksi, P. Forget, and J. C. Kieffer, "Femtosecond structural dynamics in VO₂ during an ultrafast solid-solid phase transition," *Physical Review Letters* 87 (23), 237401-1-237401-4 (2001).
9. A. Cavalleri, M. Rini, and R. W. Schoenlein, "Ultra-Broadband Femtosecond Measurements of the Photo-Induced Phase Transition in VO₂: From the Mid-IR to the Hard X-rays," *Journal of the Physical Society of Japan* 75 (1), 011004-1-011004-9 (2006).
10. E. E. Chain, "Optical-Properties of Vanadium Dioxide and Vanadium Pentoxide Thin-Films," *Applied Optics* 30 (19), 2782-2787 (1991).

11. R. T. Chen, H. Nguyen, and M. C. Wu, "A high-speed low-voltage stress-induced micromachined 2 x 2 optical switch," *IEEE Photonics Technology Letters* 11 (11), 1396-1398 (1999).
12. Coherent Inc., 5100 Patrick Henry Drive, Santa Clara CA 95054 USA.
13. J. R. Cooper, B. Alavi, L. W. Zhou, W. P. Beyermann, and G. Grüner, "Thermoelectric power of some high- T_c oxides," *Physical Review B* 35 (16), 8794-8796 (1987).
14. Coventorware, S. 4000 CentreGreen Way, Cary, NC 27513, USA.
15. M. D. Dollan and S. Mixture, "A high-temperature diffraction study of the reduction and reoxidation of nickel oxide," *The Rigaku Journal* 21 (2), 12-16 (2004).
16. M. P. Earnshaw, M. Cappuzzo, E. Chen, L. Gomez, A. Griffin, E. Laskowski, and A. Wong-Foy, "Highly-integrated planar lightwave circuit wavelength selective switch," *Electronics Letters* 39 (19), 1397-1398 (2003).
17. Elan Technology, PO Box 779, 169 Elan Court, Midway, GA 31320.
18. Engelhard Corporation, 101 Wood Avenue, Iselin, NJ 08830, USA.
19. Fimmwave: <http://www.photond.com/products/fimmwave>.
20. J. E. Ford, V. A. Aksyuk, D. J. Bishop, and J. A. Walker, "Wavelength add-drop switching using tilting micromirrors," *Journal of Lightwave Technology* 17 (5), 904-911 (1999).
21. H. P. R. Frederikse, "Recent studies on rutile (TiO_2)," *Journal of Applied Physics* 32 (10), 2211-2215 (1961).
22. F. Gervais and J. F. Baumard, "Infrared Properties of Stoichiometric and Nonstoichiometric Rutile TiO_2 ," *Journal of the Optical Society of America* 67 (2), 255-255 (1977).
23. D. M. Gill, B. A. Block, C. W. Conrad, B. W. Wessels, and S. T. Ho, "Thin film channel waveguides fabricated in metalorganic chemical vapor deposition grown $BaTiO_3$ on MgO ," *Applied Physics Letters* 69 (20), 2968-2970 (1996).
24. D. M. Gill, C. W. Conrad, G. Ford, B. W. Wessels, and S. T. Ho, "Thin-film channel waveguide electro-optic modulator in epitaxial $BaTiO_3$," *Applied Physics Letters* 71 (13), 1783-1785 (1997).
25. J. B. Goodenough, "The two components of the crystallographic transition in VO_2 ," *Journal of Solid State Chemistry* 3, 490-500 (1971).

26. C. H. Griffiths and H. K. Eastwood, "Influence of Stoichiometry On Metal-Semiconductor Transition in Vanadium Dioxide," *Journal of Applied Physics* 45 (5), 2201-2206 (1974).
27. J. Hiltunen, D. Seneviratne, R. Sun, M. Stolfi, H. L. Tuller, J. Lappalainen, and V. Lantto, "BaTiO₃-SrTiO₃ multilayer thin film electro-optic waveguide modulator," *Applied Physics Letters* 89 (24) (2006).
28. J. Hiltunen, D. Seneviratne, H. L. Tuller, J. Lappalainen, and V. Lantto, "Crystallographic and Dielectric Properties of Highly Oriented BaTiO₃ Films: Effect of Oxygen Pressure During Pulsed Laser Deposition," *To be submitted* (2007).
29. A. J. P. Hnatiw, R. G. DeCorby, J. N. McMullin, C. Callender, and R. I. MacDonald, "A multimode thermo-optic polymer switch for incorporation in a 4x4 hybrid integrated optoelectronic switch matrix," *Proceeding of the IEEE Canadian Conference on Electrical and Computer Engineering*, 645-650 (1999).
30. J. Kim, C. J. Nuzman, B. Kumar, D. F. Lieuwen, J. S. Kraus, A. Weiss, C. P. Lichtenwalner, A. R. Papazian, R. E. Frahm, N. R. Basavanhally, D. A. Ramsey, V. A. Aksyuk, F. Pardo, M. E. Simon, V. Lifton, H. B. Chan, M. Haueis, A. Gasparyan, H. R. Shea, S. Arney, C. A. Bolle, P. R. Kolodner, R. Ryf, D. T. Neilson, and J. V. Gates, "1100 x 1100 port MEMS-based optical crossconnect with 4-dB maximum loss," *IEEE Photonics Technology Letters* 15 (11), 1537-1539 (2003).
31. A. Karimi, O. R. Shojaei, T. Kruml, and J. L. Martin, "Characterisation of TiN thin films using the buldge test and the nanoindentation technique," *Thin Solid Films* 308-309, 334-339 (1997).
32. H. T. Kim, B. G. Chae, D. H. Youn, G. Kim, and K. Y. Kang, "Raman study of electric-field-induced first order metal-insulator transition in VO₂-based devices," *Applied Physics Letters* 86, 242101-1-242101-3 (2005).
33. L. C. Kimerling, "Photons to the rescue: Microelectronics becomes Microphotonics," in *The Electrochemical Society INTERFACE* (2000), Vol. 9, pp. 28-31.
34. N. Kimizuka, M. Saeki, and M. Nakahira, "Crystal growth of vanadium dioxide," *Materials Research Bulletin* 5, 403-408 (1970).
35. I. Kitahiro and A. Watanabe, "Thermoelectric power of vanadium dioxide whisker," *Journal of Physical Society of Japan* 21, 2423 (1966).
36. I. Kitahiro, T. Ohashi, and A. Watanabe, "Hall effect of vanadium dioxide powder," *Journal of Physical Society of Japan* 21, 2422 (1966).

37. P. Kofstad, *Nonstoichiometry, diffusion, and electrical conductivity in binary metal oxides* (Wiley-Science, New York, 1972).
38. A. Y. Kwan, C. H. Griffiths, and H. K. Eastwood, "Transport and structural properties of VO₂ films," *Applied Physics Letters* 20 (12), 93-95 (1971).
39. L. A. Ladd and W. Paul, "Optical and transport properties of high quality crystals of V₂O₄ near the metallic transition temperature," *Solid State Communications* 7, 425-428 (1969).
40. A. K. Lee, J. L. Jeon, M. H. Kim, W. Choi, and H. I. Yoo, "Oxygen nonstoichiometry (δ) of TiO₂- δ -revisited," *Journal of Solid State Chemistry* 178 (1), 185-193 (2005).
41. J. W. Lim, H. S. Park, T. H. Park, and J. J. Lee, "Mechanical properties of titanium nitride coatings," *Journal of Vacuum Science and Technology A* 18 (2), 524-528 (2000).
42. B. E. Little, H. A. Haus, J. S. Foresi, L. C. Kimerling, E. P. Ippen, and D. J. Ripin, "Wavelength switching and routing using absorption and resonance," *IEEE Photonics Technology Letters* 10 (6), 816-818 (1998).
43. B. E. Little, J. S. Foresi, G. Steinmeyer, E. R. Thoen, S. T. Chu, H. A. Haus, E. P. Ippen, L. C. Kimerling, and W. Greene, "Ultra-compact Si-SiO₂ microring resonator optical channel dropping filters," *IEEE Photonics Technology Letters* 10 (4), 549-551 (1998).
44. Y. L. Liu, E. K. Liu, S. L. Zhang, G. Z. Li, and J. S. Luo, "Silicon 1-X-2 Digital Optical Switch Using Plasma Dispersion," *Electronics Letters* 30 (2), 130-131 (1994).
45. N. Maluf, *An Introduction to Microelectromechanical Systems Engineering* (Artech House, Norwood, Massachusetts, 2000).
46. A. Mansingh, R. Singh, and M. Sayer, "Dielectric Behavior of Vanadium Dioxide," *Physica Status Solidi a-Applied Research* 49 (2), 773-779 (1978).
47. J. Mizusaki, Y. Yonemura, H. Kamata, K. Ohyama, N. Mori, H. Takai, H. Tagawa, M. Dokiya, K. Naraya, T. Sasamoto, H. Inaba, and T. Hashimoto, "Electronic conductivity, Seebeck coefficient, defect and electronic structure of nonstoichiometric La_{1-x}Sr_xMnO₃," *Solid State Ionics* 132 (3-4), 167-180 (2000).
48. E. Mohammed, A. Alduino, T. Thomas, H. Braunisch, D. Lu, J. Heck, A. Liu, I. Young, B. Barnett, G. Vandentop, and R. Mooney, "Optical interconnect systems integration for ultra-short-reach applications," *Intel Technical Journal* 8 (2), 115-127 (2004).
49. T. S. Moss, *Optical Properties of Semi-conductors* (Butterworths, London, 1961).

50. G. N. Nielson, "Micro-Opto-Mechanical Switching and Tuning for Integrated Optical Systems," PhD, Massachusetts Institute of Technology, 2004.
51. G. N. Nielson, D. Seneviratne, F. Lopez-Royo, P. T. Rakich, Y. Avrahami, M. R. Watts, H. A. Haus, H. L. Tuller, and G. Barbastathis, "Integrated wavelength-selective optical MEMS switching using ring resonator filters," *IEEE Photonics Technology Letters* 17 (6), 1190-1192 (2005).
52. E. Ollier, "Optical MEMS devices based on moving waveguides," *IEEE Journal of Selected Topics in Quantum Electronics* 8 (1), 155-162 (2002).
53. Omega Engineering Inc., One Omega Drive, PO Box 4047, Stamford, CT 06907, USA.
54. M. Paniccia, V. Krutul, and R. Koehl, "White Paper: Intel's Advances in Silicon Photonics," 2004. <http://www.intel.com/technology/silicon/sp/doc.htm>.
55. J. I. Pankove, *Optical Processes in Semiconductors* (Prentice-Hall, New Jersey, 1971).
56. P. Patsalas, C. Charitidis, and S. Logothetidis, "The effect of substrate temperature and biasing on the mechanical properties and structure of sputtered titanium nitride thin films," *Surface and Coatings Technology* 125 (1-3), 335-340 (2000).
57. C. Petit and J.-M. Frigerio, "Optical properties of VO₂ thin films in their dielectric and metallic states," *Proceedings of International Society of Optical Engineers SPIE* 3738, 102-106 (1999).
58. A. Petraru, J. Schubert, M. Schmid, and C. Buchal, "Ferroelectric BaTiO₃ thin-film optical waveguide modulators," *Applied Physics Letters* 81 (8), 1375-1377 (2002).
59. A. Petraru, J. Schubert, M. Schmid, O. Trithaveesak, and C. Buchal, "Integrated optical Mach-Zehnder modulator based on polycrystalline BaTiO₃," *Optics Letters* 28 (24), 2527-2529 (2003).
60. R. F. Pierret, *Semiconductor device fundamentals* (Addison-Wesley, Reading, 1996).
61. R. Ramaswami and K. Sivarajan, *Optical Networks: A Practical Perspective* (Morgan Kaufmann, San Francisco, 1998).
62. Rigaku MSC, 9009 New Trails Drive, The Woodlands, TX 77381, USA., .
63. M. Salib, L. Liao, R. Jones, M. Morse, A. Liu, D. Samara-Rubio, D. Alduino, and M. Paniccia, "Silicon Photonics," *Intel Technology Journal* 8 (2), 143-160 (2004).

64. D. Seneviratne, G. Nielson, G. Barbastathis, and H. Tuller, *Functional material for micro-mechanical systems*, US Patent & Trademark Office Application #20060006484 (2004).
65. S. D. Senturia, *Microsystem Design* (Kluwer Academic Publishers, Boston, 2001).
66. O. T. Sorensen, *Nonstoichiometric Oxides* (Academic Press, New York, 1981).
67. T. S. Stefanik, "Electrical Properties and Defect Structure of Praseodymium-Cerium Oxide Solid Solutions," PhD, Massachusetts Institute of Technology, 2004.
68. G. Stefanovich, A. Pergament, and D. Stefanovich, "Electrical switching and Mott transition in VO₂," *Journal of Physics-Condensed Matter* 12 (41), 8837-8845 (2000).
69. P. S. Tang, D. J. Towner, A. L. Meier, and B. W. Wessels, "Polarisation-insensitive Si₃N₄ strip-loaded BaTiO₃ thin-film waveguide with low propagation losses," *Electronics Letters* 39 (23), 1651-1652 (2003).
70. P. S. Tang, D. J. Towner, T. Hamano, A. L. Meier, and B. W. Wessels, "Electrooptic modulation up to 40 GHz in a barium titanate thin film waveguide modulator," *Optics Express* 12 (24), 5962-5967 (2004).
71. P. S. Tang, D. J. Towner, A. L. Meier, and B. W. Wessels, "Low-voltage, polarization-insensitive, electro-optic modulator based on a polydomain barium titanate thin film," *Applied Physics Letters* 85 (20), 4615-4617 (2004).
72. P. S. Tang, D. J. Towner, A. L. Meier, and B. W. Wessels, "Low-loss electrooptic BaTiO₃ thin film waveguide modulator," *IEEE Photonics Technology Letters* 16 (8), 1837-1839 (2004).
73. P. Tang, A. L. Meier, D. J. Towner, and B. W. Wessels, "High-speed travelling-wave BaTiO₃ thin-film electro-optic modulators," *Electronics Letters* 41 (23), 1296-1297 (2005).
74. P. S. Tang, A. L. Meier, D. J. Towner, and B. W. Wessels, "BaTiO₃ thin-film waveguide modulator with a low voltage-length product at near-infrared wavelengths of 0.98 and 1.55 μm," *Optics Letters* 30 (3), 254-256 (2005).
75. W. R. Thurber and A. J. H. Mante, *Physical Review* 139, A1655 (1965).
76. H. L. Tuller and A. S. Nowick, "Small Polaron Electron-Transport in Reduced CeO₂ Single-Crystals," *Journal of Physics and Chemistry of Solids* 38 (8), 859-867 (1977).

77. H. L. Tuller and A. S. Nowick, "Defect structure and Electrical Properties of Nonstoichiometric CeO₂ single crystals," *Journal of Electrochemical Society* 126 (2), 209-217 (1979).
78. Varian Inc., 121 Hartwell Avenue, Lexington, MA 02421, USA.
79. H. W. Verleur, A. S. Barker Jr., and C. N. Berglund, "Optical Properties of VO₂ between 0.25 and 5 eV," *Physical Review* 172 (3), 788-798 (1968).
80. R. W. Vest and J. M. Honig, "Highly Conducting Ceramics and the Conductor-Insulator Transition," in *Electrical Conductivity in Ceramics and Glasses (Part B)*, edited by Tallan N. M. (Marcel Dekker, New York, 1974), pp. 343-452.
81. M. R. Watts, "Wavelength Switching and Routing through Evanescently Induced Absorption," S.M., Massachusetts Institute of Technology, 2001.
82. H. A. Wriedt, "The O-V (Oxygen-Vanadium) System," *Bulletin of Alloy Phase Diagrams* 10 (3), 271-276 (1989).
83. A. Zylbersztein and N. F. Mott, "Metal-Insulator Transition in Vanadium Dioxide," *Physical Review B* 11 (11), 4383-4395 (1975).